

Ing. Stefan Moscher, BSc

Stability of PM6/Y6 based bulk heterojunction organic solar cells

-

Thermal influence on the optical, morphological and photovoltaic properties

MASTER'S THESIS

to achieve the university degree of

Master of Science

Master's degree programme:

Environmental System Sciences / Climate Change and Environmental Technology

submitted to

Graz University of Technology

Supervisors

Univ.-Prof. Dipl.-Ing. Dr.techn. Gregor Trimmel

Dipl.-Ing. Dr.techn. Thomas Rath

Institute for Chemistry and Technology of Materials

Graz, April 2023

AFFIDAVIT

I declare that I have authored this thesis independently, that I have not used other than the declared sources/resources, and that I have explicitly indicated all material which has been quoted either literally or by content from the sources used. The text document uploaded to TUGRAZonline is identical to the present master's thesis.

Date, Signature

Acknowledgement

I would like to express my warmest thanks to my supervisor Professor Gregor Trimmel for the opportunity to be part of this working group at the TU Graz. The chance to work on a totally current topic in a technically perfectly equipped laboratory makes me very happy. I would also like to thank the entire working group, which not only supported me greatly in my work, but also created a very friendly relationship beyond the work itself. These circumstances, which cannot be taken for granted, have made the time during my work even more enjoyable.

I have to say an extremely big thank you to Dr. Thomas Rath for the great professional support during my time at the TU Graz and especially the time he was available for advice and assistance.

In addition, I would like to thank my family and friends for the great support in my life so far, especially my parents and my charming partner Melanie Korbilius, PhD. and my lovely son Julian. This was and is not self-evident for me and I am infinitely grateful for it!

Table of Contents

1	Introduction	1
1.1	NFA solar cells – general aspects	2
1.2	PM6/Y6-based organic solar cells	4
1.3	Working principle of organic solar cells	8
1.3.1	Important parameters in solar cell characterization	11
1.4	Lifetime evaluation	13
2	Objectives	15
3	Results and discussion	16
3.1	Binary OSCs based on the absorber materials PM6 and Y6	16
3.2	Investigation of the annealing step	17
3.2.1	Influence of thermal annealing on the EQE spectra	20
3.2.2	Dependency of J_{SC} and V_{OC} on the light intensity	21
3.2.3	Exciton dissociation probability and charge collection efficiency	23
3.3	Temperature stability tests of the binary PM6/Y6 system	24
3.4	Ternary System based on the absorber materials PM6, Y6 and PC ₇₁ BM	27
3.5	Temperature stability tests of the ternary PM6/Y6/PC ₇₁ BM system	28
3.6	Comparison of the temperature stability tests	30
3.6.1	Optical properties – UV-Vis spectroscopy	31
3.6.2	EQE spectra	34
3.6.3	Hole and electron mobility	37
3.6.4	Light intensity dependent measurements of J_{SC} and V_{OC}	39
3.6.5	Exciton dissociation probability and charge collection efficiency	42
3.6.6	Atomic force microscopy	45
3.6.7	TEM investigations	47
3.6.8	GIWAXS and GISAXS investigations	49
3.7	Long-term stability	52
3.7.1	ISOS-D-1 shelf life	52

3.7.2	ISOS-D-2 high storage temperature	56
3.7.3	ISOS-LT-1 solar thermal cycling (cycle RT – 65°C)	60
4	Conclusions	64
5	Experimental part	69
5.1	Solar cell and sample preparation.....	69
5.2	Solar cell characterization – JV characteristics	69
5.3	Temperature stability tests.....	70
5.3.1	Investigation of the annealing step.....	70
5.3.2	Temperature treatment for 1020 minutes at 50 and 100°C	70
5.3.3	ISOS-D-1 shelf life.....	70
5.3.4	ISOS-D-2 high storage temperature	71
5.3.5	ISOS-LT-1 solar thermal cycling (cycle RT – 65°C)	71
5.4	Layer thickness measurements	71
5.5	UV/Vis spectroscopy.....	72
5.6	EQE spectra	72
5.7	Determination of hole and electron mobility.....	72
5.8	Light intensity dependent measurements of J_{sc} and V_{oc}	73
5.9	Exciton dissociation probability and charge collection efficiency	73
5.10	Atomic force microscopy	74
5.11	TEM investigations.....	74
5.12	GIWAXS and GISAXS measurements	74
5.13	Used materials, chemicals and solvents	74
6	References	76
7	Appendix	84

Abstract

The progress of power conversion efficiencies (PCEs) of organic photovoltaics has been great in the recent years. Since the beginning of the development and application of highly efficient non-fullerene acceptors in the middle of the last decade, the PCEs of organic solar cells improved from slightly above 10% to currently more than 19%. Together with other advantages such as roll-to-roll processability, different coloring, flexibility and semi-transparency, the high efficiency makes organic photovoltaics an interesting technology for commercialization and their usage in various applications in large scale. One of the main obstacles is the limited long-term stability of organic solar cells. Even though also their stability has been improved over the last years and promising T_{80} lifetimes of a few thousand hours have already been reported, extensive research in this field is still needed to obtain reliable stability over many years.

Thus, this work focused on the thermal stability of organic solar cells with absorber layers based on the conjugated polymer PM6 and the non-fullerene acceptor Y6. Both materials are among the most investigated ones in organic solar cell research and with this material combination, efficiencies of around 17.5% have been reported. In this work, solar cells with PCEs up to 17.0% were obtained and the influence of thermal treatment of the bulk heterojunction absorber layers on their optical, morphological and photovoltaic properties was investigated. We could demonstrate that a temperature treatment of 50°C for 1020 minutes has virtually no influence on the optical, morphological and photovoltaic properties, but in case of a treatment of 100°C for 1020 minutes some changes were observed. Here, the PCE was affected by the worse fill factor due to the increasing serial and decreasing parallel resistance. The ratio of the hole and electron mobilities was also strongly affected, changing by a factor of more than 10. In the UV-Vis and EQE spectra a slight red shift of the Y6 absorption was observed, which can be associated with a higher crystallinity in this phase. In addition, the charge collection efficiency was reduced by the temperature effect at 100°C for 1020 minutes. Moreover, it was investigated whether the addition of a small amount of PC₇₁BM can reduce the adverse effects of the exposure of the solar cells to 100°C and in some parameters such as the fill factor and the charge collection efficiency. Benefits could be observed, but overall no significant improvement was revealed. In addition, long term stability tests of solar cells at room temperature and 65°C as well as using temperature cycling between 25 and 65°C were performed. T_{80} values with the addition of PC₇₁BM of about 5000 hours were obtained in the shelf life time experiment and about 3600 hours without. The T_{80} values of the 65°C storage experiment remained below 200 hours while in the temperature cycle experiment they stayed below 100 cycles, with one cycle

time of about three hours. In all of the three long term stability tests, the devices with the addition of PC₇₁BM performed a little bit better.

Based on the performed experiments, the main cause of the PCE reduction is a further crystallization of Y6 in the absorber layer. While we could not observe that the domain sizes of the Y6 phase in the bulk heterojunction becomes significantly larger, atomic force microscopy and also grazing incidence small angle X-ray scattering indicated that the phase contrast between the donor and acceptor domains becomes higher. This leads to changes at the interface between donor and acceptor phase. We assume that the percolation pathways in the Y6 phase are negatively affected because of the significant reduction in the electron mobility in the absorber layers, observed after temperature treatment at 100°C for 1020 minutes, while the hole mobility remains very similar.

Kurzfassung

Die organische Photovoltaik hat in den letzten Jahren große Fortschritte bei den Wirkungsgraden (PCE) gemacht. Seit Beginn der Entwicklung und Anwendung hocheffizienter Nicht-Fulleren-Akzeptoren in der Mitte des letzten Jahrzehnts konnten die PCEs organischer Solarzellen von knapp über 10% auf derzeit über 19% verbessert werden. Zusammen mit anderen Vorteilen, wie der Verarbeitbarkeit im Rolle-zu-Rolle-Verfahren, der unterschiedlichen Farben, der Flexibilität und der Semitransparenz, macht der hohe PCE die organische Photovoltaik zu einer interessanten Technologie für die Kommerzialisierung und ihren Einsatz in verschiedenen Anwendungen in großem Maßstab. Eines der Haupthindernisse auf diesem Weg ist die begrenzte Langzeitstabilität der organischen Solarzellen. Obwohl auch ihre Stabilität in den letzten Jahren verbessert werden konnte und bereits über vielversprechende T_{80} -Lebensdauern von einigen tausend Stunden berichtet wird, ist noch umfangreiche Forschung in diese Richtung erforderlich, um eine zuverlässige Stabilität über viele Jahre zu erreichen.

Daher wurde in dieser Arbeit der Schwerpunkt auf die Untersuchung der thermischen Stabilität von organischen Solarzellen mit Absorberschichten auf Basis des konjugierten Polymers PM6 und des Nicht-Fulleren-Akzeptors Y6 gelegt. Beide Materialien gehören zu den am meisten in der organischen Solarzellenforschung untersuchten und zeigen in Kombination PCEs von etwa 17,5%. In dieser Studie wurden PCEs bis zu 17,0% erzielt und der Einfluss der thermischen Behandlung der Absorberschichten auf ihre optischen, morphologischen und auch photovoltaischen Eigenschaften untersucht. Dabei wurde festgestellt, dass eine Temperaturbehandlung von 50°C für 1020 Minuten praktisch keinen Einfluss auf die optischen, morphologischen und photovoltaischen Eigenschaften hat, aber im Falle einer Behandlung von 100°C für 1020 Minuten wurden einige Veränderungen beobachtet. Hierbei wurde der PCE durch den schlechteren Füllfaktor aufgrund des zunehmenden seriellen und abnehmenden parallelen Widerstands beeinflusst. Das Verhältnis von Loch- und Elektronenmobilität war ebenfalls stark betroffen und änderte sich um einen Faktor von mehr als 10. In den UV-Vis- und EQE-Spektren wurde eine leichte Rotverschiebung der Y6-Absorption beobachtet, die mit einer höheren Kristallinität in dieser Phase in Verbindung gebracht werden konnte. Darüber hinaus wurde die Ladungsträgersammeleffizienz durch die Temperatureinwirkung von 100°C für 1020 Minuten reduziert. Weiters wurde untersucht, ob die Zugabe einer kleinen Menge von PC₇₁BM die negativen Auswirkungen durch die Exposition der Solarzellen bei 100°C verringern kann. Bei einigen Parametern wie dem Füllfaktor und der

Ladungsträgersammeleffizienz wurden Vorteile festgestellt, aber in Summe konnten wenige signifikante Verbesserungen festgestellt werden. Zusätzlich wurden Langzeitstabilitätstests von Solarzellen bei Raumtemperatur und 65°C, sowie unter Verwendung eines Temperaturzyklus zwischen 25 und 65°C durchgeführt. Bei den Experimenten zur Stabilität wurden T_{80} -Werte von etwa 5000 Stunden mit dem Zusatz von PC₇₁BM und etwa 3600 Stunden ohne diesen Zusatz erreicht. Die T_{80} -Werte des 65°C Lagerungsexperiments blieben unter 200 Stunden und im Temperaturzyklusexperiment blieben sie unter 100 Zyklen, mit einer Zykluszeit von etwa drei Stunden. In allen drei Langzeitstabilitätstests schnitten die Zellen mit dem Zusatz von PC₇₁BM etwas besser ab.

Die Hauptursache für die Verringerung des PCEs ist eine weitere Kristallisation von Y6 in der Absorberschicht und es wurden keine Anzeichen dafür beobachtet, dass die Domänengrößen der Y6-Phase in der Bulk-Heterojunction Absorberschicht signifikant größer werden. Allerdings wurde der Phasenkontrast zwischen den Donor- und Akzeptordomänen größer, was mittels Rasterkraftmikroskopie und Röntgenkleinwinkelstreuung unter streifendem Einfall festgestellt wurde. Die Erhöhung des Phasenkontrasts führt zu Veränderungen an der Grenzfläche zwischen der Donor- und Akzeptorphase und wir gehen davon aus, dass die Perkulationswege in der Y6-Phase negativ beeinflusst werden, da nach einer Temperaturbehandlung bei 100°C für 1020 Minuten eine deutliche Verringerung der Elektronenmobilität in den Absorberschichten beobachtet wurde, während die Lochmobilität sehr ähnlich blieb.

1 Introduction

Due to the constantly increasing energy demand, global warming and the scarcity of fossil resources, it is necessary to develop fossil fuel-free strategies for energy supply. Among other renewable energy sources, solar cells are a very good alternative to reduce dependence on fossil fuels, as the sun offers enormous potential as an energy source. Another big advantage is that solar cells do not cause any carbon dioxide emissions during operation.

One of the most promising emerging solar cell technologies is organic photovoltaics (OPV). Exploring novel organic optoelectronic materials is one of the most important steps to advance the development of OPVs. Furthermore, over the past two decades, the power conversion efficiency (PCE) of organic solar cells (OSCs) has increased from 5% to over 19%^{1–14} by using various near-infrared absorbing materials as active layers, whereas tandem OSCs have already reached a PCE of more than 20%.¹⁵

The major benefits of OSCs are their potentially low manufacturing costs when using low-temperature deposition methods and high-throughput processing via roll-to-roll printing and coating methods, as shown schematically in Figure 1. In this roll-to-roll process, a roll of a flexible transparent plastic foil coated with a semi-transparent electrode is used as substrate. The required coatings are then applied sequentially by e.g. slot die coating, blade coating, screen printing or spraying and finally an encapsulation foil is laminated to protect the modules from air and environmental influences in order to ensure their long-term stability.

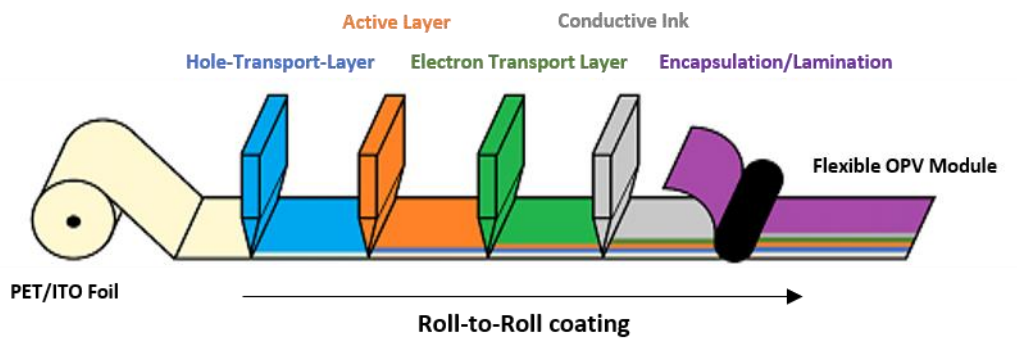


Figure 1: Scheme of a roll-to-roll coating line for flexible solar cell modules.

Further advantages of OSCs are their short energy payback times due to the elimination of energy-consuming high temperature processes in their fabrication, as well as the high adaptability of organic absorber materials due to the use of organic chemistry. In addition, OSCs offer a high energy output, strong low-light performance, they are flexible and lightweight and can be also prepared in different colors and different degrees of semitransparency. Moreover,

because of the high absorption coefficients of the organic absorber materials, only very low amounts of material are required.

Due to the possibility to customize colors and semi-transparency, new products incorporating photovoltaics become feasible and are already emerging, for example in architecture (incorporation into glass facades, windows, agricultural greenhouses). Because of its low mass and stretchability, OSCs can be used for example in consumer electronics and wearables. Their integration into portable and self-powered devices, where they can be used for the recycling of indoor light energy, is also very interesting. Despite achieving remarkable PCEs, the long-term stability of OSCs represents an obstacle for their use in a variety of applications. Therefore, research towards understanding the main causes of the degradation of solar cells to elaborate approaches to improve their long-term stability is currently highly needed.

1.1 NFA solar cells – general aspects

To date, a vast number of new non-fullerene acceptor (NFA) structures have been developed and used in OSCs along with a wide range of donor materials. The progress of OPVs in the last years is thoroughly described in several recent reviews.¹⁶

In brief, until the mid of the last decade, the organic solar cell research was focused on fullerene-based solar cells. For example, based on PTB7-Th:PC₇₁BM, a PCE of 10.1% was achieved in 2015.¹⁷ The maximum efficiencies reported today for polymer/fullerene solar cells are little above 11%.^{18–21}

Regardless of this success of fullerene-based OSCs, the intrinsically limited ability of fullerenes for light harvesting and other issues have limited further progress regarding PCE. On the contrary, the design and synthesis of new organic non-fullerene acceptor materials has brought new possibilities for further improvements to the field of OSCs. Numerous novel acceptor materials (mainly small molecules, but also polymeric materials) have been designed and synthesized with the right bandgaps to effectively capture solar radiation and the right energy levels to minimize energy loss of OSCs.²² Particularly, a variety of molecular design techniques, including side chain and functional group engineering and backbone modification, have been established to effectively control the optoelectronic characteristics of active layers.

Wide-bandgap polymer donors such as the J-series, PBDB-series, PTQ10 and D18 were designed and developed to provide complementing absorption with narrow-bandgap NFAs. The most often used polymers among them were PBDB-T, PBDB-T-2F (PM6) and D18 because of

their excellent processing capabilities, acceptable energy levels and improved phase separation. These polymers were combined with NFAs to obtain PCEs up to over 18%.^{1–13,15,23–25}

The benefits of NFAs' tunable energy levels, near-infrared area absorption and strong thermal and photo stability are widely established. Perylene diimide units (PDI), which have a broad and planar structure, good photochemical stability and are easy to synthesize and modify, are used as n-type materials in many applications. In 2013, PDI dimers of bis-PDIT-EG directly linked through thiophene were created.²⁶ This technique can reduce excessive molecular aggregation and improve charge transfer in the active layers. For example, spirofluorene served as the π -bridge in the SF(PDI)₂ small molecule acceptor (SMA), published by Yan *et al.* in 2016. With a low voltage drop to 0.61 V, OSCs based on P3TEA:SF(PDI)₂ demonstrated a high PCE of 9.5% and an internal quantum efficiency of around 90%.²⁷

Non-covalent intramolecular interactions are used to regulate the planarity of molecular structures in unfused-ring SMAs, which are defined as those that have a partially or completely unfused backbone structure. Such compounds may often be generated using straightforward synthetic techniques. In only three steps, Chen *et al.* produced an unfused-ring SMA (DICTF) in 2016.²⁸ COTI-4F and SiOTI-4F, two unfused-ring SMAs with ultra-narrow bandgaps and absorption ranges above 1000 nm (Eg of 1.1 eV), were reported by Lee *et al.*²⁹ with incorporated alkoxythiophene as the π -bridge. A PCE of 9% was obtained by the PTB7-Th:SiOTI-4F-based devices.²⁹ In 2018, a PCE of 11.5% for HF-PCIC-based solar cells was reported, in which the unfused core in acceptor-donor-core-donor-acceptor (A-D-C-D-A) small molecules served as a useful building block to create high-performance non-fullerene acceptors.³⁰

Fused-ring electron acceptors (FREAs) have demonstrated significant promise for the development of OSCs. FREAs possess a fused-ring core that donates electrons, two terminal groups that pull electrons away from the core and a planar π -conjugated bridge that connects them. This results in a planar molecular structure with strong intermolecular interactions. Additionally, the development of OSCs currently makes FREAs the key acceptors.²⁵

The first description of an A-D-A-D-A-type narrow-bandgap acceptor with a benzotriazole core was made in 2017³¹, representing a significant development for high-performance Y-series acceptors. In 2019, Yuan *et al.* presented a new acceptor, Y6, using the benzothiadiazole unit for an electron-deficient core-based fused-ring acceptor yielding a PCE of over 15.7% by a single-junction OSC.³²

Regarding the stability of OPV, it is now known that fullerene dimerization and morphological instability, caused by the fullerene component diffusing into and through the semiconducting polymeric donor, are important degradation processes in the classic fullerene systems. Several recent studies deal with the current challenges of NFA-based OSCs, including stability issues and advances regarding their lifetime.^{33–38} Based on that, NFAs do not appear to be subject to the same degrading processes, at least not to the same degree. Nevertheless, they can get damaged by chemical reactions with interface materials, in particular in combination with UV-radiation.

However, there are still many unanswered concerns and the investigations of the solar cell stability is barely keeping up with the introduction of new materials that need to be evaluated in this respect. To gather reliable and reproducible data about the stability of a novel system, stability tests require feedback periods of many weeks or even months. Given this tedious timeframe, only a small number of systems may be studied at any given time due to experimental capacity constraints and limited advancement for a single material. Novel techniques that allow stability prediction from shorter measurements, accelerated testing and ideas that do not rely on whole devices, but instead evaluate the potential of individual components before combining them into OSCs, will become more relevant in the future.³⁹

1.2 PM6/Y6-based organic solar cells

Because of their excellent potential to achieve highPCEs, OPVs using non-fullerene acceptors have gained a lot of interest in the past 10 years. The main difficulties of simultaneously enabling effective charge separation/transport and a low voltage loss limit the development of higher performance OPVs. Regarding the NFAs, materials from the Y-family are currently leading to the highest PCEs. The structure of Y6 (Figure 2), the most famous NFA of the Y-family, is based on a central ladder-type multi-fused ring with the electron-deficient core 2,1,3-benzothiadiazole (BT). Additionally, the electron affinity may be adjusted by adding an electron-withdrawing moiety to the central core to form a charge-deficient area. BT as one of the most often used electron-poor units in this regard has been widely applied in creating low-bandgap conjugated materials and polymers due to its economic availability and the electron-withdrawing property of its sp^2 -hybridized nitrogen atoms. Additionally, due to their high mobility, BT-based polymers may be able to provide thick-active-layer OPVs that are extremely effective, which is important regarding large area fabrication and their commercialization.^{31,32,40–43}

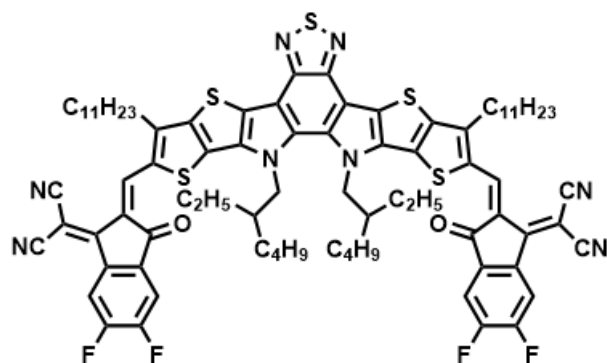


Figure 2: Structure of the acceptor Y6.

In 2015, Zhang *et al.* introduced the copolymer PM6 with 4,8-bis(5-(2-ethylhexyl)-4-fluorothiophen-2-yl) benzo[1,2- *b* :4,5- *b'*]-dithiophene (BDT-F) as the donor and 1,3-bis(thiophen-2-yl)-5,7-bis(2-ethylhexyl)benzo-[1,2-*c* :4,5-*c'*] dithiophene-4,8-dione (BDD) as the acceptor for use in solar applications (structure of PM6 is shown in Figure 3).⁴⁴ This polymer displayed a deep HOMO energy level and a wide bandgap of 1.80 eV. With a film thickness of 75 nm, the PM6-based inverted SCs with PC₇₁BM as acceptor had a PCE of 9.2% and a V_{OC} of 0.98 V. Furthermore, semitransparent devices built on the PM6/PC₇₁BM basis had a PCE of 5.7%, which were among the highest values recorded for a semitransparent single-junction solar cell at that time.⁴⁴

Thin films of PM6 demonstrate a strong crystallinity and a dominating face on packing with regard to the electrodes, which is favorable for charge transport perpendicular to the substrate, as it is needed in the solar cell. In the UV-Vis absorption spectra of PM6 in solution, two distinct absorption bands are visible in the 300-700 nm region, which is characteristic for D-A copolymers. In solution, the absorption maximum is based at a wavelength of ~550 nm, but is redshifted to 570 nm in the solid film, accompanied by a prominent shoulder peak at 614 nm.

This can be related to the good polymer chain aggregation in the solid state.⁴⁴ These findings suggest that PM6 is an effective material for photovoltaic use.

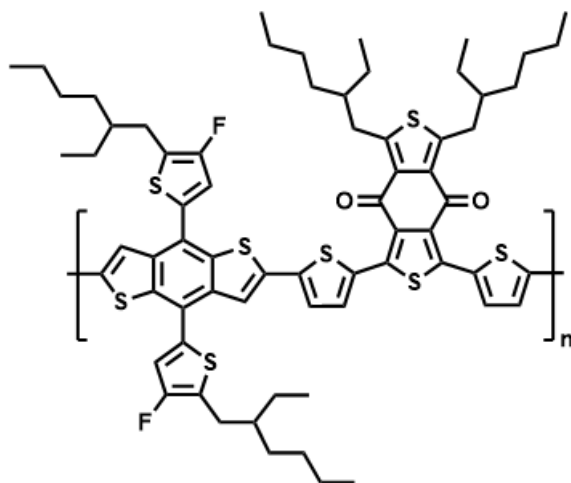


Figure 3: Structure of the donor PM6.

The reported PCE of OSCs has reached more than 19%⁷ up to this point, but the limited stability issue prevents its commercialization, raising scientists' curiosity for further exploration. The current commercial solar cell technologies, monocrystalline and multi-crystalline silicon, cadmium telluride and copper indium gallium selenide/sulfide solar cells, have high efficiencies and operating longevity of more than 20 years. Currently, they share the entire commercial photovoltaic market. However, because of their disadvantages such as relatively high manufacturing costs, difficult processing conditions, brittle construction and poor aesthetics^{45,46}, new types of solar cells are needed that possess high efficiency, low costs, ease of production and flexibility. The stability of OSCs is still not thoroughly investigated, which makes further studies of stability aspects in highly efficient OSCs necessary to increase the chances of a broad and successful commercialization of OSCs in the future.

Regarding the stability of PM6:Y6-based OSCs, it was found that e.g. light-induced traps can reduce the charge carrier mobility and the current extraction potential, while increasing non-radiative recombination. Based on the comparison of the donor-, acceptor- and blend-exposed devices, it is concluded that the photodegradation of PM6 predominates in the photodegradation process of PM6:Y6-based devices.⁴⁷ Han *et al.* presented a T₈₀ lifespan of over 4,000 h under continuous illumination in a glovebox with nitrogen atmosphere (JV curves measured in certain intervals), demonstrating the quite good long-term stability of this heterojunction solar cell. Furthermore, PM6:Y6 cells displayed a PCE of 16.46% and a greatly improved long-term stability under continuous illumination circumstances.⁴⁸

Upon addition of ITIC-M as second acceptor to the PM6/Y6 system, a very high PCE of 18.13% as well as a high fill factor of 80.1% could be achieved in ternary organic PM6:Y6-based solar cells.⁴⁹ PM6/Y6/PC₇₁BM-based devices reported by Li *et al.*, with a PCE of 16.72%, compared to 15.56% for the binary system, have a significantly better light and thermal stability. Additionally, PC₇₁BM, a fullerene derivative, offers a number of benefits including excellent isotropic transport ability and good solubility.⁵⁰

Thus, various approaches can be used to further improve the principally already well performing binary PM6/Y6 system, including e.g. stabilizing additives, intermediate layers, or the usage of ternary and quaternary systems with additional acceptors.

1.3 Working principle of organic solar cells

The structure of the OSCs in conventional device architecture is shown schematically in Figure 4A. A semi-transparent electrode (ITO) on glass is covered with a hole transport layer (HTL) layer. On top of this is the bulk heterojunction active layer, followed by an electron transport layer (ETL) layer and the opaque metal electrode. Charge extraction is facilitated by the use of selective ETL and HTL between the electrodes and the active layer.^{51,52}

The exciton generation process is illustrated in Figure 4B. When a photon with sufficient energy is absorbed, an electron can be excited from the HOMO level to the LUMO level, while the hole remains at the HOMO level. The respective energy levels of the materials used to fabricate typical PM6/Y6 solar cells in conventional architecture are depicted in Figure 4C. The work functions of ITO, the Ag electrode, PEDOT:PSS, the HOMO and LUMO levels of PM6, Y6 and the ETL PNDIT-F3N-Br were obtained from the literature.^{53,54}

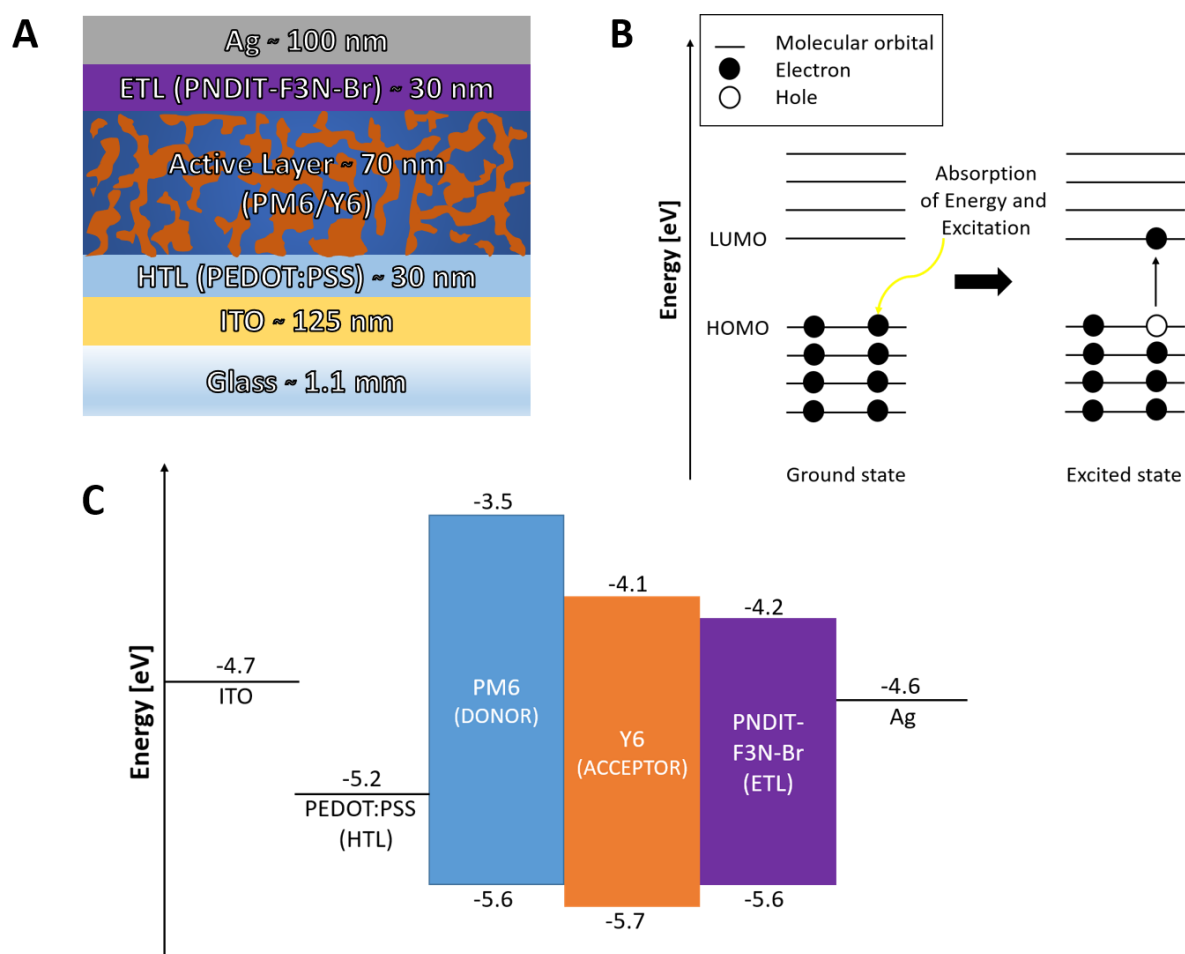


Figure 4: (A) Device architecture, (B) process of exciton generation and (C) energy levels of the different layers of the OSCs used in this work.

Currently, the most common active layer consists of a bulk heterojunction blend comprising one donor and one acceptor. However, it is also feasible to have an active layer with just one component. In this case, the donor and acceptor moieties are part of an identical molecule (monomer), oligomer, or polymer. These single-component solar cells may reach a PCE of up to 11% at the moment.^{55–57} The addition of a third component to the active layer is used to create ternary solar cells⁵⁸, which enables a more effective use of solar light and can also improve device performance and stability by reducing trap states. Morphological control becomes increasingly difficult when more than two materials are used for the bulk heterojunction layer.⁵⁹ The use of two- (tandem) or multi-junction cells is another approach to increase the wavelength range for solar light absorption.^{60–63}

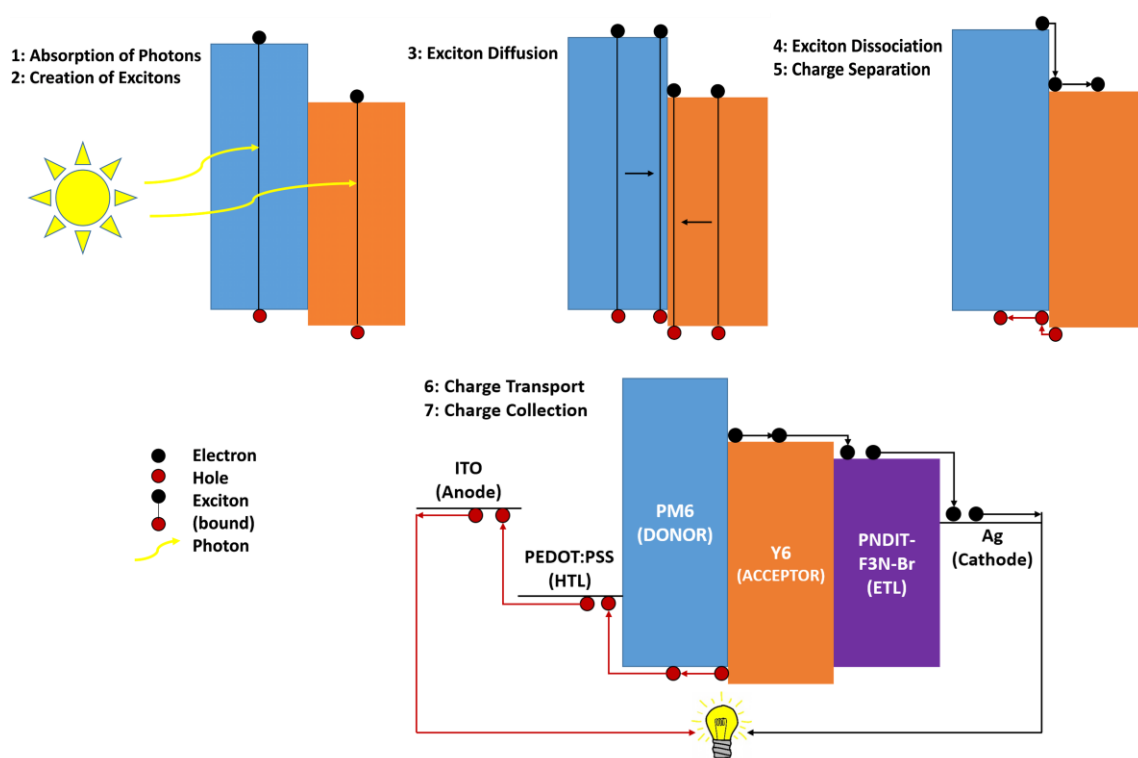


Figure 5: Scheme illustrating the solar energy conversion in an OSC used in this work.

Figure 5 schematically outlines the stepwise power generation of OSCs investigated in this work: The donor and NFA materials independently absorb photons efficiently (1), leading to the formation of a bound electron-hole pair, the exciton (2). The resulting electron of the bound electron-hole pair is excited from the HOMO level to the respective LUMO level, but still remains bound. In the next step, the exciton diffuses through the respective material to the boundary region, the donor-acceptor interface (3), and dissociates into free charge carriers, *i.e.* the electron-hole pair is no longer bound (4). An electron excited in the donor layer is transferred from the LUMO level of the donor to the LUMO level of the acceptor. Similar to

this process, a hole created in the acceptor moves from the HOMO level of the acceptor back to the HOMO level of the donor (5). Subsequently, the electrons move in the acceptor phase towards the cathode and the holes in the donor phase towards the anode (6), thus closing the circuit (7).

Each of these processes, from light absorption and exciton production through charge collection at the electrodes, have to be efficient to obtain high PCE values.⁶⁴ Singlet excitons are the main species created in an OSC as a result of light absorption. The photoluminescence quantum yield (PLQY), which measures a crucial feature of the substance, reflects the probability of an exciton undergoing radiative decay. Unless the molecule contains a heavy element, the intersystem crossing rate for singlet excitons is usually very low, but can increase for triplet excitons due to spin-orbit coupling in molecules with heavy atoms.⁶⁵

Although quick, the intersystem crossover in fullerenes has been observed to occur on a nanosecond timescale, which is slower than the exciton lifetime in most donor-acceptor bulk heterojunctions. Consequently, it is commonly believed that a singlet exciton is the main species produced in an OSC upon light absorption.⁶⁶

The ability of excitons in organic semiconductor materials to migrate between chromophores through a process known as exciton diffusion is a crucial characteristic that is of great importance for the functioning of the solar cell. Both intermolecular and intramolecular transfers are possible for molecules with multiple chromophores, such as conjugated polymers. Förster and Dexter energy transfer are combined to cause diffusion for singlet excitons. The incoherent, non-radiative transmission of excitons via dipole-dipole coupling between two chromophores is known as Förster resonant energy transfer (FRET). The PLQY of the donor chromophore, the extinction coefficient of the acceptor chromophore and the relative position of both chromophores all have a significant role in the rate of energy transfer. Excitons can travel across chromophores that are a few nanometers apart, which can be very effective.⁶⁷ Dexter energy transfer, on the other hand, only allows the transmission of excitons between chromophores with overlapping wave functions, since it is a short-range process mediated by the exchange of a single electron. Extensive studies have been performed to determine the exciton diffusion coefficients or diffusion lengths, showing that for many organic materials, the exciton diffusion length generally ranges from 5 to 10 nm.^{68,69}

1.3.1 Important parameters in solar cell characterization

The recording of a current-voltage characteristic in both the dark and illuminated states enables the determination of the most important electrical properties of a solar cell. As depicted in Figure 6, a voltage is given in a certain range and the current is measured to get the JV curve of the measured devices, with the dark curve reflecting typical diode characteristics.

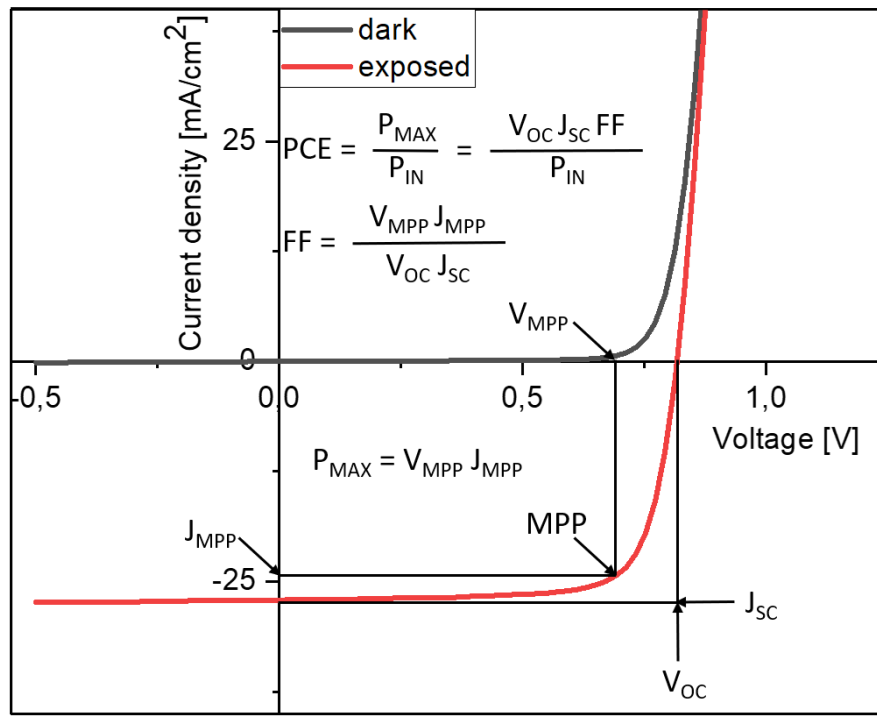


Figure 6: Current density / voltage characteristics.

Short-circuit current density (J_{sc}) reflects the efficiency of charge separation and charge transport per area. It is a function of the light intensity and depends on the thickness and morphology of the layer. However, the layer thickness cannot easily be increased as this would concomitantly increase the serial resistance, resulting in the opposite effect.³³

Open-circuit voltage (V_{oc}) reflects the maximum voltage of a solar cell measured without current and mainly depends on the energy difference between the LUMO of the acceptor and the HOMO of the donor. Furthermore, also the choice of the electrodes and their contact with the active layer, as well as the temperature and light intensity influence the open-circuit voltage.³³

J_{MPP} and V_{MPP} are those current and voltage parameters that are given at the point of maximum power (**MPP**), where the product of current and voltage is maximum.³³

Fill factor (FF) describes the relationship between the maximum power of the solar cell and the product of the short-circuit current and open-circuit voltage. As a consequence, the JV curve's squareness is evaluated by the FF, which can be seen as a quality indicator.³³

The **power conversion efficiency (PCE)** of solar cells is the ratio of the generated power to the radiant power.³³

The **charge carrier mobility μ** is also one important material feature that has a considerable impact on the efficiency of organic BHJ solar cells. The hopping rates between acceptor (donor) molecules determine the electron (hole) mobility, which is strongly influenced by the shape of the intermixed layer. All these impacts are taken into account in the effective medium method of the one-dimensional simulation with μ , which must be considered as an effective parameter.³³

1.4 Lifetime evaluation

In contrast to solar cells of the first and second generation (e.g. crystalline silicon or inorganic thin film solar cells), many emerging solar cell technologies including OSCs still display distinct decreases in their PCEs over time under certain conditions. For the solar cell technologies of the first and second generation, various evaluation methods have already been created and are well covered in standards.^{70,71} Methods for measuring OPV devices have been also already described, with a focus on developing standardized methods for precise and comparable lifespan estimation. These descriptions represent the agreement on OPV stability established at the first three ISOS international meetings (ISOS 2008–2010) and are reported by Reese *et al.* in 2011.⁷² Shelf life, outdoor, indoor and thermal cycling are the four main test categories that were created. Each category was then divided into three levels: basic, intermediate and advanced.⁷²

Table 1: Overview of some different long-term stability ISOS regulations⁷².

	ISOS-D-1 (shelf life)	ISOS-D-2 (high T storage)	ISOS-T-1 (thermal cycling)	ISOS-L-1 (laboratory simulations)
Test setup				
Environment	Dark	Dark	Dark	Constant light source
Load	Open circuit	Open circuit	Open circuit	MPP tracking preferred
Storage temperature	Ambient	65 ± 2°C	Cycle between RT and 65°C	Monitored, uncontrolled
Testing protocol				
Storage Temperature	Monitor ambient values	Control and monitor specimen temperature	Monitor specimen temperature	Monitor specimen temperature
Min. measurement intervals	Daily to weekly (adjust to device performance)	Daily to weekly (adjust to device performance)	Every 1-10 cycles for first 50 cycles, then once every 50 cycles	Daily to weekly (adjust to device performance)
Characterization temperature	Monitor	Monitor	Monitor specimen temperature on backside	Monitor specimen temperature on backside
Characterization irradiance	Monitor	Control (800–1100 W/m ²)	Control (800–1100 W/m ²)	Monitor (400–1200 W/m ²)
Output				
Time and Date	Report	Report	Report	Report
Characterization light source	Report type and irradiance level	Report type and irradiance level	Report type and irradiance level	Report light spectrum and irradiance level
Storage Temperature	Report	Report	Report specimen temperature	Report specimen temperature
Instantaneous performance parameters	Report Jsc, Voc, FF, PCE and MPP	Report Jsc, Voc, FF, PCE and MPP	Report Jsc, Voc, FF, PCE, MPP and full JVs optional	Report Jsc, Voc, FF, PCE, MPP and full JVs optional

An overview of various long-term stability tests is shown in Table 1. In the basic lifetime evaluation approach, samples are stored in the dark with no load to conduct shelf life experiments. This approach can include storing a sample at room temperature (ISOS-D-1), adjusting the temperature up to 65°C using a hotplate or an oven (ISOS-D-2) and carefully controlling the temperature and humidity in an environmental chamber ISOS-D-3, to perform so called damp heat tests.⁷²

In these tests, the photovoltaic performance of the devices is evaluated by periodically recording their JV curves, either outdoors in direct sunlight or indoors using a solar simulator. Although *in situ* monitoring outdoors is the most practical and scalable option which is closed to real-life conditions, it can also present a number of challenges, such as impacts from temperature coefficients, cloud cover, non-linearity in performance and irradiance, wind and seasonal variations in the energy dose received by a specimen.⁷²

To demonstrate that thermal cycling will not be a deterioration mechanism throughout the product's life, final product certification often requires thermal cycling with a temperature range considerably outside the limits of regular use. However, because this test involves sophisticated equipment and can only provide sparse data throughout development, particularly when samples are vulnerable to heat cycling damage, it could be laborious. As a result, there are many test categories that are dependent on both the quality of the available equipment and the resilience of the cell itself to thermal cycling-related damage. The basic type (ISOS-T-1) is an introductory test in which a specimen is brought from room temperature to 65°C using a hot plate.⁷²

Given that the spectral distribution is recorded, there are no restrictions on the type of light source used for the ISOS-L-1 test, but there are limitations on the type of light source used for the ISOS-L-2 & L-3 tests: The light sources shall match the sun spectrum as good as possible, such as calibrated metal halide lamps with daylight filters or xenon arc lamps with filters. It is also possible to use class A lamps for spectral mismatches in the 400-1100 nm range, which include a large amount of UV light down to 300 nm. Since the spectra of the lamps might vary with age, tracking the intensity of these light sources over time is essential for these experiments.⁷²

2 Objectives

As discussed above, the long-term stability is currently one of the major hurdles of OSCs towards further adaption in many applications. Therefore, this work is devoted to the investigation of the stability of OSCs. In particular, the focus was set on their thermal stability under operation as in real-life conditions, where OSCs will be often exposed to elevated temperatures. For the experiments, the absorber material combination of the conjugated polymer PM6 and the non-fullerene acceptor Y6 was chosen, as PM6 and acceptors of the Y-family are currently among the most efficient absorber layer systems in OPV.

The first objective of this work was to fabricate state-of-the art PM6/Y6 OSCs and to elaborate the effects of different thermal treatments on the solar cell performance. For that, three main types of experiments were conducted: (i) the influence of short-term (several minutes) heat exposure to temperatures up to 200°C was investigated, (ii) the effect of exposure to 50°C and 100°C for 1020 minutes was studied and (iii) the stability of the solar cells was tested over several hundreds of hours at 65°C, thermal cycling between 25 and 65°C and the data were compared to solar cells stored at room temperature. All these experiments have been conducted in inert atmosphere to exclude effects stemming from the encapsulation, oxygen or moisture.

The second objective was to correlate the changes in the solar cell parameters to possible changes of the optical, morphological and also electronic properties of the bulk heterojunction absorber layers. To obtain this goal, several characterizations of the absorber layers including UV-Vis spectroscopy, atomic force microscopy, transmission electron microscopy and X-ray scattering techniques, were performed. Besides the characterization of the solar cells by JV curves, recording of external quantum efficiency (EQE) spectra, studying recombination properties, exciton dissociation probabilities and charge collection efficiencies as well as the investigation of electron and hole mobilities were planned.

3 Results and discussion

In order to obtain well comparable and reproducible results from the investigations of the thermal stability of the solar cells, the corresponding experiments and lifetime tests were carried out only with solar cells over a certain efficiency threshold, which was set to efficiencies of more than 15%.

3.1 Binary OSCs based on the absorber materials PM6 and Y6

Therefore, in a first step, the processing parameters and thicknesses of the individual layers in the PM6/Y6 binary solar cells were optimized. As device architecture, the commonly used conventional structure was chosen, which is schematically shown in Figure 4A. In this device setup, a HTL (PEDOT:PSS) is coated on a glass-based, semi-transparent indium tin oxide (ITO) electrode. The bulk heterojunction active layer consists of a blend of the conjugated polymer PM6 and the NFA Y6 and is spin coated from a solution containing PM6 and Y6 in a weight ratio of 1 to 1.2 in the solvent chloroform with 0.5% (vol%) 1-chloronaphthalene as additive. Further, an ETL (PNDIT-F3N-Br), and the opaque silver electrodes are deposited on top of the absorber layer. More detailed information regarding the solar cell preparation is given in the Experimental part (Chapter 5).

The JV characteristics of the solar cell with the highest PCE prepared with the binary PM6/Y6 system within this study are presented in Figure 7. With this device, a PCE of 17.0% was achieved, with an open circuit voltage of 817 mV, a short circuit current density of 27.2 mA/cm² and a fill factor of 76%. The solar cells were illuminated with a Dedolight DLH400D lamp (metal-halide gas discharge lamp) with an intensity of 100 mW/cm² and a 0.070 mm² shadow mask was used to accurately define the active area. The current-voltage characteristics, measured with a Keithley 2400 source meter and a LabVIEW program, were recorded from 1.5 to -0.5 V with 20 mV steps.

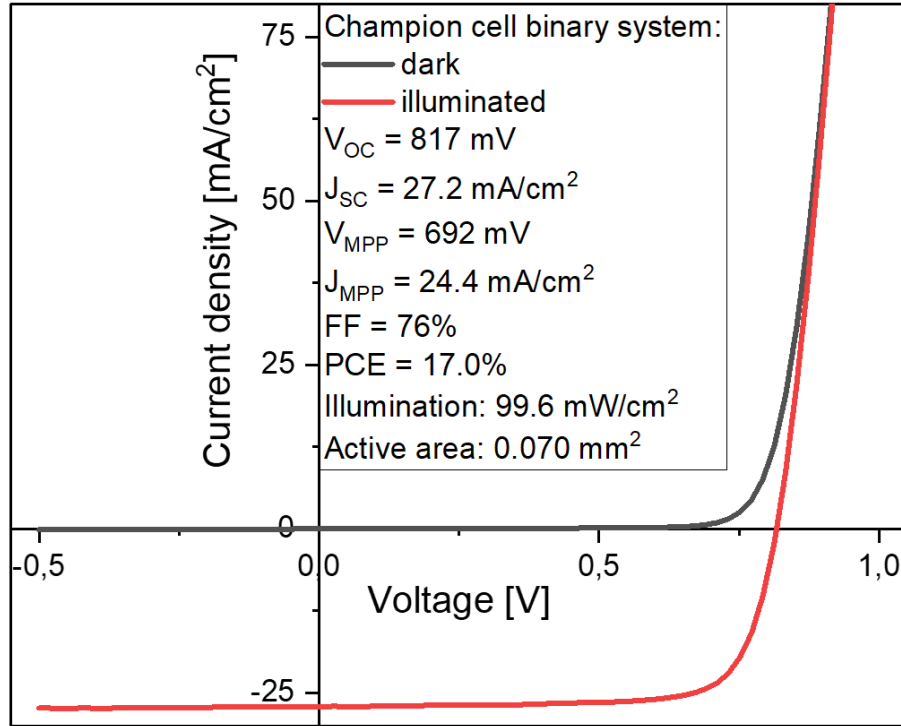


Figure 7: JV characteristics of the champion solar cell using the binary PM6/Y6 system, recorded in the dark and under illumination.

3.2 Investigation of the annealing step

In the standard procedure for the solar cell fabrication in this work, the active layer was annealed for 10 minutes at 100°C, as it is typically done in most of the reports in the literature.^{4,47,48} To investigate the actual influence of the annealing step of the active layer in more detail, an annealing experiment was performed. Herein, a set of similarly prepared absorber layers were subjected to an annealing procedure, in which the samples were heated with a rate of 10°C/min, from room temperature to 200°C, and then maintained at 200°C for 20 minutes. The temperatures have not been determined separately, but are the surface temperatures of the heating plate (CAT MCS66), which are displayed by this with an accuracy of $\pm 0.2^\circ\text{C}$. For this purpose, 20 devices, each with six solar cells, were placed on a hot plate and after every 10°C temperature increase, a substrate was removed from the hot plate during the heating run. After reaching 200°C, the last two sets of solar cells were taken from the heating plate after 10 and 20 minutes. For the evaluation of this experiment, the three best solar cells of each substrate were used. The reference devices with standard annealing step (100°C for 10 minutes) of the active layer revealed a PCE of 15.9%, which is well comparable to the solar cells, which perceived in this “heating run” experiment (c.f. Table 2).

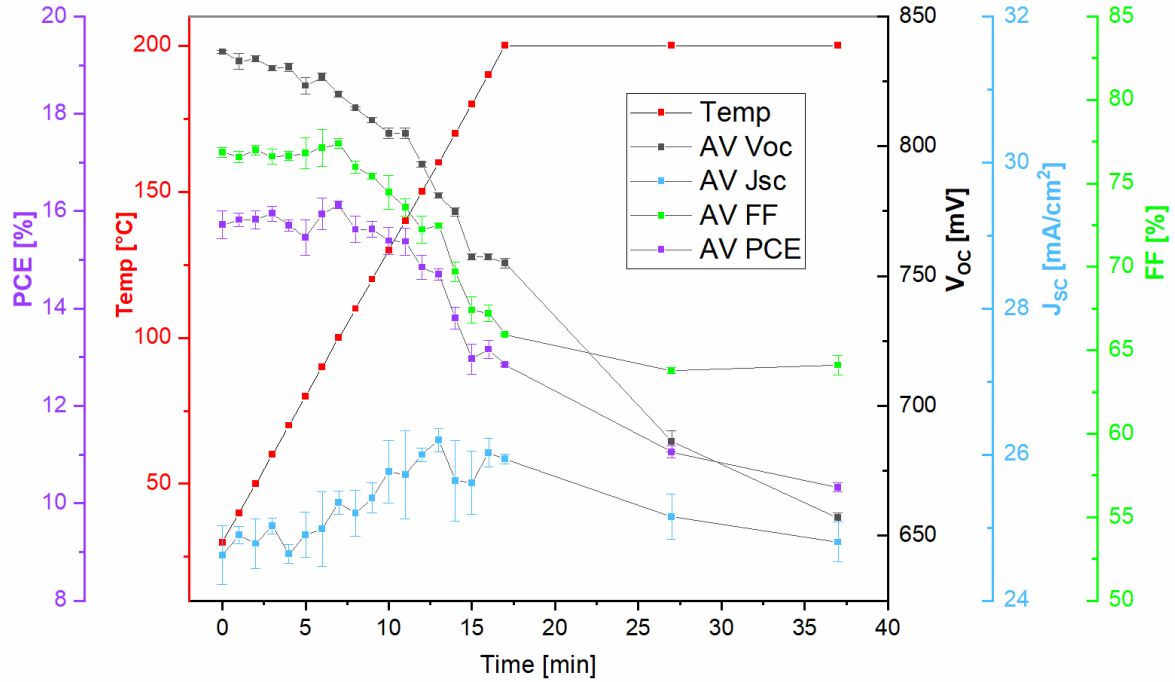


Figure 8: Investigation of the annealing step; the average (av) parameters of three devices are shown for each step.

Figure 8 shows the obtained values of the PCE, V_{OC} , J_{SC} and FF plotted against temperature and time, respectively. The corresponding data including the standard deviations are listed in Table 2. The solar cells prepared without annealing reveal an efficiency of 15.7%. During the heating run, the PCE reaches a maximum of 16.1% after seven minutes at 100°C and decreases to 10.3% after 20 minutes holding time at 200°C. Generally, it is observed that the PCE stays above 15% up to a temperature of 140°C of the surface of the heating plate. At higher temperatures, a significant decrease in PCE is observed.

It is also interesting to note that the maximum of the V_{OC} (836 mV) is obtained in devices without annealing, remaining almost constant during the heating run up to 70°C and then dropping almost linearly to a value of 657 mV after 37 minutes of heat treatment at 200°C. The FF, like the PCE, reaches its maximum at seven minutes, or at 100°C, with a value of $77.4 \pm 0.3\%$. In the further course of the heating run, it drops to about 64% by minute 27 at 200°C and then remains constant until the end of the test. The J_{SC} increases slightly from the beginning and reaches its maximum (26.2 mA/cm^2) after 13 minutes at 160°C. Only after a longer temperature treatment at 200°C, the J_{SC} slightly decreases, but interestingly, still comparatively high value of 24.8 mA/cm^2 was retained, which is even higher than in the solar cells without or with annealing at lower temperatures. This experiment provides very interesting insight into the changes of the solar cell properties based on different annealing temperatures of the active layer,

such as the facts that the reduced photovoltage and FF are the main drivers of a reduced PCE at higher temperatures above 140°C. Moreover, it should be noted that the best values obtained in this “heating-run” experiment match those of the devices prepared with the standard annealing (10 minutes annealing at 100°C), so the standard procedure was not changed for the following experiments.

Table 2: Results of the investigation of the annealing step.

T [°C]	t [min]	AV V _{oc} [V]	SD V _{oc}	AV J _{sc} [mA/cm ²]	SD J _{sc}	AV FF [%]	SD FF	AV PCE [%]	SD PCE
30	0	836	1	24.6	0.4	77	0.3	15.7	0.3
40	1	833	3	24.9	0.1	77	0.3	15.8	0.1
50	2	834	1	24.8	0.3	77	0.3	15.8	0.2
60	3	830	1	25.0	0.1	77	0.4	15.9	0.2
70	4	830	2	24.6	0.1	77	0.3	15.7	0.1
80	5	823	3	24.9	0.3	77	0.9	15.5	0.4
90	6	827	1	25.0	0.5	77	1.1	15.9	0.3
100	7	820	1	25.3	0.2	77	0.3	16.1	0.1
110	8	815	1	25.2	0.3	76	0.4	15.6	0.3
120	9	810	1	25.4	0.2	75	0.2	15.6	0.2
130	10	805	2	25.8	0.4	74	1.0	15.4	0.3
140	11	805	2	25.7	0.6	74	0.5	15.4	0.3
150	12	793	1	26.0	0.1	72	0.8	14.8	0.2
160	13	781	1	26.2	0.2	72	0.2	14.7	0.1
170	14	775	2	25.6	0.6	70	0.6	13.8	0.2
180	15	757	1	25.6	0.4	67	0.8	13.0	0.3
190	16	757	1	26.0	0.2	67	0.5	13.2	0.2
200	17	755	2	25.9	0.1	66	0.1	12.8	0.0
200	27	686	4	25.2	0.3	64	0.2	11.1	0.1
200	37	657	2	24.8	0.3	64	0.6	10.3	0.1

For a better understanding of the results of this experiment, the devices at room temperature, 100°C, 160°C, 200°C and at 200°C for 20 minutes, were examined in more detail by external quantum efficiency spectra, the investigation of the charge recombination properties, the exciton dissociation probability, and charge collection efficiency in the solar cells.

3.2.1 Influence of thermal annealing on the EQE spectra

Figure 9 shows the EQE spectra of the “heating run” experiment, from the devices at room temperature, and taken of the heating plate at 100°C, 160°C, 200°C and after 20 minutes at 200°C. The filled points in the EQE spectra are measured values and the unfilled points were estimated based on the UV-Vis spectra. Due to the usage of a Xenon-lamp as light source, no values could be measured in these wavelength regions because of intense peaks in the Xenon lamp spectrum at these wavelengths.

The characteristics of the different solar cells are very similar up to 800 nm, only the device, which was additionally exposed to a temperature of 200°C for 20 minutes, generates slightly less charge carriers over almost the whole wavelength range. Between approx. 820 and 950 nm, there is a clear difference between the solar cells obtained by different final temperatures. With higher temperature exposure, a shift to higher wavelengths can be seen, which also fits well with the slight increase of the J_{SC} (Figure 8) up to a certain point, since in total slightly more charge carriers are generated and it can be explained by the red shift in the absorption of Y6 in this region. This red shift is also very well visible in the UV-Vis spectra (chapter 3.5.1) and the EQE spectra (chapter 3.5.2) of the temperature stability tests.

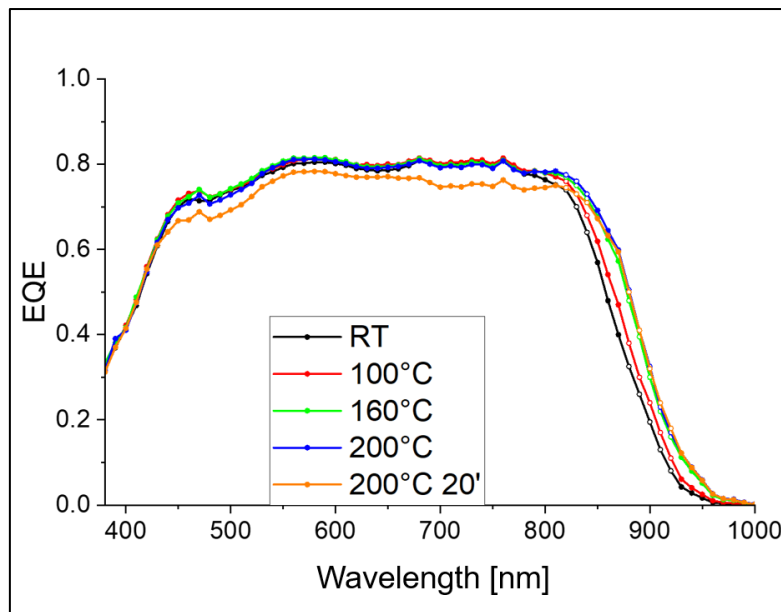


Figure 9: EQE spectra of the annealing step experiment of the devices at room temperature, 100°C, 160°C, 200°C and at 200°C for 20 minutes.

3.2.2 Dependency of J_{SC} and V_{OC} on the light intensity

Furthermore, changes in recombination properties in the solar cells based on the temperature treatment are investigated by light intensity dependent measurements of J_{SC} and V_{OC} .

First the light intensity dependence of J_{SC} was studied using light intensities of 100.0, 80.6, 51.8, 34.1, 29.6, 12.1, and 6.0 mW/cm^2 . The slope of the double logarithmic plot of the J_{SC} and light intensity, represents the alpha value. If the alpha value is 1, all dissociated free charge carriers are collected by the electrode, while values less than 1 suggest bimolecular recombination of imbalanced charge transport.⁷³

In Figure 10, the data are shown in a double-logarithmic plot (J_{SC} vs. light intensity) of the devices at room temperature, 100°C, 160°C, 200°C and at 200°C for 20 minutes. The results are obtained from a triple determination and all devices show an alpha value of 0.99. From this, it can be concluded that presumably in the area of the J_{SC} no bimolecular recombination is present and the charge transport and charge collection work well, even at higher annealing temperatures.⁷³

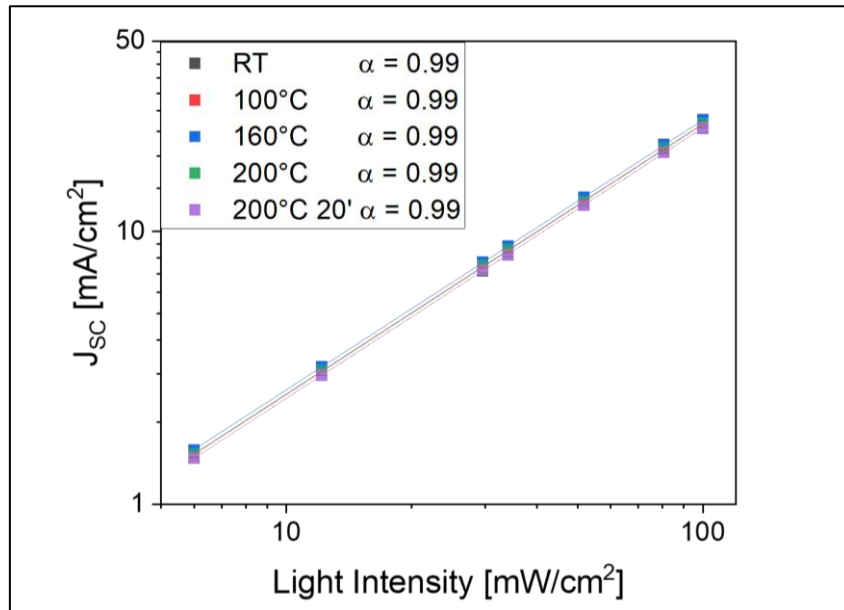


Figure 10: Dependence of the short-circuit current density on the light intensity of the device kept at room temperature and the devices taken of the heating plate during the heating run at 100°C, 160°C, 200°C and after 20 minutes at 200°C.

Furthermore, the n -values ($1 < n < 2$) are derived from the semi-logarithmic plot of the V_{OC} versus the light intensity. Pure bimolecular recombination happens in the V_{OC} area if this value is 1, and pure trap-assisted recombination is anticipated if this value is 2. A mixture of bimolecular and trap-assisted recombination is indicated by values between 1 and 2.⁷³

The dependence of the open circuit voltage of the respective devices of the “heating-run” experiment is shown in the semi-logarithmic plot in Figure 11. The results are formed from a triple determination and show an upward trend with the increase in temperature up to 200°C. The values for the solar cells without annealing and annealing at 100°C reveal an n-value of 1.27, which is well in line with ideality factors for PM6/Y6 solar cells reported in the literature,⁷⁴ and indicates low trap assisted recombination in these solar cells. Annealing at 160°C increases the value to 1.56 and the solar cell annealed at 200°C displays an n-value of 1.82. The increase in trap assisted recombination is expected based on the annealing at higher temperatures, which potentially leads to changes in the bulk heterojunction blend morphology and can also lead to a degradation of PM6 and/or Y6 leading to changes in the electronic properties. Interestingly, the ideality factor is again decreasing to 1.52 after 20 minutes annealing at 200°C, most likely due to a further rearrangement of the donor-acceptor morphology during the prolonged heating at the for conjugated polymers and NFAs comparably high temperature of 200°C.

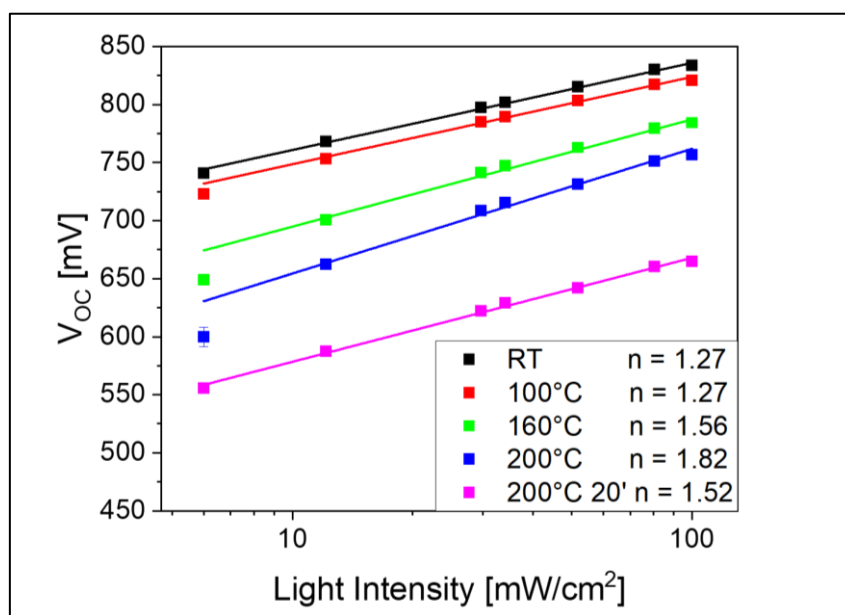


Figure 11: Dependence of the open circuit voltage of the device kept at room temperature and the devices taken of the heating plate during the heating run at 100°C, 160°C, 200°C and after 20 minutes at 200°C.

3.2.3 Exciton dissociation probability and charge collection efficiency

Studying the exciton dissociation probability and charge collection efficiency can give further hints about the changes caused by the different annealing temperatures. First, annealing at higher temperatures can lead to more pronounced phase separation, which can significantly diminish the donor/acceptor interface areas resulting in a lower probability of exciton dissociation and lower photovoltaic performance.⁷⁵ Second, it is also possible that higher temperature annealing induces changes directly at the interface of donor and acceptor such as a reduction of mixed donor/acceptor phases so that the domains become purer.

How the Exciton dissociation probability and charge collection efficiency were determined is described in more detail in chapter 5.9. The obtained data (see Figure 12, Table 3) reveal that the exciton dissociation probability decreases during the heating run in this experiment, however, the drop from 98 ± 1 to $93 \pm 1\%$ is lower than expected and it seems to stabilize after reaching 200°C as the holding time of 20 minutes does not lead to a further reduction of the exciton dissociation efficiency. A more pronounced effect is observed regarding the charge collection efficiency, which drops from $91 \pm 1\%$ for the sample without annealing and 100°C annealing to $79 \pm 1\%$ for the sample, which was on the hot plate for the entire heating run. This gives the hint that the annealing at higher temperatures has more impact on the charge transport than on the exciton dissociation.

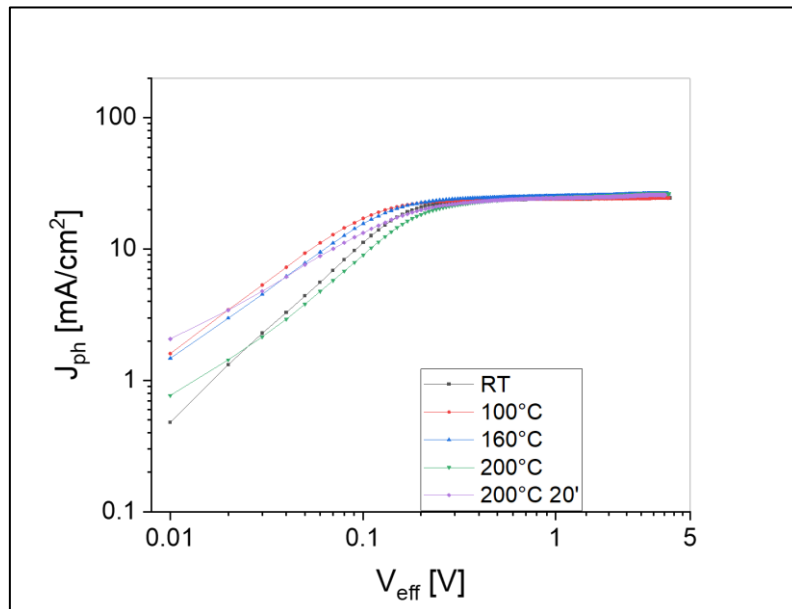


Figure 12: Exciton dissociation probability and charge collection efficiency of the device kept at room temperature and the devices taken of the heating plate during the heating run at 100°C , 160°C , 200°C and after 20 minutes at 200°C .

Interestingly, the annealing at temperatures up to 100°C has only a very minor effect on the properties of the solar cells. The photovoltage decreases slightly, while the short circuit current density slightly increases. The FF keeps unchanged, which leads to an only minor change in the PCE. Also, recombination properties, exciton dissociation probability and charge collection efficiency do not change upon a short annealing within this temperature range.

Table 3: Exciton dissociation probability and charge collection efficiency of the device kept at room temperature and the devices taken of the heating plate during the heating run at 100°C, 160°C, 200°C and after 20 minutes at 200°C; the average values are determined from three individual solar cells, respectively.

	AV n_{diss} [%]	SD [%]	AV n_{coll} [%]	SD [%]
RT	98	1	91	1
100°C	98	1	91	1
160°C	96	1	87	1
200°C	93	1	80	1
200°C 20'	94	1	79	1

3.3 Temperature stability tests of the binary PM6/Y6 system

To explore the temperature stability over an extended timeframe, solar cells were placed on a heating plate at 50°C and 100°C for 1020 minutes. Therefore, 20 standard PM6/Y6 solar cells with a PCE above 15% were fabricated and characterized before and after the exposure to 50°C and 100°C for 1020 minutes, respectively.

Table 4: Parameters of the solar cells of the binary PM6/Y6 system before and after temperature treatment at 50°C for 1020 minutes. The average values and standard deviations are calculated from 10 solar cells. The parameters of the single solar cells are listed in the appendix (Table 13).

Binary System	V_{OC} [mV]	J_{SC} [mA/cm ²]	FF [%]	PCE [%]	R_s [Ω]	R_p [k Ω]
RT	814 \pm 4	25.5 \pm 0.5	77.1 \pm 0.3	16.0 \pm 0.4	2.1 \pm 0.1	1.5 \pm 0.2
1020' 50°C	811 \pm 3	25.7 \pm 0.6	75.8 \pm 0.4	15.7 \pm 0.4	2.1 \pm 0.1	1.3 \pm 0.1
Change [%]	-0.3	1.8	-1.7	-1.9	0.0	-13.3

The devices show excellent temperature stability at 50°C for 1020 minutes, as can be seen in Table 4. The mean values of the V_{OC} remained very similar with 814 and 811 mV and a standard deviation of 4 and 3 mV, respectively. The same is true for the J_{SC} , which did not change significantly from 25.5 \pm 0.5 to 25.7 \pm 0.6 mA/cm². Also, no significant change was observed in the PCE, which decreased slightly from 16.0 \pm 0.4 to 15.7 \pm 0.4%. A more distinct change was perceived in the FF, which decreased from 77.1 \pm 0.3 to 75.8 \pm 0.4 after the temperature exposure to 50°C for 1020 minutes. The series resistance remained exactly the same with a value of 2.1 \pm 0.1 Ω , but the parallel resistance decreased by 13.3% to a value of 1.3 \pm 0.1 k Ω , which could also be responsible for the slightly lower FF.

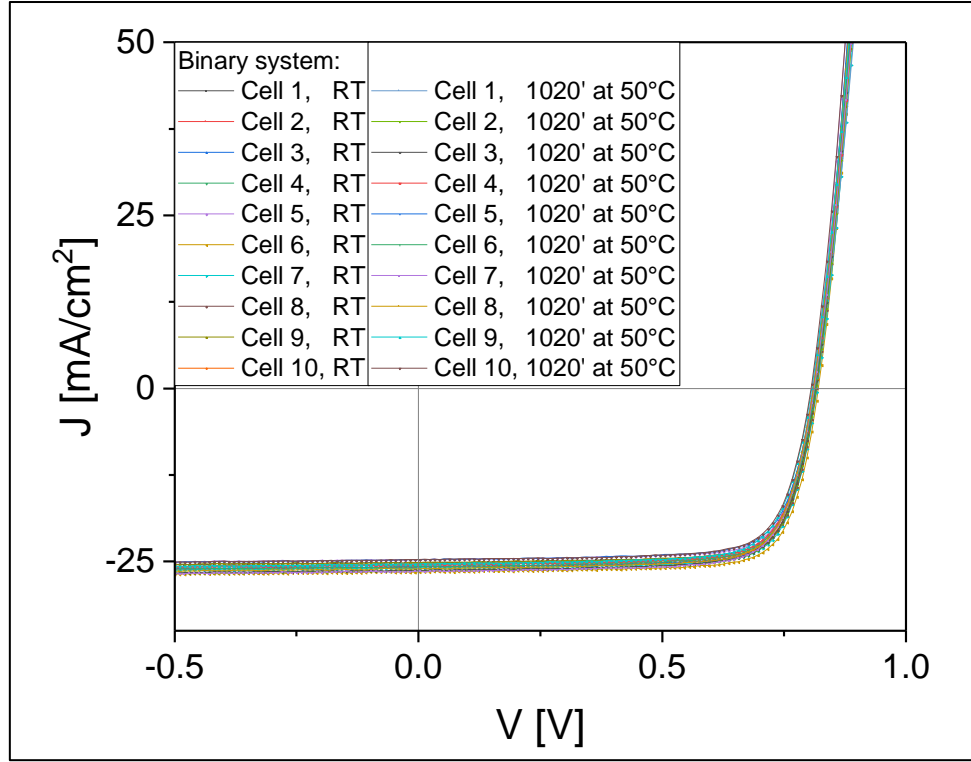


Figure 13: JV characteristics of the 10 binary PM6/Y6 devices, 10 curves before temperature treatment and the 10 curves of the same devices after 50°C for 1020 minutes.

Overall, it can be said that the binary devices are very stable at 50°C for 1020 minutes, which is also well illustrated by the JV characteristics depicted in Figure 13, where the 20 current-voltage characteristics, 10 before and the same 10 devices after the 50°C treatment for 1020 minutes, are presented. These devices show very similar characteristics, however the situation is different at a temperature treatment of 100°C for 1020 minutes. For that, again 10 standard binary devices with a PCE of over 15% were measured before and after a temperature treatment at 100°C for 1020 minutes.

Table 5: Parameters of the solar cells of the binary PM6/Y6 system before and after temperature treatment at 100°C for 1020 minutes. The average values and standard deviations are calculated from 10 solar cells. The parameters of the single solar cells are listed in the appendix (Table 14).

Binary System	V_{OC} [mV]	J_{SC} [mA/cm ²]	FF [%]	PCE [%]	R_s [Ω]	R_p [k Ω]
RT	820 \pm 3	25.5 \pm 0.6	75.9 \pm 0.5	15.9 \pm 0.4	2.1 \pm 0.1	1.4 \pm 0.2
1020' 100°C	795 \pm 3	25.4 \pm 0.5	68.0 \pm 0.4	13.7 \pm 0.4	2.7 \pm 0.1	0.6 \pm 0.1
Change [%]	-3.1	-0.4	-9.9	-13.8	28.6	-57.1

As can be seen in Table 5, each value changed significantly except for the J_{SC} , which even after the temperature exposure of 100°C for 1020 minutes, has nearly the same value above 25 mA/cm², which matches well with the “heating-run” experiment (chapter 3.1), where the J_{SC} also did not markedly decrease even at an annealing temperature of 200°C. Due to the decrease of V_{OC} , and FF, the PCE deteriorated by 13.8% in relative terms to an absolute efficiency value

of $13.7 \pm 0.4\%$ compared to the initial value of $15.9 \pm 0.4\%$. A moderate but still significant deterioration is observed in the V_{OC} , from 820 ± 3 to 795 ± 3 , which represents a relative voltage loss of 3.1%. The fill factor lost relatively almost 10% and decreased to $68.0 \pm 0.4\%$. Very strong changes were observed in series and parallel resistance. The series resistance increased from 2.1 ± 0.1 to $2.7 \pm 0.1 \Omega$ and thus relatively by 28.6%. The value of the parallel resistance was more than halved and worsened relatively by 57.1% to an absolute value of $0.6 \pm 0.1 \text{ k}\Omega$. Due to the strong changes of the two resistances and the fill factor, it is no longer possible to achieve a high efficiency. Figure 14 shows all 20 JV curves of the binary solar cells, before and after 1020 minutes at 100°C . The change in the shape of the characteristic curves clearly shows the deterioration of the V_{OC} , FF and PCE, with the J_{SC} remaining more or less the same.

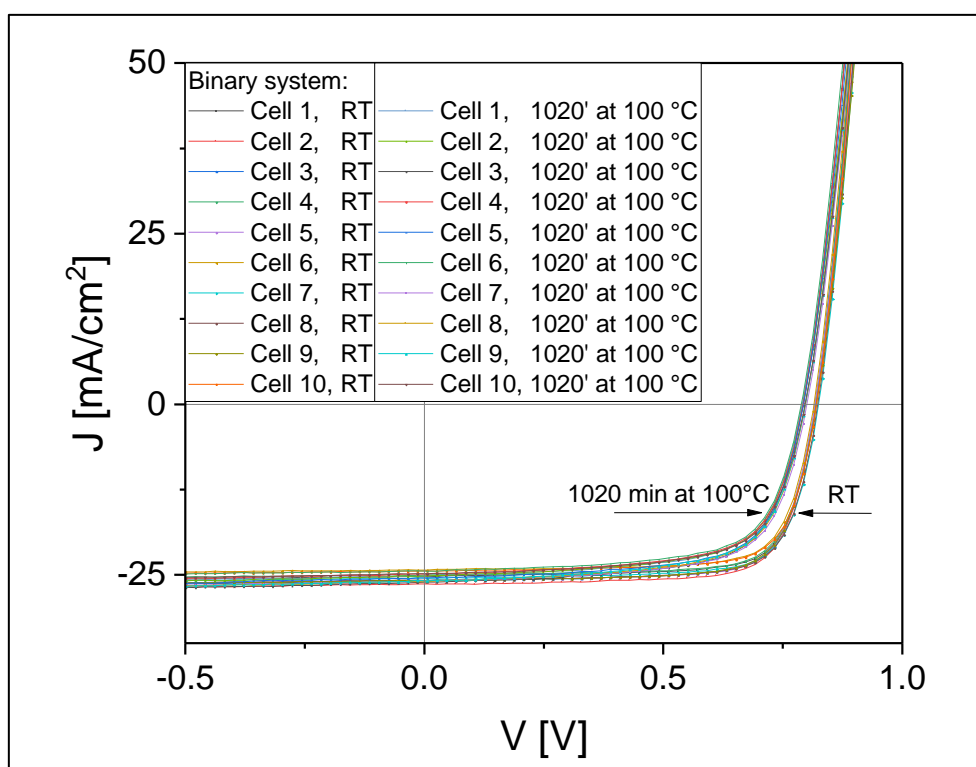


Figure 14: JV characteristics of the 10 devices, 10 curves before temperature treatment and the 10 curves of the same 10 devices after 100°C for 1020 minutes.

It can be said that the binary OSCs with a PM6/Y6 absorber layer blend are susceptible for degradation based on exposure to higher temperatures, i.e. 100°C . However, at low temperature of 50°C , even over a longer period of time, this system seems to be quite stable. Based on these experiments, the idea arose to integrate a second acceptor into the existing standard system. As a result, instead of PM6/Y6 absorber layers, a ternary system with an additional small amount of a fullerene acceptor (PC_{71}BM) was tested.

3.4 Ternary System based on the absorber materials PM6, Y6 and PC₇₁BM

The ternary system was built with one donor, PM6, and two acceptors, Y6 and PC₇₁BM, with a weight ratio of 1 to 1 to 0.2 (PM6/Y6/PC₇₁BM). The design and fabrication were otherwise the same as those of the binary system. The characteristic curve of the ternary record cell is shown in Figure 15. A PCE of 16.5% was obtained, with a V_{OC} of 824 mV, a J_{SC} of 26.0 mA/cm² and a FF of 77%. At the MPP, the solar cell operates at a voltage of over 700 mV and a current density of 23.4 mA/cm². For the following tests, similar to the devices of the binary system, only solar cells with a PCE of more than 15% were used for the temperature aging tests.

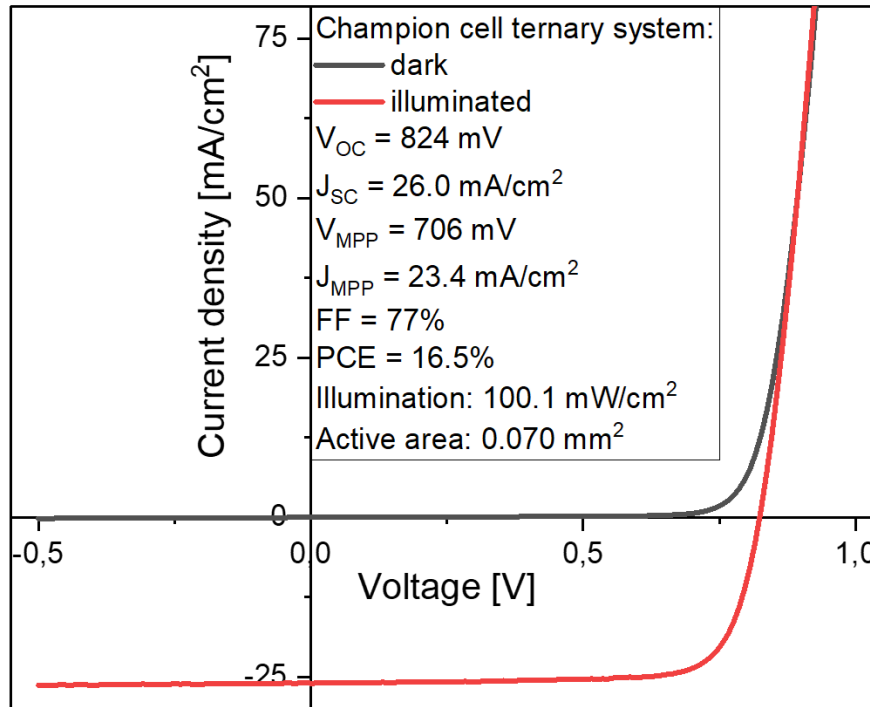


Figure 15: JV curves in the dark and under illumination and the characteristic parameters of the champion cell of the ternary PM6/Y6/PC₇₁BM system.

3.5 Temperature stability tests of the ternary PM6/Y6/PC₇₁BM system

To investigate temperature stability, similar to the experiments performed with the binary system, 20 standard devices with a PCE greater than 15% were built. Subsequently, 10 devices were characterized via recording of JV curves without temperature treatment and after expose to 50°C for over 1020 minutes and the other 10 devices also were measured without and with a temperature treatment at 100°C for 1020 minutes. Like the binary system, the ternary system shows very good temperature stability at 50°C for 1020 minutes as shown in Table 6.

Table 6: Parameters of the solar cells of the ternary PM6/Y6/PC₇₁BM system before and after temperature treatment at 50°C for 1020 minutes. The average values and standard deviations are calculated from 10 solar cells. The parameters of the single solar cells are listed in the appendix (Table 15).

Ternary System	V _{OC} [mV]	J _{SC} [mA/cm ²]	FF [%]	PCE [%]	R _s [Ω]	R _p [kΩ]
RT	820 ± 2	24.7 ± 0.6	76.6 ± 0.7	15.7 ± 0.4	2.3 ± 0.1	1.4 ± 0.3
1020' 50°C	813 ± 2	25.1 ± 0.8	76.0 ± 1.0	15.5 ± 0.5	2.4 ± 0.2	1.2 ± 0.2
Change [%]	-0.9	1.6	-0.8	-1.3	4.3	-14.3

Only the V_{OC} changed significantly, with a decrease of relatively 0.9%, from 820 ± 2 to 813 ± 2 mV. The other values, J_{SC}, PCE, FF, R_s, and R_p remained within the standard deviation range and thus did not change significantly.

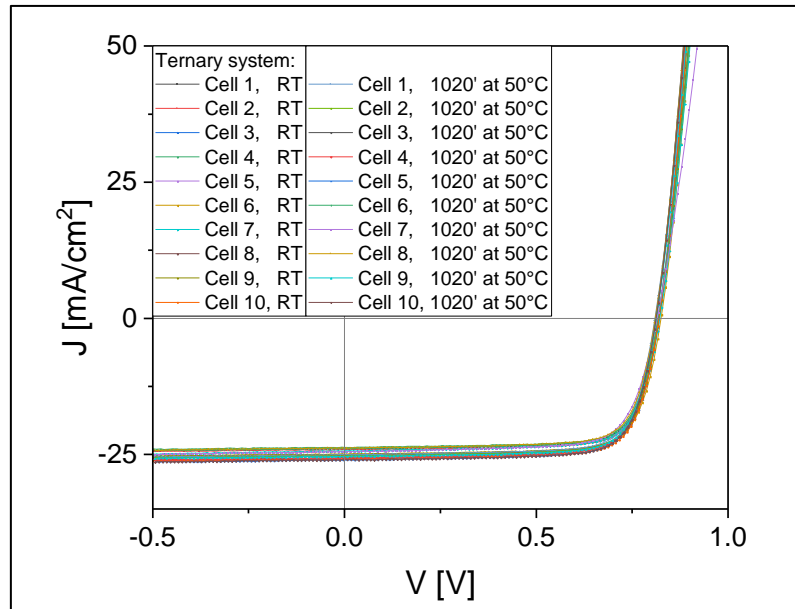


Figure 16: Characteristics of the 10 ternary PM6/Y6/PC₇₁BM devices, 10 curves before temperature treatment and the 10 curves of the same devices after 50°C for 1020 minutes.

The 20 characteristics of the untreated 10 devices and the 10 curves of the same devices temperature treated at 50°C for 1020 minutes, can be seen in Figure 16. All 20 curves show the

same behavior and it is evident from the graph that the ternary devices also have very good temperature stability at 50°C.

Similar to the binary system, after a temperature exposure of 100°C for 1020 minutes, the solar cell properties change distinctly.

Table 7: Parameters of the solar cells of the ternary PM6/Y6/PC₇₁BM system before and after temperature treatment at 100°C for 1020 minutes. The average values and standard deviations are calculated from 10 solar cells. The parameters of the single solar cells are listed in the appendix (Table 16).

Ternary System	V _{OC} [mV]	J _{SC} [mA/cm ²]	FF [%]	PCE [%]	R _s [Ω]	R _p [kΩ]
RT	832 ± 3	24.2 ± 0.5	77.0 ± 0.3	15.7 ± 0.4	2.1 ± 0.1	1.6 ± 1.4
1020' 100°C	793 ± 2	25.0 ± 0.6	72.2 ± 0.5	14.4 ± 0.4	2.5 ± 0.1	1.0 ± 0.1
Change [%]	-4.7	3.3	-6.2	-8.3	19.0	-37.5

Also in the ternary system, all values, except for the J_{SC}, changed significantly (see Table 7). The V_{OC} was reduced relatively by 4.7% to a value of 793 ± 2 mV. The J_{SC} increased from 24.2 ± 0.5 to 25.0 ± 0.6 mA/cm². The FF deteriorated relatively by 6.2% to an absolute value of 72.2 ± 0.5%, the PCE fell to an absolute value of 14.4 ± 0.4% and thus decreased relatively by 8.3%. Relatively, R_s and R_p changed the most, with R_s increasing by 19% and R_p decreasing by over 37%. Figure 17 shows all 20 curves of the same 10 ternary devices, non-annealed and after 1020 minutes at 100°C. The change in the shape of the characteristic curves clearly shows the deterioration of the V_{OC}, FF and PCE, with the J_{SC} remaining almost unchanged as it was also observed in the binary PM6/Y6 based devices.

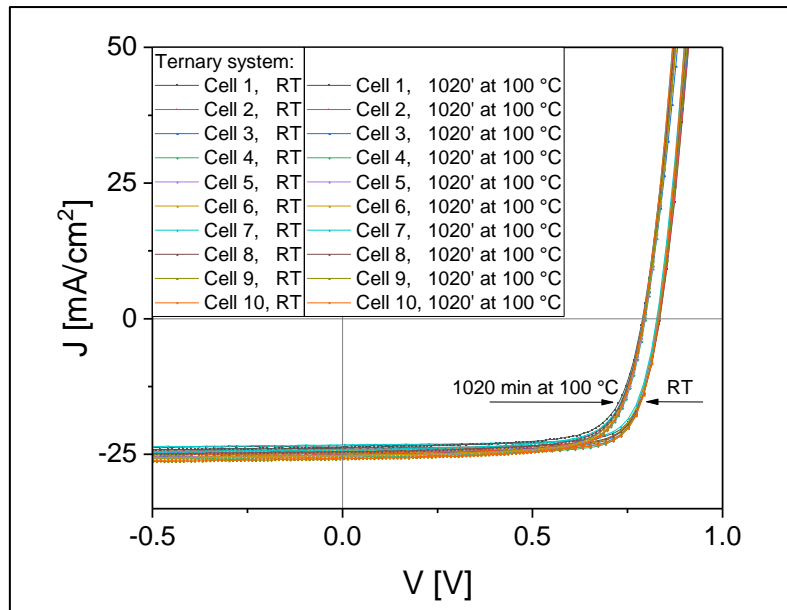


Figure 17: Characteristics of the 10 ternary devices, 10 curves before temperature treatment and the 10 curves of the same devices after 100°C for 1020 minutes.

3.6 Comparison of the temperature stability tests

To illustrate the difference between the binary and ternary systems in the quantitative changes of the solar cell parameters, the mean values and standard deviations of the two systems are summarized and compared in the following Figure 18.

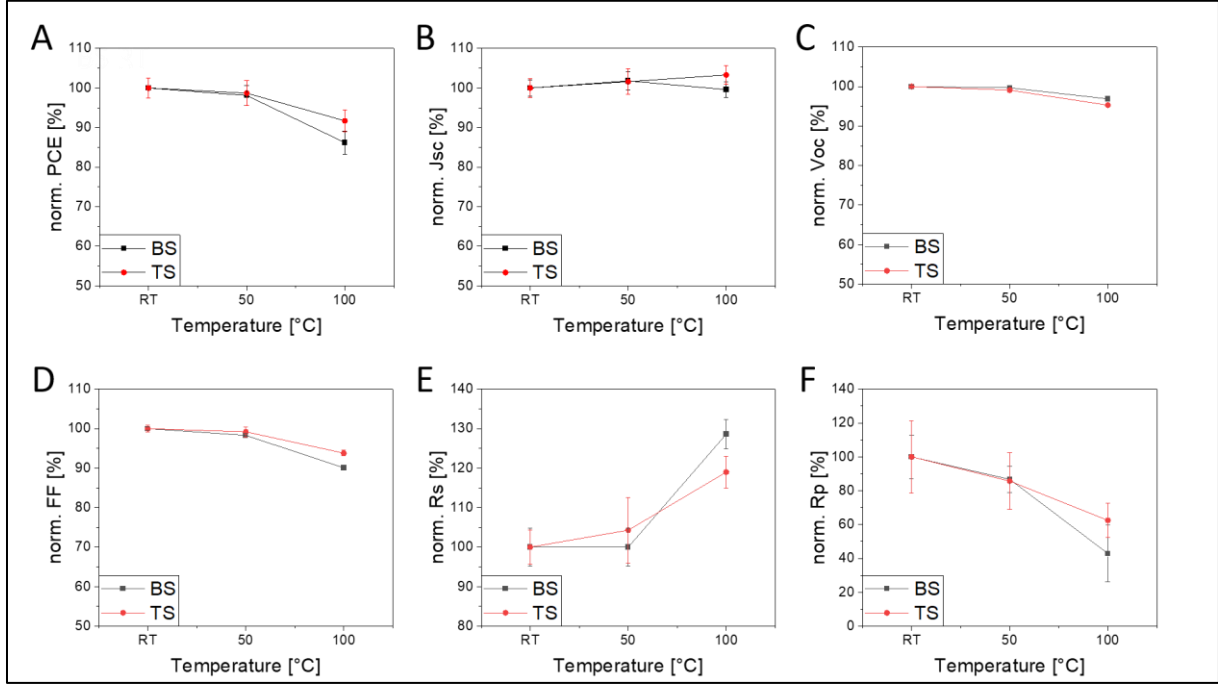


Figure 18: Comparison of the binary and ternary system at room temperature, 50 and 100°C for 1020 minutes of PCE (A), Jsc (B), Voc (C), FF (D), Rs (E) and Rp (F).

The untreated 20 devices are very well comparable because the average efficiency of $15.9 \pm 0.4\%$ of the binary system and that of the ternary system with $15.7 \pm 0.4\%$ are very similar.

Real differences between the binary and ternary systems at 1020 minutes at 50°C are not apparent, the behavior is still very similar. In contrast, at a temperature of 100°C for 1020 minutes, differences between the binary and ternary systems become visible. The ternary system seems to cope better with the effect of 100°C, because the PCE, Figure 18A, loses 8.3% in relative terms, but the binary system deteriorates by 13.8% in relative terms. The Jsc, Figure 18B, increases slightly by 3.3% for the ternary system, whereas the Jsc drops minimally by 0.4% for the binary system. With respect to Voc (Figure 18C) a slight decrease is observed for both systems. The fill factor (Figure 18D) drops quite sharply by 9.9% (relative) in the binary system, compared to a drop of only 6.2% in the ternary solar cells. This is also reflected by the strong increase of 28.6% for the Rs (Figure 18E) and the strong decrease of 57.1% for the Rp (Figure 18F). The lower decrease of the FF in the ternary system is also associated with a weaker increase in the Rs of 19.0% and a weaker decrease in the Rp of 37.5% (relative).

To obtain indications for these changes, further analyses were made in order to possibly take advantage of them in future device fabrication.

3.6.1 Optical properties – UV-Vis spectroscopy

Figure 19 below shows the normalized absorption spectra of pristine PM6 thin films at room temperature and after exposure to a temperature of 50 and 100°C for 1020 minutes. The spectra reveal a prominent peak with a maximum at 624 nm and a second local maximum at 580 nm. The positions of these maxima do not change with the temperature exposure. It is easy to see that there is no shift, but at the peak at 580, it is noticeable that the intensity is highest for the layers without thermal aging and drops a little due to the temperature treatment at 50 and 100°C for 1020 minutes.

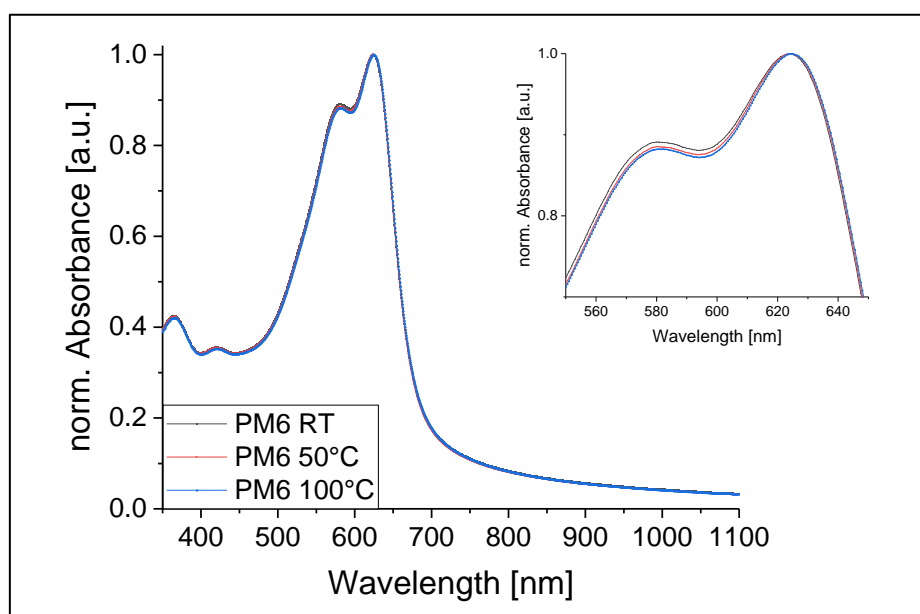


Figure 19: UV-Vis absorption spectra of the pure PM6 layer at room temperature and after 1020 minutes at 50 and 100°C.

Figure 20 shows the spectra of pristine Y6 films at room temperature, and after exposure to 50 and 100°C for 1020 minutes. Y6 absorbs in a very broad wavelength range and forms its main peak between 600 and almost 1000 nm. The peak maximum is at 817 to 818 nm for the layers without further temperature exposure and does not shift after 1020 minutes exposure to 50°C. However, after thermal aging of 1020 minutes at 100°C, a slight red shift can be seen, with the new maximum being at 820 to 821 nm. This is also clearly visible in the zoomed insert in the Figure.

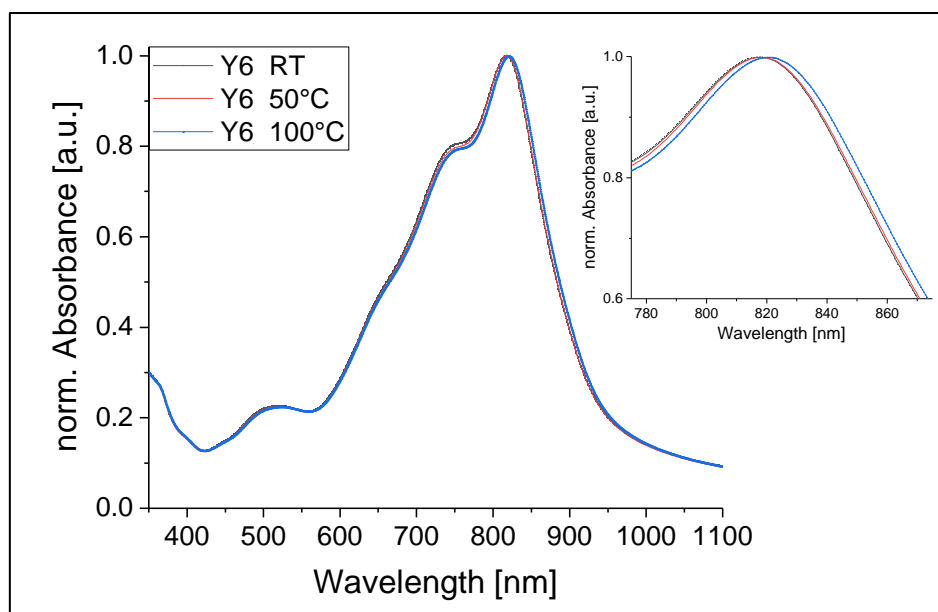


Figure 20: UV-Vis absorption spectra of the pure Y6 layer at room temperature and after 1020 minutes at 50 and 100°C.

The absorption spectrum of the binary PM6/Y6 absorber layer blend in Figure 21 shows the very good absorption ability of this system. Again, the spectra at room temperature and after thermal aging at 50 and 100°C for 1020 minutes each are shown. The first peak maximum is at 628 nm and has shifted by 4 nm compared to the pure PM6 layer. This small red shift is the same for the layers without and with temperature aging. The main peak of Y6 in this spectrum of the binary layer looks a bit different. The peak maximum is at 810 nm for the layers without temperature treatment and for those exposed to 50°C for 1020 minutes, which means a blue shift of about 7 nm compared to the pure Y6 layers. The peak maximum of the coatings exposed to a temperature aging of 100°C for 1020 minutes is 816 to 817 nm, compared to 820 to 821 nm for the pure Y6 coatings exposed to the same temperature.

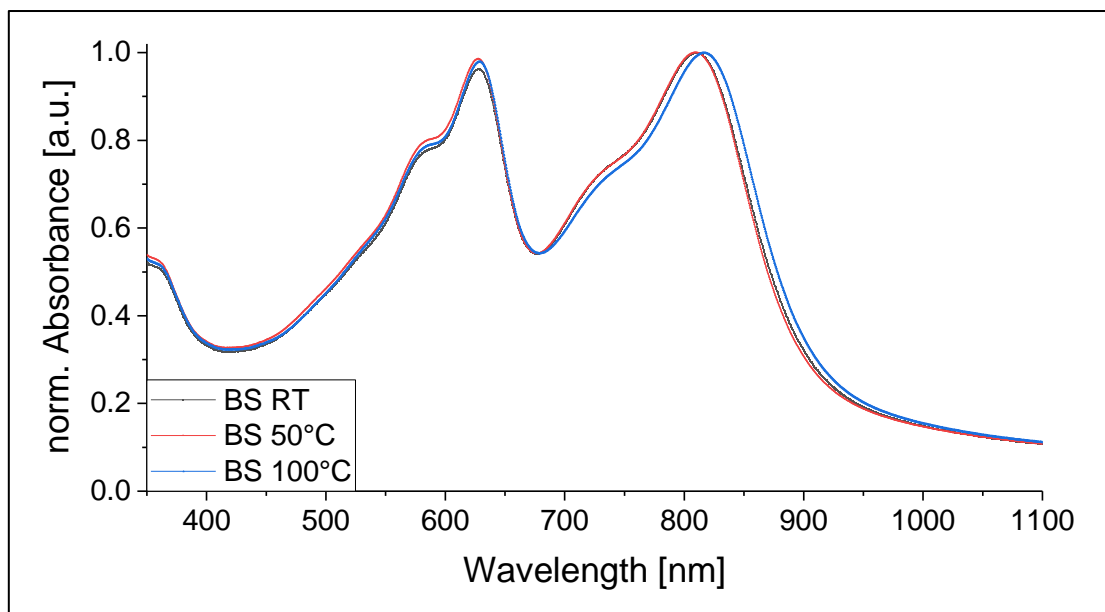


Figure 21: UV-Vis absorption spectra of the binary layer at room temperature and after 1020 minutes at 50 and 100°C.

In the following Figure 22, the absorption spectra of the ternary layers, PM6/Y6/PC₇₁BM, are shown for the untreated layers and those with temperature loading of 50 and 100°C for 1020 minutes. Again, as with the binary films, the first peak maximum is at 628 nm and has a red shift of 4 nm compared to the pristine PM6 films. The temperature treatment also did not change the maximum at 628 nm. Similar to the binary layers, for the untreated layers and those at 50°C for 1020 minutes, the second maximum (stemming from the Y6-absorption) is at 810 nm and has a blueshift of 7 nm compared to the pristine Y6 layers. The peak maximum of the layers subjected to thermal aging at 100°C for 1020 minutes is at 818 to 819 nm for the ternary layers and is a little closer to that of the Y6 pure layers compared to the binary layers. Due to the red shift of the Y6 peak in the layer with a thermal aging of 100°C, the absorption is decreased between 680 and 818 nm, but increased from 818 nm to higher wavelengths.

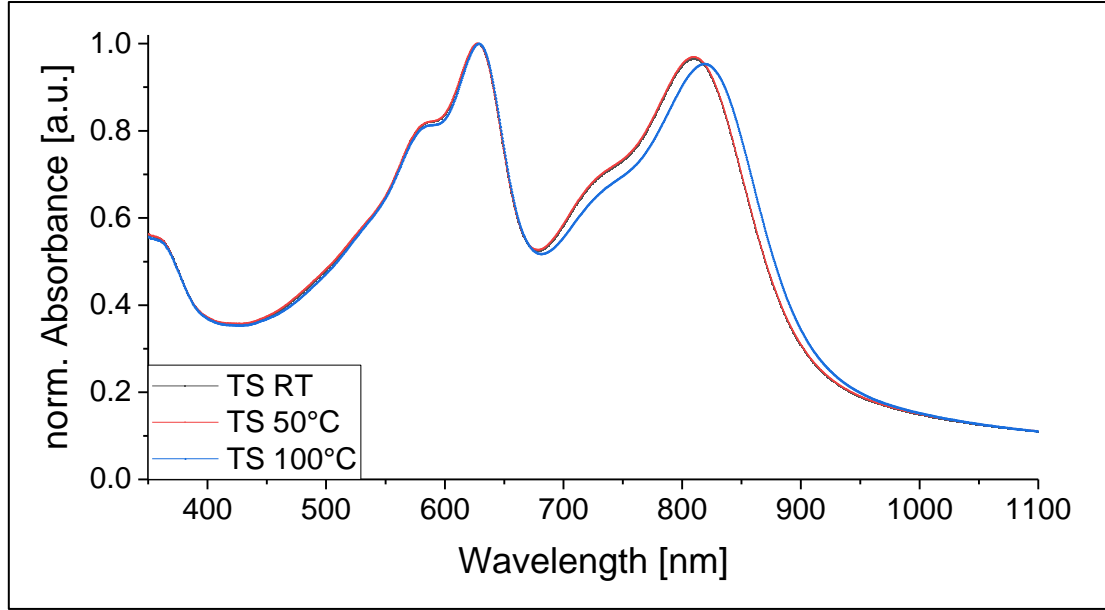


Figure 22: UV-Vis absorption spectra of the ternary layer at room temperature and after 1020 minutes at 50 and 100°C.

3.6.2 EQE spectra

The EQE results from the ratio of the charge carriers generated by the device, which arrive at the electrodes, to the incident energy, the photons at a certain wavelength. Figure 23 below compares the EQE spectra of binary devices without and with temperature treatment for 1020 minutes at 50 and 100°C, respectively. It can be seen that the charge carrier generation is very efficient over a wide wavelength range, from about 400 to 900 nm. The spectrum of the untreated device (black line) and that with gentle thermal aging, 50°C for 1020 minutes (red line), have a very similar profile. This is also supported by the respective UV-Vis spectra, the very similar hole and electron mobilities (see chapter 3.5.3) and the performance of the devices. As mentioned in Section 3.1.1, in Figure 23 and 24 the filled points are also actual measurements and the unfilled ones were estimated from the UV-Vis spectra.

The spectrum of the solar cell, which was exposed to a temperature load of 100°C for 1020 minutes (blue line), shows some differences. Between 410 and 815 nm, slightly fewer charge carriers are generated. This might be associated with a decreased electron mobility. Moreover, due to the further crystallization of Y6 (chapter 3.6.8) based on the temperature exposure the charge transfer at the interface of PM6/Y6 can be slightly impaired. And in addition, it was found that the mobility ratio, μ_h to μ_e , increases by more than a factor of 10 from 0.7 to 7.9 due to thermal aging at 100°C, showed in chapter 3.6.3. The slightly higher carrier generation between approx. 820 and 950 nm can be explained by the red shift in the absorption of Y6 in this region (chapter 3.6.1).

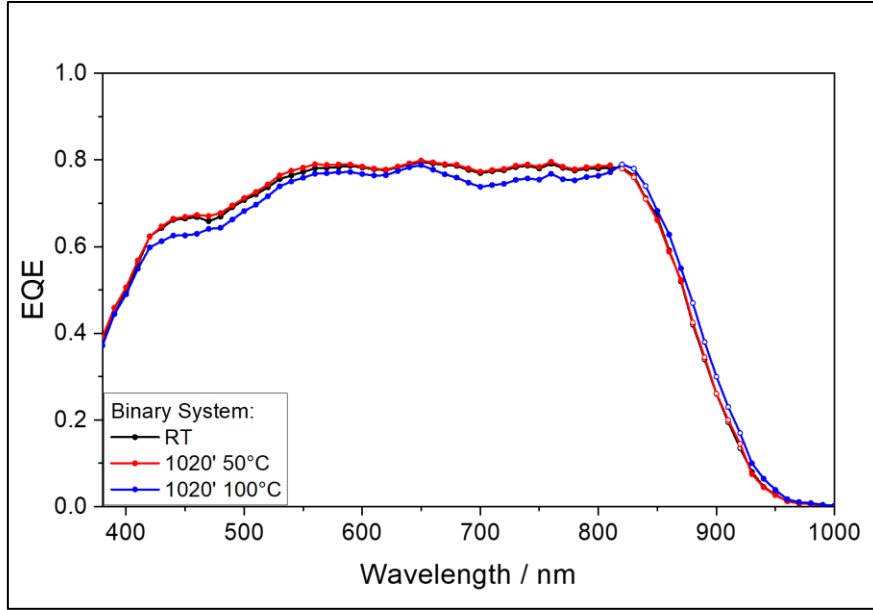


Figure 23: EQE spectra of the binary system at room temperature and after 1020 minutes temperature treatment at 50°C and 100°C.

In case of the ternary devices, between 440 and 820 nm, the devices exposed to 50°C for 1020 minutes generate a little less charge carrier, but the devices exposed to 100°C generate even less. This effect with the 100°C aged devices has already been observed with the binary devices, but to a lesser extent. The lower charge carrier density in this region could be due to the reduced absorption visible in the UV/Vis images (chapter 3.6.1). A higher crystallinity of the Y6 and a reduced charge transport are also possible (chapter 3.6.8). In addition, for the devices aged at 100°C, an increase in the mobility ratio, μ_h to μ_e , by a factor of about 17, from 0.7 to 12, is observed (chapter 3.6.3). Due to the higher absorption in the region after 820 nm, the devices aged at 100°C generate more charge carriers in this region than the devices without temperature stress and those exposed to only 50°C for 1020 minutes, Figure 24.

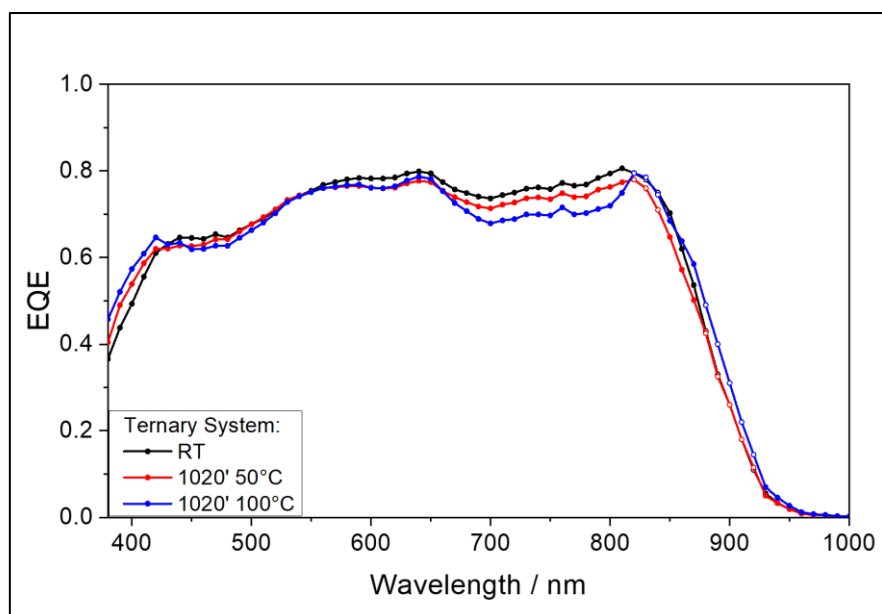


Figure 24: EQE spectra of the ternary system at room temperature and after 1020 minutes temperature treatment at 50°C and 100°C.

3.6.3 Hole and electron mobility

In order to calculate the hole and electron mobilities, μ_h and μ_e , hole- and electron-only devices were built, measured and then evaluated with the space charge limited current (SCLC) methode.⁷⁶ The exact procedure is explained in chapter 5.7.

The characteristics of typical hole and electron only devices together with the fits between 1 and 2 V are depicted in Figure 25.

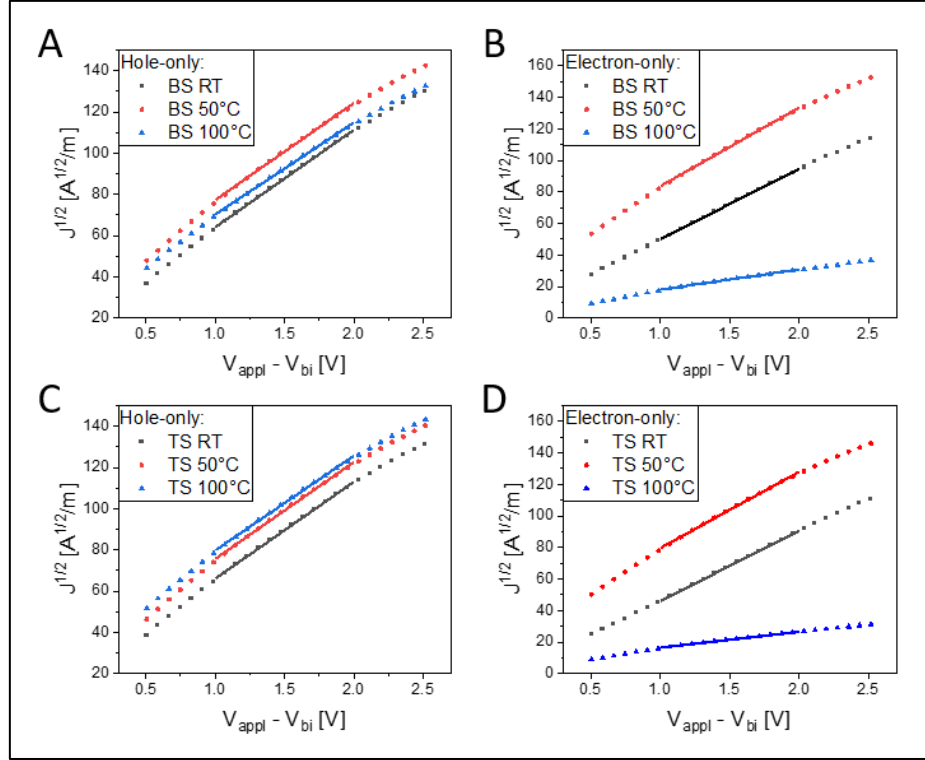


Figure 25: $J^{1/2} / V$ plots of the hole- (A, C) and electron-only (B, D) measurements of the binary and ternary system.

Table 8: Results of the hole and electron mobilities measurements.

	$\mu_h \cdot 10^{-4}$ [cm ² /Vs]	$\mu_e \cdot 10^{-4}$ [cm ² /Vs]	μ_h/μ_e
BS RT	2.3 ± 0.20	3.1 ± 0.33	0.7
BS 1020' at 50°C	2.3 ± 0.13	4.0 ± 0.31	0.6
BS 1020' at 100°C	2.0 ± 0.19	0.25 ± 0.02	7.9
TS RT	2.0 ± 0.12	3.0 ± 0.20	0.7
TS 1020' at 50°C	2.0 ± 0.05	3.3 ± 0.20	0.6
TS 1020' at 100°C	1.9 ± 0.12	0.15 ± 0.05	12.1

For the determination of the mobilities, five devices were evaluated and averaged and the results are presented in Table 8. The mobilities of the holes are very similar for the binary and ternary devices and values of about $2 \cdot 10^{-4}$ cm²/Vs are revealed. Even after a temperature treatment at 50 and 100°C for 1020 minutes, they do not change significantly.

For the binary devices the electron mobility changes from $3.1 \cdot 10^{-4}$ to $4.0 \cdot 10^{-4} \text{ cm}^2/\text{Vs}$ after 1020 minutes at 50°C and for the ternary devices there is no significant change to observe, it is nearly the same value as the value of the binary system and these changes are negligible.

The change at a temperature treatment of 100°C for 1020 minutes is, however, very significant. In this case, the electron mobility of the binary system is reduced to $0.25 \cdot 10^{-4} \text{ cm}^2/\text{Vs}$, which corresponds to a reduction by a factor of more than 10. In the case of binary devices, the ratio μ_h to μ_e increases from 0.7 to 7.9. This ratio increases a little more for ternary devices, from 0.7 to 12.1, an increase by a factor of 17. In absolute values, the electron mobility falls from $3.0 \cdot 10^{-4}$ to $0.15 \cdot 10^{-4} \text{ cm}^2/\text{Vs}$ at the temperature treatment of 100°C for 1020 minutes.

3.6.4 Light intensity dependent measurements of J_{SC} and V_{OC}

The light intensities used for the determination of the light intensity dependences of J_{SC} and the V_{OC} were 100.0, 80.6, 51.8, 34.1, 29.6, 12.1, and 6.0 mW/cm².

In case of the dependence of the J_{SC} , the alpha value is the slope in the double logarithmic plot, of J_{SC} and the light intensity, and can thus be determined graphically. If the alpha value is 1, all dissociated free charge carriers are collected by the electrode and values less than 1 indicate bimolecular recombination.⁷³

Figure 26 shows the short-circuit current density of the binary devices plotted versus the light intensity. Five measurements were performed in each case to obtain well-comparable results. Figure 26A shows the devices without temperature treatment, Figure 26B shows the results for the devices which were aged at 50°C for 1020 minutes. Figure 26C shows the results at 100°C for 1020 minutes and Figure 26D summarizes the results. All results show a linear relationship between J_{SC} and light intensity in the double logarithmic plot. All alpha values result in 1.0, indicating a very strong suppression of bimolecular recombination.⁷³

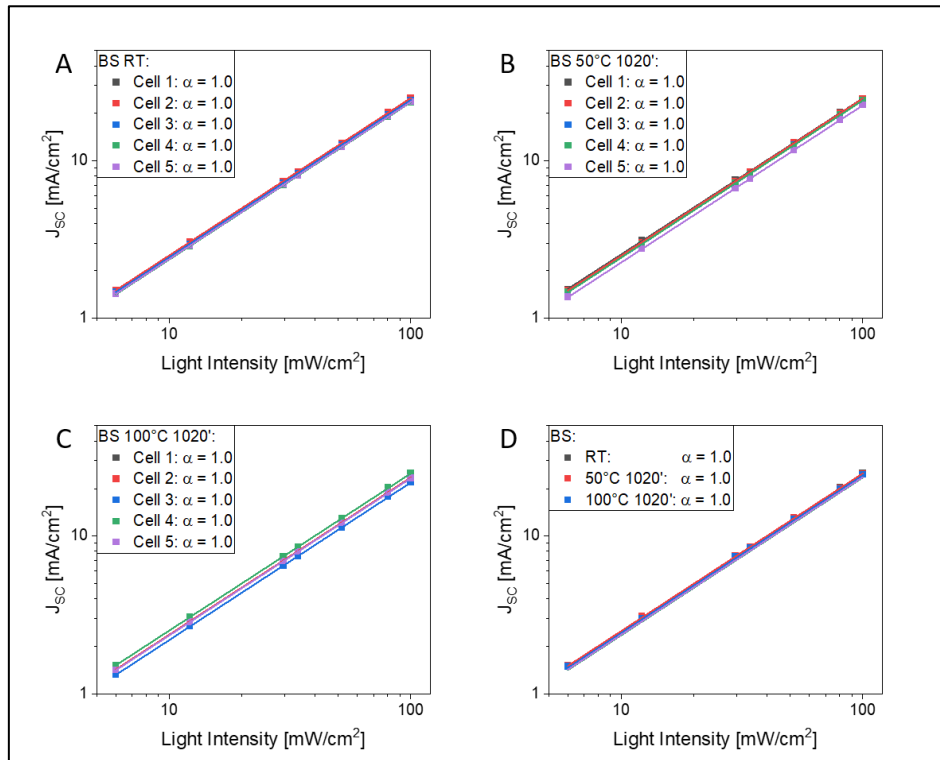


Figure 26: Dependence of the short-circuit current density of the binary devices on light intensity; devices without temperature stress (A), thermal aging at 50 (B) and 100°C (C) for 1020 minutes, summary of the results (D).

In Figure 27, the dependence of the short-circuit current density on the light intensity of the ternary devices is presented. Five measurements were performed in each case to obtain well-

comparable results. Figure 27A shows the devices without temperature treatment, Figure 27B shows the results for the devices which were aged at 50°C for 1020 minutes. Figure 27C shows the results at 100°C for 1020 minutes and Figure 27D summarizes the results. All results show a linear relationship between J_{SC} and light intensity in the double logarithmic plot. As before for the binary devices, all alpha values result in 1.0, indicating a very strong suppression of bimolecular recombination.⁷³

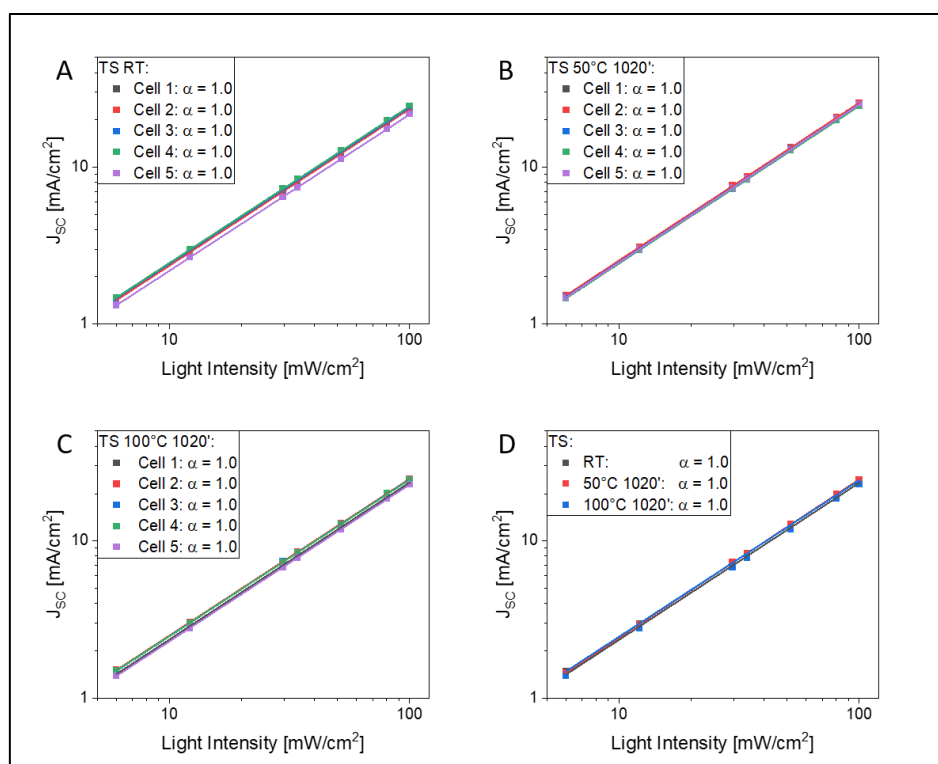


Figure 27: Dependence of the short-circuit current density of the ternary devices on light intensity; devices without temperature stress (A), thermal aging at 50 (B) and 100°C (C) for 1020 minutes, summary of the results (D).

To investigate the recombination in the open circuit voltage region also five measurements were performed in each case to obtain well-comparable results. In the following Figure 28, the determined n-values and the corresponding plot of the binary devices are shown. Figure 28A shows the evaluation devices without temperature treatment, Figure 28B and C show the evaluation of the devices with thermal aging of 50 and 100°C for 1020 minutes and Figure 28D shows a summary of the results.

No significant difference can be seen between the results of the binary devices. The n-value of the binary devices without thermal aging is 1.40 ± 0.02 , for the devices with thermal aging of 50°C for 1020 minutes the n-value is 1.38 ± 0.01 and for those devices with thermal aging at 100°C for 1020 minutes the n-value is 1.39 ± 0.02 . It is interesting to note, as can be seen in

Figure 28D, that even though the voltage is lower from the beginning of the measurement, the same slope or linear behavior is visible for the devices aged at 100°C. The recombination in the V_{OC} region is based on a mixture of bimolecular and trap-assisted recombination, as indicated by the obtained n-values.

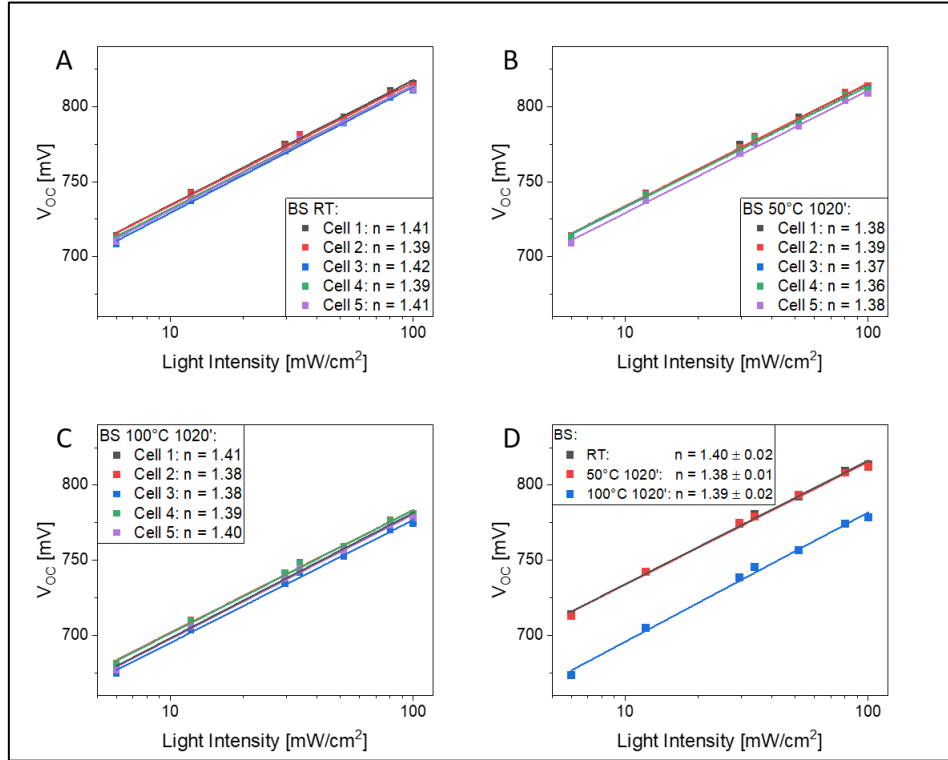


Figure 28: Dependence of the open-circuit voltage of the binary devices on light intensity; devices without temperature stress (A), thermal aging at 50 (B) and 100°C (C) for 1020 minutes, summary of the results (D).

Five measurements were performed in each case to obtain well-comparable results. In Figure 29, the determined n-values and the corresponding plot of the ternary devices are shown. Figure 29A shows the evaluation devices without temperature treatment, Figure 29B and C show the evaluation of the devices with thermal aging at 50 and 100°C for 1020 minutes and Figure 29D shows a summary of the results.

The n-value of the ternary devices without thermal aging is 1.30 ± 0.02 , for the devices with thermal aging of 50°C for 1020 minutes the n-value is 1.41 ± 0.01 and for those devices with thermal aging at 100°C for 1020 minutes the n-value is 1.40 ± 0.02 . Figure 29D clearly shows that the curve of the ternary devices without temperature stress differs from the others, also from the binary devices. The ternary devices with thermal aging at 50 and 100°C for 1020 minutes have the same n-values as the binary devices. Also, for the ternary devices, the V_{OC} of the devices aged at 100°C is a lower voltage but the trend remains. The lower n value in the ternary devices without temperature stress, compared to the binary devices and the thermally

aged ternary devices, could be because the additional PC₇₁BM facilitates electron transport in the absorber layer, thereby reducing trap-assisted recombination, but this fact seems to disappear due to thermal aging at 50 and 100°C.

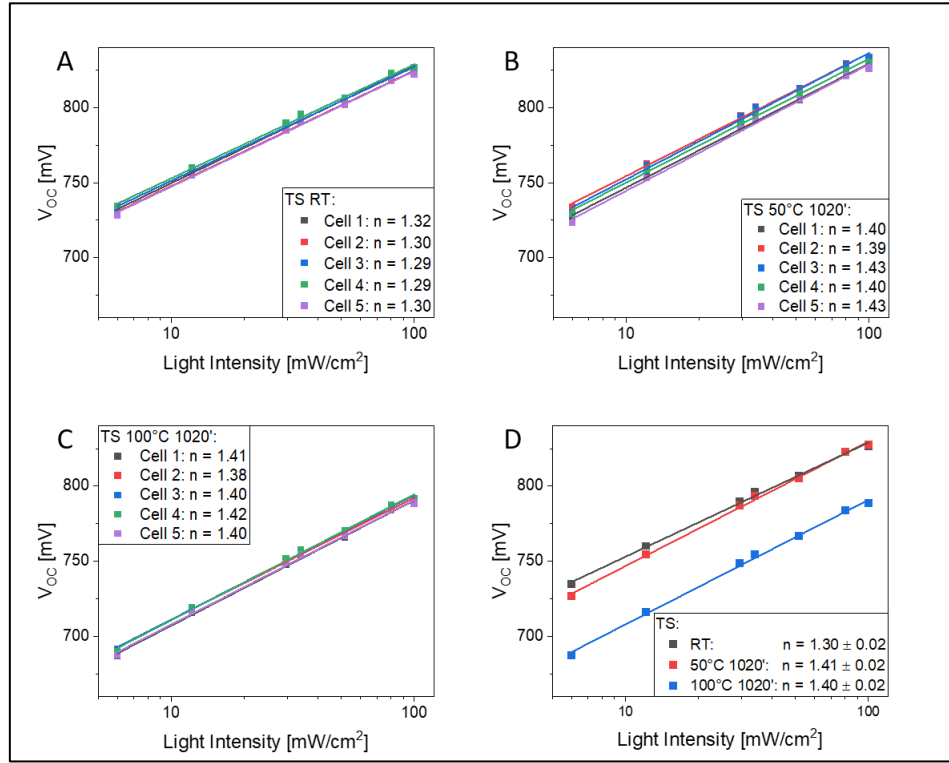


Figure 29: Dependence of the open-circuit voltage of the ternary devices on light intensity; devices without temperature stress (A), thermal aging at 50 (B) and 100°C (C) for 1020 minutes, summary of the results (D).

3.6.5 Exciton dissociation probability and charge collection efficiency

High interfacial areas are required for high exciton dissociation efficiency, which requires sufficiently close mixing of donors and acceptors. A certain amount of phase separation is necessary for successful charge extraction in order to move free holes and electrons separately with a low chance of recombination⁷⁵. The charge collection efficiency is high if charge collection is significantly quicker than charge recombination because the electrons are captured before they have a chance to recombine⁷⁷.

Figure 30 shows the exciton dissociation probability and charge collection efficiency of the binary devices at room temperature (A), 50°C (B) and 100°C (C) for 1020 minutes and a summary of the results (D).

The devices, whether untreated or thermally aged at 50 and 100°C for 1020 minutes, show no significant difference in exciton dissociation probability, the results of the triple determination ranging from 98 ± 1 to $97 \pm 1\%$. The averaged values are all within the standard deviation

range, so no significant change of the exciton dissociation probability due to thermal aging can be observed.

The charge collection efficiency is different, here the untreated devices and those aged at 50°C for 1020 minutes are very similar, with a value of 92 ± 1 and $91 \pm 1\%$ respectively. However, the charge collection efficiency deteriorates to a value of $82 \pm 1\%$ when thermally aged at 100°C for 1020 minutes, and these layers thus show poorer charge transport and increased recombination.

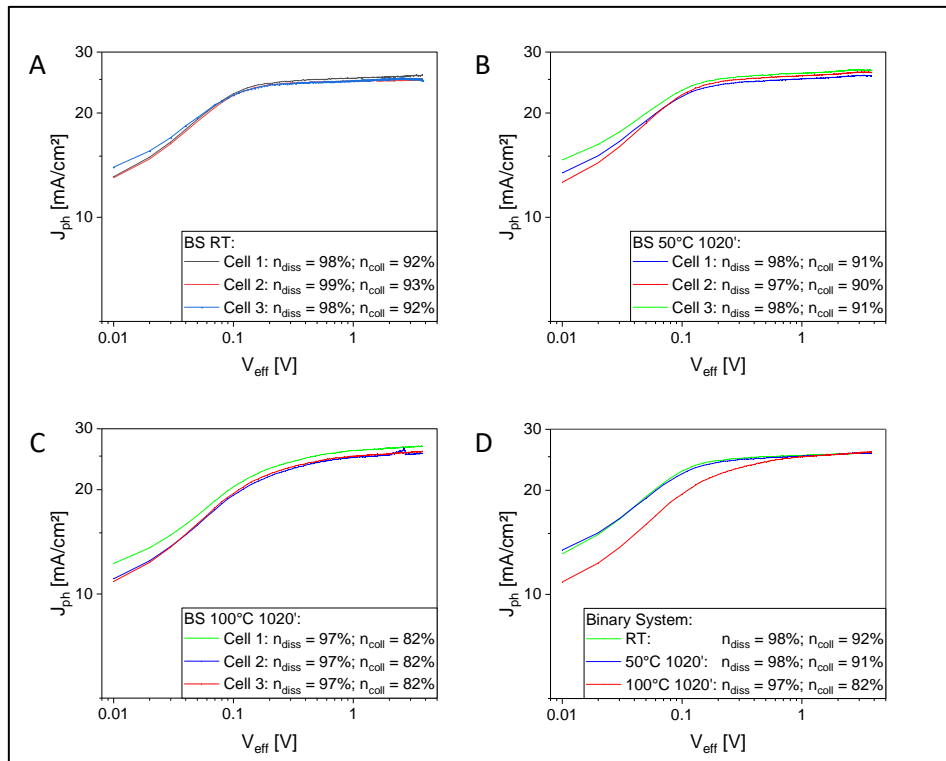


Figure 30: Exciton Dissociation Probability and Charge Collection Efficiency of the binary devices at room temperature (A), 50°C (B) and 100°C (C) for 1020 minutes and a summary of the results (D).

Figure 31 shows the exciton dissociation probability and Charge Collection Efficiency of the ternary devices at room temperature (A), 50°C (B) and 100°C (C) for 1020 minutes and a summary of the results (D). Also, the ternary devices show a very high and similar exciton dissociation probability for the untreated devices and those thermally aged at 50 and 100°C for 1020 minutes. The values of the triple determination are 97 ± 1 and $98 \pm 1\%$, respectively, and are thus all within the range of the standard deviation, so there is no significant difference in the exciton dissociation probability.

As with the binary devices, the ternary devices show a significant difference in charge collection efficiency, which is, however, somewhat smaller than with the binary devices. The

values of the untreated devices and those that were thermally aged at 50°C for 1020 minutes have similar values, which averaged over the three measurements are $91 \pm 1\%$. However, the charge collection efficiency drops significantly for the devices thermally aged at 100°C for 1020 minutes to a value of $87 \pm 1\%$, compared with the binary devices, the deterioration is not as strong, which drop to $82 \pm 1\%$. The difference between binary and ternary devices was also evident in the performance, where the binary devices deteriorate by 13.8% in relative efficiency after thermal aging, while the ternary devices loose only 8.3% in relative efficiency.

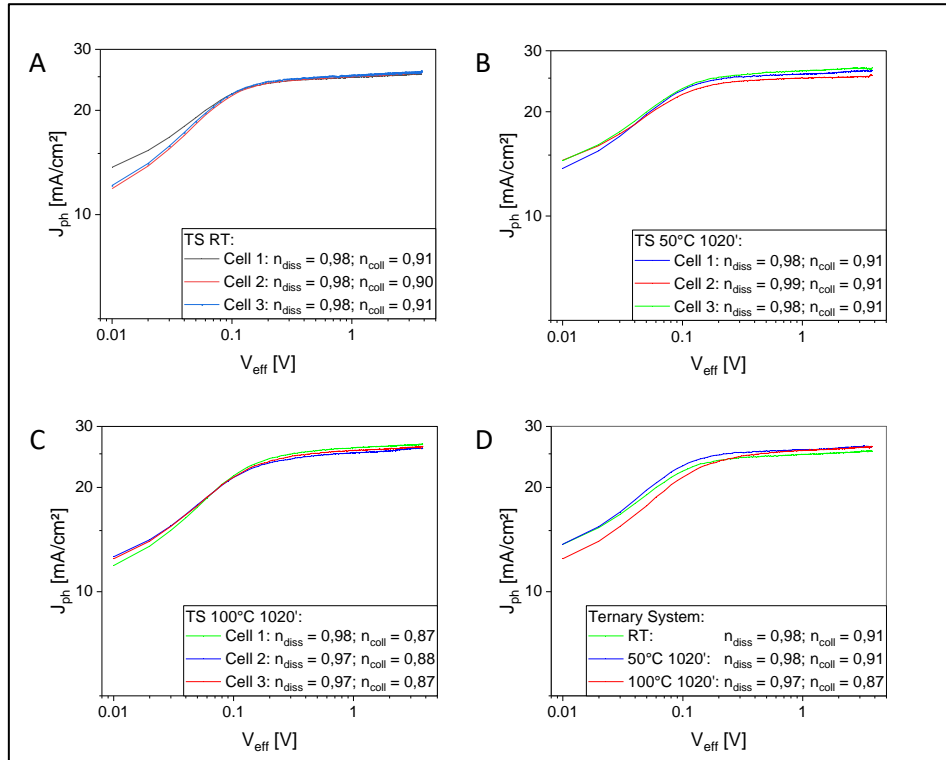


Figure 31: Exciton Dissociation Probability and Charge Collection Efficiency of the ternary devices at room temperature (A), 50°C (B) and 100°C (C) for 1020 minutes and a summary of the results (D).

3.6.6 Atomic force microscopy

The atomic force microscopy (AFM) surface images of the binary devices at room temperature (A) and after 1020 minutes of temperature treatment at 50°C (B) and 100°C (C) as well as the corresponding phase images (D, E, F), shown in Figure 32. The roughness of the layers is generally very low, ranging from 1.20 to 1.45 nm.

While in the topography images, no distinct changes in the absorber layer morphology are observed based on the temperature exposures, the phase images indicate higher and more prominent phase contrast in the sample annealed at 100°C for 1020 minutes. This gives the hint that the Y6 phase does not only get more crystalline, as expected due to the red-shift of the absorption spectra, but the phases also seem to become purer, at least at the surface of the films which is accessible by the AFM measurements.

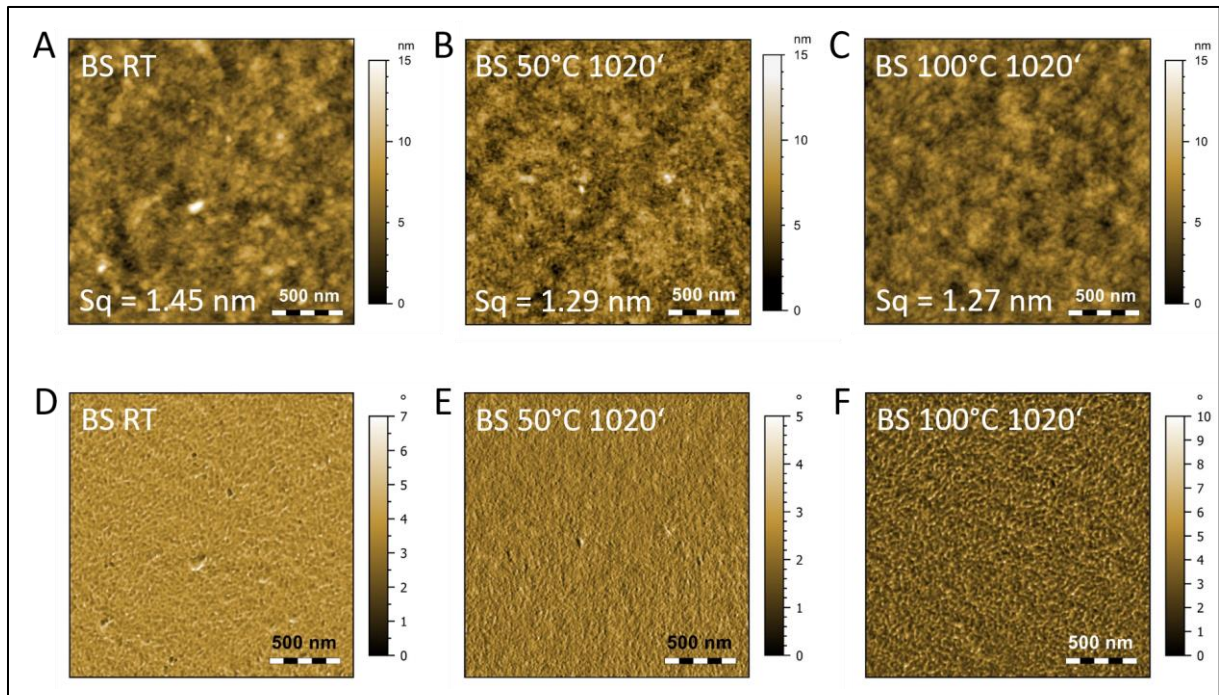


Figure 32: AFM surface images of the binary devices at room temperature (A) and after 1020 minutes temperature treatment at 50°C (B) and 100°C (C) and the corresponding phase images (D, E, F); measured by Elena Zuccala.

In Figure 33, the AFM topography images of the ternary PM6/Y6/PC₇₁BM devices at room temperature (A), after 1020 minutes temperature treatment at 50°C (B) and 100°C (C) as well as the corresponding phase images (D, E, F), are presented. Also in these films, very low roughness values are observed, ranging from 1.12 to 1.31 nm and no prominent changes in the surface morphology are found.

Similar to the binary PM6/Y6 devices, the phase images show the trend of a more defined phase separation after the temperature treatment at 100°C.

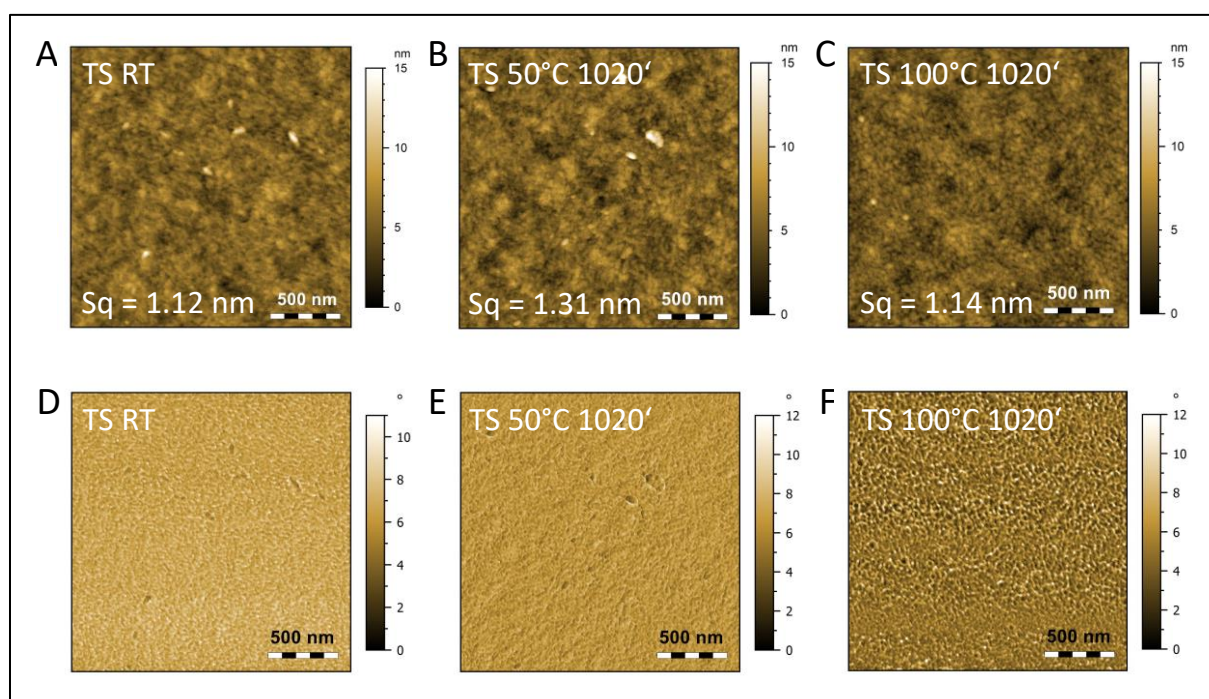


Figure 33: AFM surface images of the ternary devices at room temperature (A) and after 1020 minutes temperature treatment at 50°C (B) and 100°C (C) and the corresponding phase images (D, E, F); measured by Elena Zuccala.

3.6.7 TEM investigations

To reveal more detailed information about the donor-acceptor phase separation, the binary PM6/Y6 blends have been investigated in collaboration with Tatiana Kormilina, Georg Haberfehlner and Gerald Kothleitner at the Institute of Electron Microscopy and Nanoanalysis. For this analysis, scanning transmission electron microscopy (STEM) high-angle annular dark-field (HAADF) images and electron energy loss spectroscopy (EELS) based elemental mapping was used, which resulted in a good contrast between the donor and the acceptor despite very low differences in the chemical composition.^{78,79} This technique makes use of the fact that Y6 contains N and S atoms, while PM6 does not contain N atoms.

Thus, the red areas in the elemental distribution images in Figure 34 represent the Y6 phase, while the green areas represent the PM6 phase. This is corroborated by the nitrogen and sulfur-distribution images in Figure 35. In the sulfur images, areas which contain high concentrations of nitrogen are lighter.

In the TEM images, the Y6 domains in the absorber layers appear to be approx. 15-20 nm in size, while the PM6 domains are slightly larger (typically around 30 nm, but also larger domains are observed). Based on the temperature treatments at 50°C and 100°C, no significant changes in the sizes of the Y6 and the PM6 phase are observed. Regarding the phase purity, these investigations, do not allow clear conclusions, as thickness of the specimens was between 70 and 100 nm and thus contrast in the TEM characterization can also stem from different PM6 or Y6 domains in different depths of the specimen.

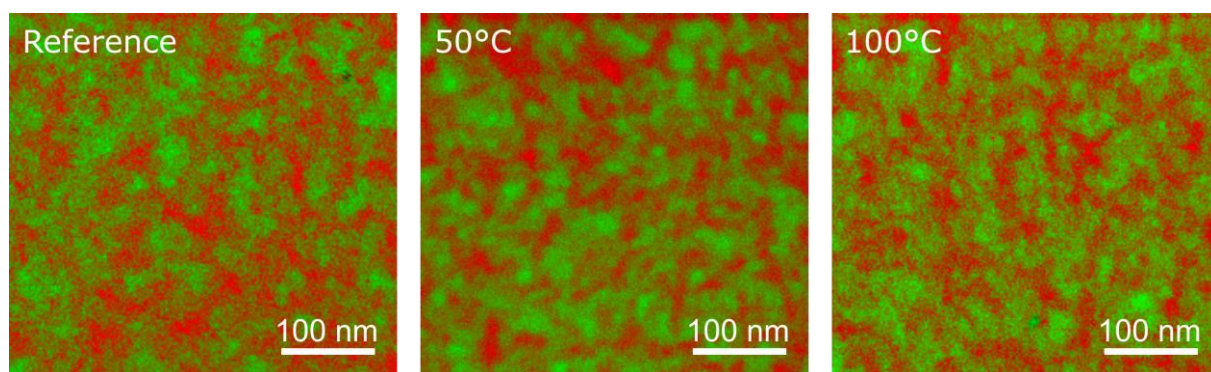


Figure 34: STEM HAADF elemental distribution images based on EELS elemental mapping showing an overlay of nitrogen (red, only present in Y6) and sulfur (green) distributions.

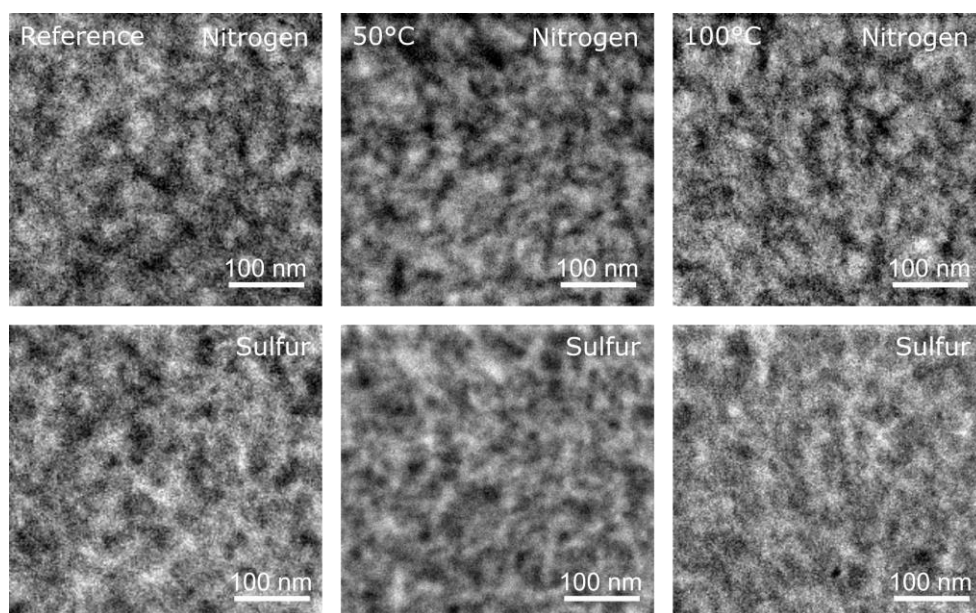


Figure 35: STEM HAADF elemental distribution images based on EELS elemental mapping; first row: nitrogen distribution; second row: sulfur distribution.

3.6.8 GIWAXS and GISAXS investigations

Grazing incidence wide and small angle X-ray scattering (GIWAXS and GISAXS) measurements were performed at the SAXS beamline at Elettra Trieste (by Thomas Rath, Bettina Schlemmer, Elena Zuccala, Peter Fürk and Heinz Amenitsch) to obtain further knowledge about the changes of the crystallinity of the PM6/Y6 films based on the temperature treatment. The GIWAXS images in Figure 36 reveal a typical pattern of PM6/Y6 absorber layers with a face-on orientation of PM6 and Y6 with respect to the substrate. The strong π - π stacking peak observed at around 18 nm^{-1} in out-of-plane direction stems from contributions of PM6 and Y6. The scattering feature at approx. 3 nm^{-1} in in-plane direction stems from lamellar stacking in the absorber layer.

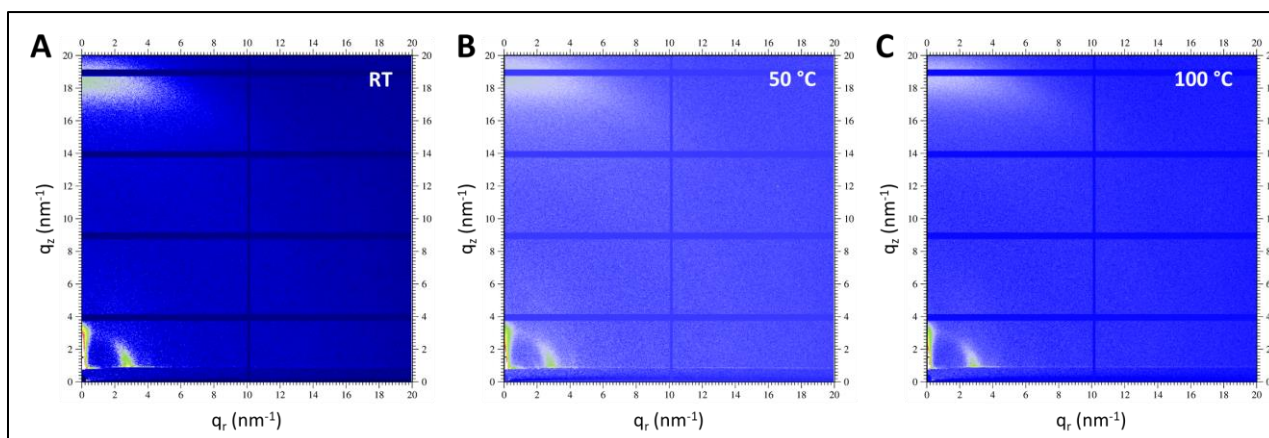


Figure 36: GIWAXS images of the binary PM6/Y6 thin films on silicon substrates (A: room temperature, B: after annealing at 50 °C for 1020 minutes; C: after annealing at 100 °C for 1020 minutes).

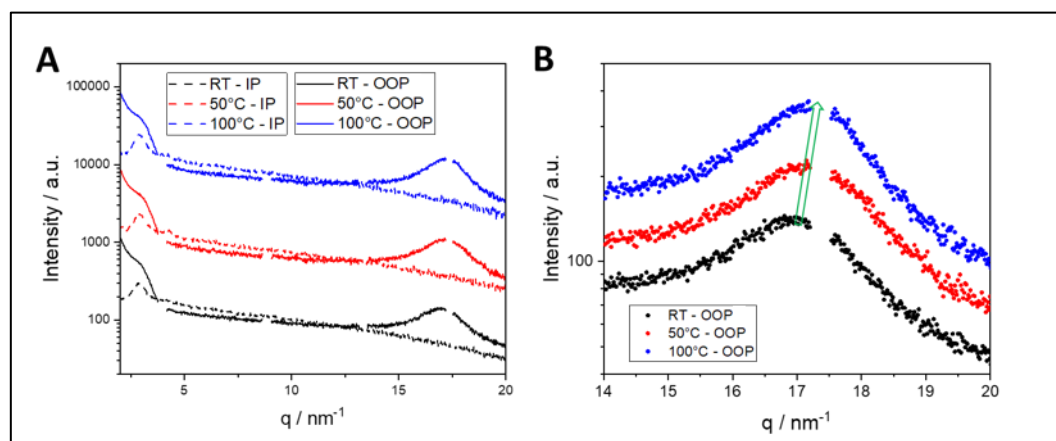


Figure 37: (A) In-plane and out-of-plane line cuts of the GIWAXS patterns and (B) q -region of the π - π stacking peak in out-of-plane direction.

The π - π stacking peak in the 100 °C sample is sifted to higher q -values, indicating a denser π - π stacking in the film. Based on the fact that the Y6 film shows a pronounced redshift in the absorption spectrum after the 100 °C temperature treatment, while the PM6 absorption

maximum does not shift, we expect, that the denser stacking occurs mainly in the Y6 phase. Upon the temperature treatment, the maximum of this peak shifts from 17.0 to 17.3 nm⁻¹, which corresponds to a reduction of the π - π stacking distance from 0.369 to 0.363 nm, Figure 37.

Moreover, GISAXS measurements were performed on these films. The obtained GISAXS images are presented in Figure 38 and the corresponding in-plane cuts are shown in Figure 39. The sizes of the Y6 domains of 15-20 nm obtained from the TEM investigations, correspond to a q-range of 0.3-0.4 nm⁻¹ in the GISAXS data. Around this q-range an increase in intensity is observed in particular for the sample annealed for 1020 minutes at 100°C. This indicates a more defined phase separation between PM6 and the Y6 phase as it was observed already in the AFM phase images. Moreover, the GISAXS data do not reveal a significant change of the domain sizes, which is also supported by the TEM elemental distribution images.

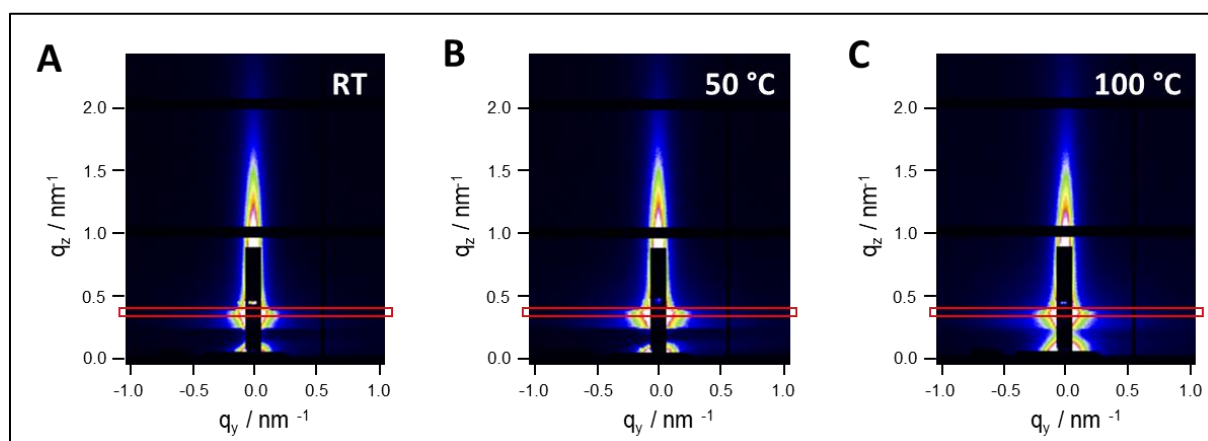


Figure 38: GISAXS images of the binary PM6/Y6 thin films on silicon substrates (A: room temperature, B: after annealing at 50°C for 1020 minutes; C: after annealing at 100°C for 1020 minutes). The red box indicates the area for integration in in-plane direction.

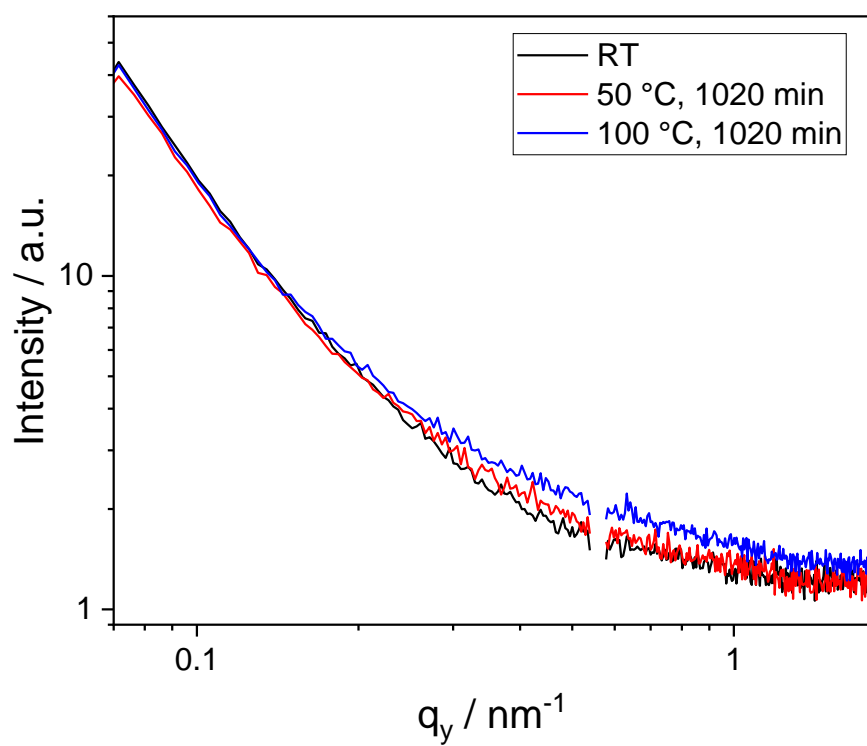


Figure 39: In-plane integration of the GISAXS patterns shown in Figure 38.

3.7 Long-term stability

In order to get a better insight into the long-term stability of PM6/Y6 based solar cells, three different experiments were selected. The first was the shelf life test (ISOS-D-1), in which the devices were stored in the dark, at room temperature and under nitrogen atmosphere in the glove box. The second type was storage at high temperatures, ISOS-D-2, in this case 65°C, also in the dark under nitrogen atmosphere in the glovebox. The third type of stress was thermal cycling, ISOS-LT-1, in which the devices were repeatedly heated from room temperature to 65°C and then cooled back to room temperature. Likewise, in the dark and under nitrogen atmosphere in the glovebox.

3.7.1 ISOS-D-1 shelf life

All the devices used had an efficiency of over 15% before the start. The binary devices were stored and regularly measured for about 5500 hours and the ternary devices for 6000 hours. For the evaluation of this experiment, a mean value was calculated from 10 devices. The results are shown graphically in relative terms in Figure 40.

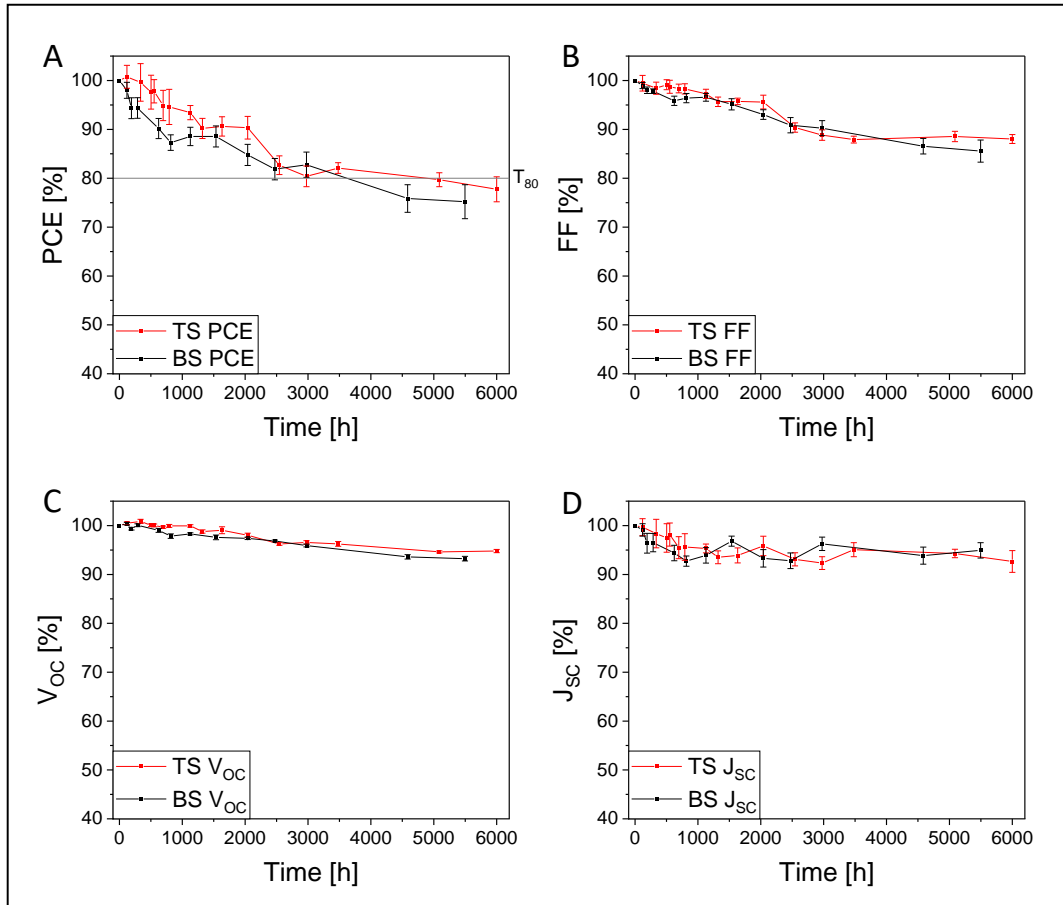


Figure 40: Results of the shelf life experiment, change of the PCE (A), FF (B), V_{OC} (C) and J_{SC} (D) over time; average of 10 devices.

Figure 40A shows the change in PCE, B illustrates the fill factor, C represents V_{OC} , and D shows the J_{SC} over time. No significant difference can be found between the binary and ternary systems.

The absolute data can be found in Table 9 for the binary system and Table 10 for the ternary system. The two systems follow the same trend and no significant difference was found between the binary and ternary systems.

Table 9: Results of the shelf life experiment, binary system; average of 10 devices.

Binary System								
t [h]	AV _{VOC} [mV]	SD _{VOC}	AV _{ISC} [mA/cm ²]	SD _{ISC}	AV _{FF} [%]	SD _{FF}	AV _{PCE} [%]	SD _{PCE}
0	814	3	26.5	0.3	73.8	0.4	15.9	0.2
120	817	2	26.2	0.3	73.0	0.5	15.6	0.3
192	809	2	25.5	0.5	72.3	0.5	15.0	0.3
288	815	2	25.6	0.5	72.2	0.3	15.0	0.3
624	806	3	25.0	0.4	70.7	0.7	14.3	0.3
816	797	4	24.6	0.3	71.1	0.7	13.9	0.2
1128	800	2	24.9	0.4	71.2	0.6	14.1	0.3
1536	795	4	25.6	0.3	70.2	0.8	14.1	0.3
2040	793	2	24.7	0.4	68.6	0.7	13.5	0.3
2472	789	1	24.6	0.4	67.0	1.0	13.0	0.3
2976	781	2	25.5	0.4	66.6	1.0	13.2	0.3
4584	762	3	24.9	0.4	63.8	1.0	12.1	0.3
5496	759	4	25.1	0.4	63.1	1.4	12.0	0.4

The devices of the binary system started with an efficiency of $15.9 \pm 0.2\%$, which dropped to $12.0 \pm 0.4\%$ after 5496 hours. In the same period, the V_{OC} fell from 814 ± 3 to 759 ± 4 mV, the J_{SC} barely dropped from 26.5 ± 0.3 to 25.1 ± 0.4 mA/cm², and the FF suffered the biggest loss in real terms, from 73.8 ± 0.4 to $63.1 \pm 1.4\%$.

In the case of ternary devices, Table 10, the losses are similar over time. These were measured regularly over 6000 hours. The efficiency dropped from 15.6 to 12.2%, the V_{OC} changed from 819 ± 3 to 777 ± 3 mV, the J_{SC} dropped from 25.7 ± 0.4 to 23.8 ± 0.5 mA/cm² and the FF decreased from 75.2 ± 0.9 to $66.2 \pm 0.6\%$.

Table 10: Results of the shelf life experiment, ternary system; average of 10 devices.

Ternary System								
t [h]	AV_{VOC} [mV]	SD_{VOC}	AV_{ISC} [mA/cm²]	SD_{ISC}	AV_{FF} [%]	SD_{FF}	AV_{PCE} [%]	SD_{PCE}
0	819	3	25.7	0.4	75.2	0.9	15.6	0.4
120	823	2	25.7	0.4	74.8	1.2	15.8	0.4
336	826	4	25.3	0.7	74.1	0.9	15.6	0.6
504	820	2	25.1	0.7	74.6	0.8	15.3	0.5
552	820	2	25.3	0.6	74.3	1.0	15.3	0.4
696	817	2	24.6	0.6	74.0	0.7	14.8	0.5
792	819	3	24.6	0.7	73.9	0.8	14.8	0.5
1128	819	2	24.5	0.2	73.2	0.7	14.6	0.2
1320	809	3	24.1	0.3	72.0	0.7	14.1	0.3
1632	811	6	24.2	0.4	72.0	0.5	14.2	0.3
2040	803	3	24.7	0.5	71.9	1.0	14.1	0.3
2544	788	2	24.0	0.3	68.0	0.6	12.9	0.2
2976	791	3	23.8	0.3	66.8	0.7	12.6	0.3
3480	789	4	24.5	0.4	66.1	0.5	12.8	0.1
5088	775	2	24.3	0.2	66.6	0.7	12.5	0.2
6000	777	3	23.8	0.5	66.2	0.6	12.2	0.3

The current-voltage characteristics of the two systems are shown in Figure 41, where the binary system is shown in 41A and C. In Figure C, the zoom has been increased to better see the change in the shape of the curve. The characteristic curves of the ternary system are shown in Figure 41B and D, also without and with zoom.

For the binary devices, a curve was plotted from the beginning of the experiment, one after 288, 1536, 2472, 4584, and the last one after 5496 hours.

In the case of the ternary device, a curve was obtained at 0, 552, 1128, 2544, 3480, 5088 and 6000 hours.

It can be seen very clearly that the curves, regardless of whether they are binary or ternary systems, become (at voltages higher than the V_{OC}) flatter and flatter with time, and the fill factor is reduced as a result; the change is not so great for the current density and voltage. The significant change in the shape of the curve is an indication of an increase in the series resistance. The parallel resistance probably changes only very slightly since the slope in the blocking direction remains quite stable.

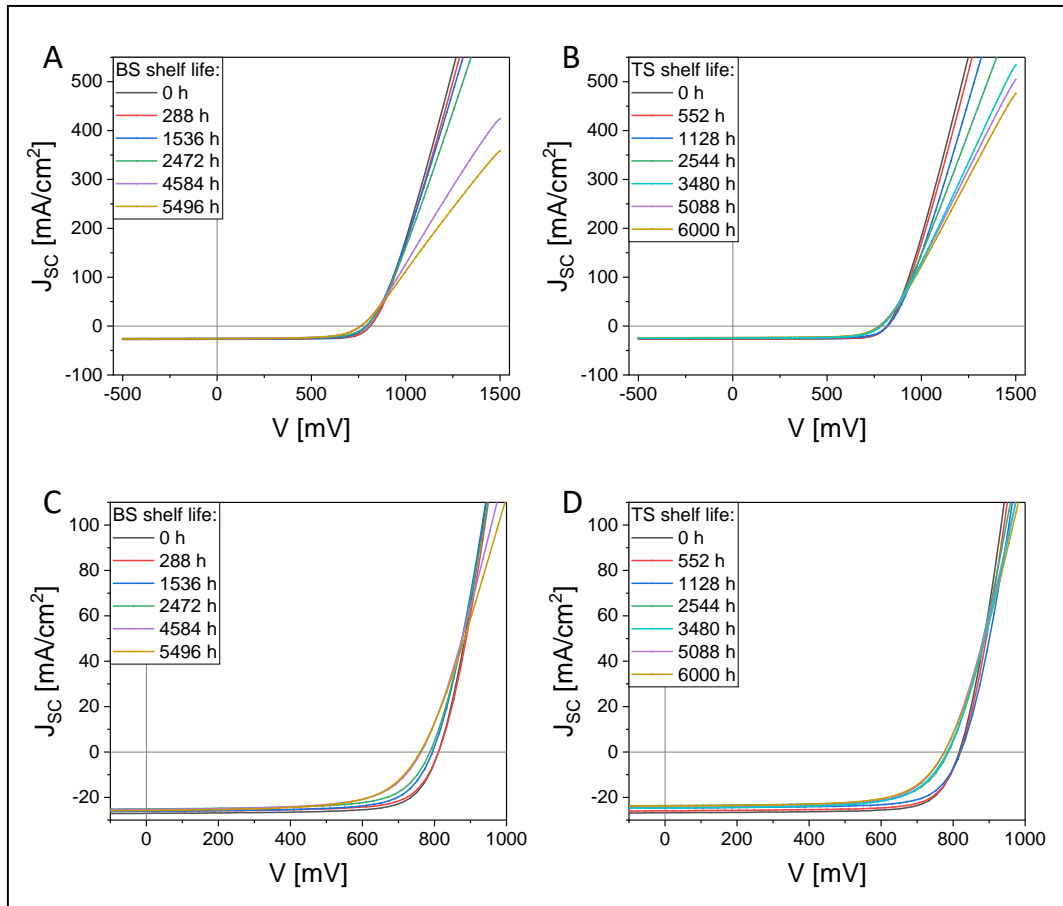


Figure 41: Current density voltage characteristics of the shelf-life experiment, binary and ternary devices (A, B) and the same devices with zoom (C, D) over time.

3.7.2 ISOS-D-2 high storage temperature

For the results of this experiment, an average value was calculated from three devices. As before, only devices with an efficiency of over 15% were used. The storage temperature was 65°C, in the dark and under nitrogen atmosphere in the glovebox. The devices were exposed to 65°C for 1080 hours and measured regularly.

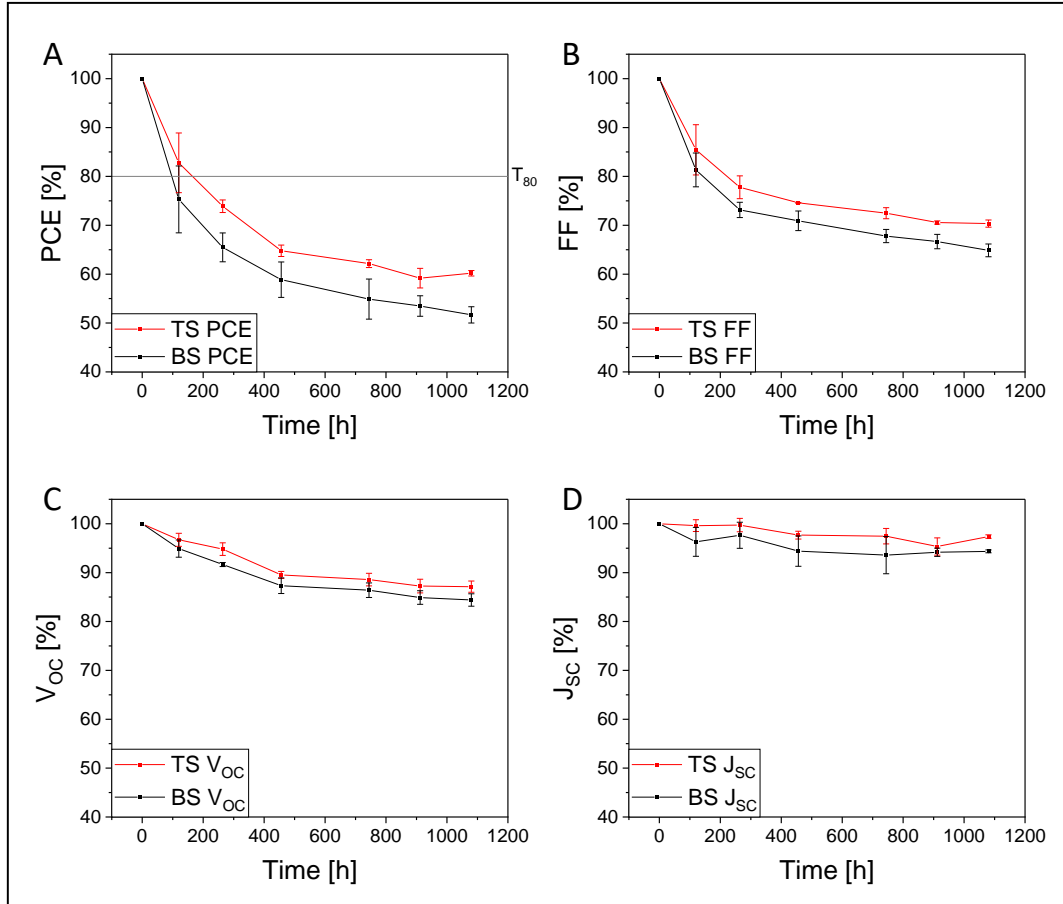


Figure 42: Results of the 65°C storage temperature experiment, change of the PCE (A), FF (B), V_{OC} (C) and J_{sc} (D) over time; average of 3 devices.

As can be seen in Figure 42, the PCE of the binary system drops by almost $48.3 \pm 1.7\%$, but the PCE of the ternary system deteriorates by $38.8 \pm 0.6\%$ in the same 1080 hours (A). The fill factor (B) of the binary system deteriorates by $35.1 \pm 1.4\%$ and that of the ternary system by $29.7 \pm 0.8\%$. Comparing the change in V_{OC} (C), it is not as high as for the fill factor and the PCE. The binary system loses relatively $15.6 \pm 1.3\%$ and the ternary system $12.9 \pm 1.2\%$. The current density (D) remains fairly constant over time for both systems, with the binary system losing $5.7 \pm 0.3\%$ and the ternary losing only $2.6 \pm 0.4\%$.

Also, as in the shelf life experiment, both systems follow the same trend, but the losses at the beginning are more pronounced in the binary system. The PCE and the fill factor decrease very

fast within the first 300 hours and slow down their change significantly afterwards. In contrast, the V_{OC} decreases quite linearly and hardly any significant change can be seen in the J_{SC} . In the following Table 11, the absolute results of this experiment are presented for the binary and ternary devices.

The almost identical PCE of the two systems provides a very good comparability of this experiment. The absolute mean value of the binary devices is $15.3 \pm 0.2\%$ and that of the ternary devices is $15.2 \pm 0.2\%$. After the 1080-hour temperature treatment at 65°C , the binary devices have a PCE of only $7.9 \pm 0.2\%$, while the ternary devices have a PCE of $9.1 \pm 0.2\%$.

The deterioration of the V_{OC} is very similar for both systems and does not have a high significance. For the binary devices, the V_{OC} decreases from 800 ± 5 to 675 ± 14 mV and for the ternary from 803 ± 3 to 699 ± 7 mV.

Similarly, the J_{SC} does not show much difference between the two systems. The binary devices start with a J_{SC} of 25.8 ± 0.3 and end up at 24.3 ± 0.3 mA/cm² after 65°C for 1080 hours, while the ternary devices start with 25.4 ± 0.2 and still have 24.8 ± 0.1 mA/cm² at the end of the test, thus performing a little better.

The fill factor deteriorates significantly with both systems, although the deterioration is slightly higher for the binary system. The fill factor for the binary devices is reduced from 74.4 ± 0.9 to $48.3 \pm 0.6\%$ and for the ternary devices from 74.8 ± 1.3 to $52.6 \pm 0.7\%$.

Table 11: Results of the high storage temperature experiment; average of 3 devices.

Binary System								
t [h]	AV_{VOC} [mV]	SD_{VOC}	AV_{ISC} [mA/cm²]	SD_{ISC}	AV_{FF} [%]	SD_{FF}	AV_{PCE} [%]	SD_{PCE}
0	800	5	25.8	0.3	74.4	0.9	15.3	0.2
120	759	10	24.8	1.0	60.5	3.2	11.5	1.2
264	733	7	25.2	0.4	54.4	0.6	10.0	0.3
456	698	17	24.3	0.5	52.8	1.2	9.0	0.5
744	691	16	24.1	0.7	50.4	0.4	8.4	0.5
912	679	15	24.3	0.1	49.6	0.7	8.2	0.2
1080	675	14	24.3	0.3	48.3	0.6	7.9	0.2
Ternary System								
t [h]	AV_{VOC} [mV]	SD_{VOC}	AV_{ISC} [mA/cm²]	SD_{ISC}	AV_{FF} [%]	SD_{FF}	AV_{PCE} [%]	SD_{PCE}
0	803	3	25.4	0.2	74.8	1.3	15.2	0.2
120	776	13	25.3	0.3	63.9	2.7	12.5	0.8
264	761	12	25.4	0.4	58.2	0.7	11.2	0.1
456	719	4	24.8	0.2	55.8	1.0	9.8	0.2
744	711	8	24.8	0.3	54.2	0.3	9.4	0.1
912	700	9	24.3	0.5	52.8	0.8	9.0	0.4
1080	699	7	24.8	0.1	52.6	0.7	9.1	0.2

The current density voltage characteristics of the two systems for the high storage temperature experiment are shown in Figure 43, where the binary system is shown in 43A and C. In Figure C, the zoom has been increased to better see the change in the shape of the curve. The characteristic curve of the ternary system is shown in Figure 43B and D, also without and with zoom.

Curves were plotted after 0, 120, 264, 456, 744, 912, and 1080 hours, for both systems. In general, it can be seen that with the continuation of the experiment the series resistance increases in both systems, but initially not so fast in the ternary system, which also leads to the greater initial degradation of the binary devices. In both systems, a rather strong “s-shaped” curve is formed with the duration of the experiment, which strongly worsens the fill factor.

In both systems, it can be seen that the curves at 0 and 120 hours of temperature treatment, black and red curve, still show no significant change in the shape of the curve, but the curve at 264 hours differs significantly. While the blue curve, at 264 hours, in the binary system flattens out clearly in comparison to the black and red curves, this does not happen so markedly in the ternary system after 264 hours.

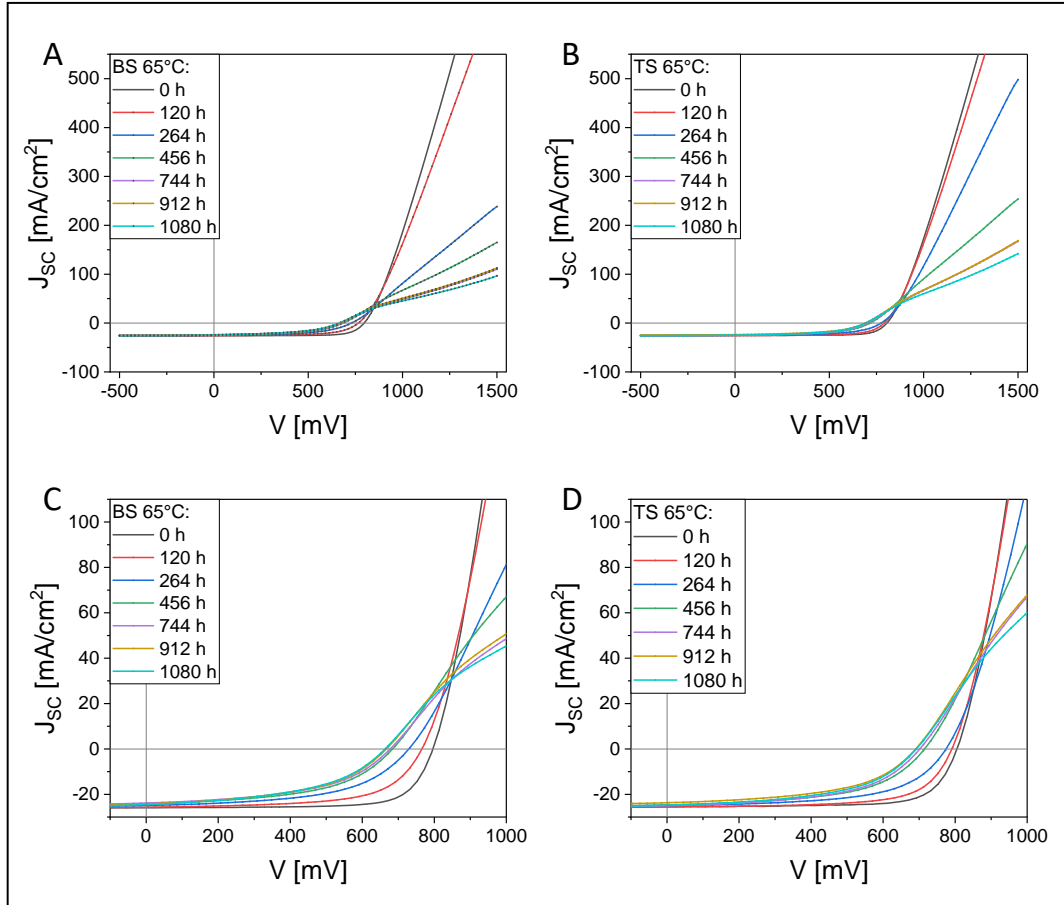


Figure 43: Current density voltage characteristics of the high storage temperature experiment, binary and ternary devices (A, B) and the same devices with zoom (C, D) over time.

3.7.3 ISOS-LT-1 solar thermal cycling (cycle RT – 65°C)

For the thermal cycling experiment, only devices with a PCE above 15% were used. Each cycle starts at 25°C and heats up to 65°C at a rate of one degree per minute, then the temperature of 65°C is maintained for 15 minutes. It then cools back down to 25°C at the same rate and is held at that temperature again for 15 minutes, after which the next cycle starts. The first 50 cycles were measured in steps of 10 and then the devices were measured every 50 cycles until a total of 200 cycles was reached. For the evaluation of this experiment, a mean value was calculated from 3 devices. Figure 44 shows the relative evaluation of this experiment. The two systems follow the same trend as in the previous tests, but the deterioration of the ternary system is not as great as in the binary system. At the beginning, in the first 50 cycles, the deterioration is stronger for both systems and decreases thereafter. The results of this experiment are also very comparable since the mean value of the PCE is the same for the binary and ternary devices, $15.1 \pm 0.2\%$ and $15.1 \pm 0.1\%$.

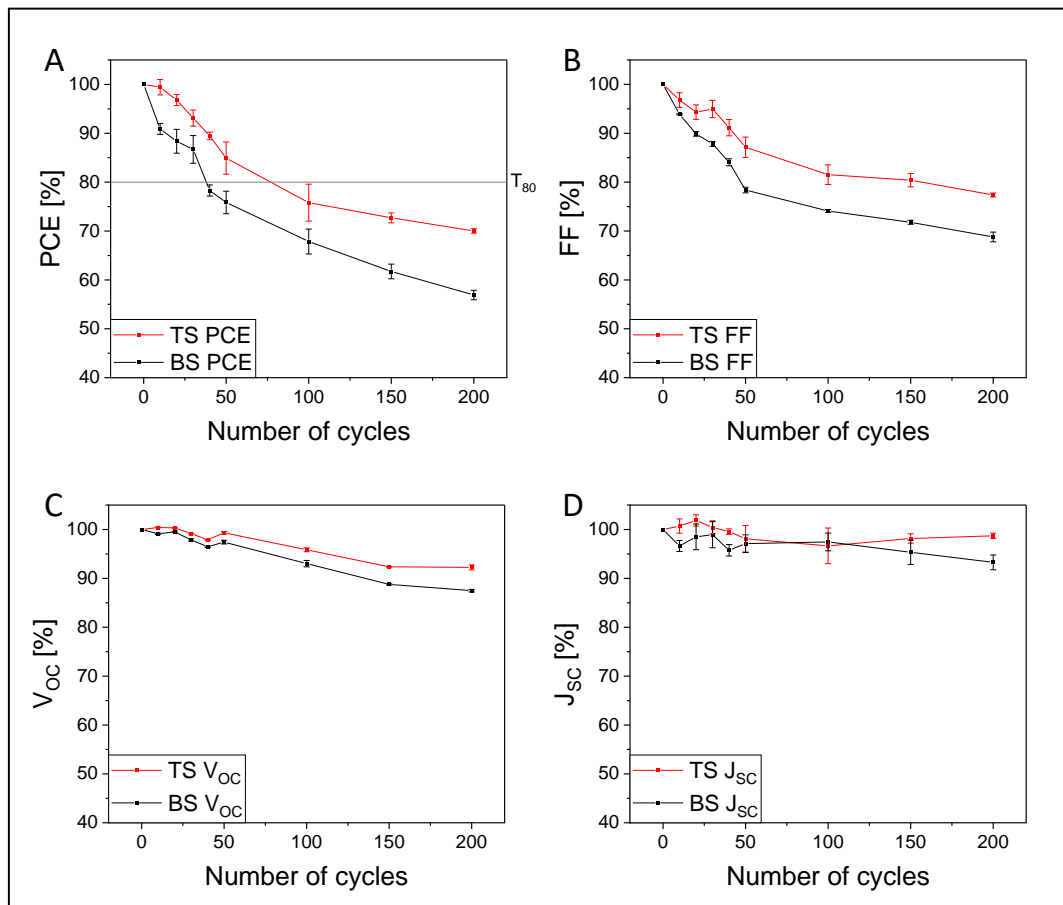


Figure 44: Results of the thermal cycling experiment, change of the PCE (A), FF (B), V_{oc} (C) and J_{sc} (D) over the cycles; average of 3 devices.

The largest difference in the results of the temperature cycling experiment between the two systems is seen in the PCE, after 200 cycles, whereby the binary devices drop $43.1 \pm 1.0\%$ in relative terms and the ternary devices drop $30.0 \pm 0.5\%$, in contrast.

The fill factor follows the same trend as the PCE, only a little weaker. The fill factor of the binary devices decreases by $31.2 \pm 1.0\%$ and the ternary devices lose $32.6 \pm 0.4\%$, after 200 cycles. Both fill factor and PCE deteriorate more rapidly within the first 50 cycles, and thereafter the deterioration becomes slower.

The V_{OC} of the two systems barely drops for the first 50 cycles, then for 100 cycles it drops a little, and in the last 50 cycles there is hardly any deterioration. The binary devices lose $12.5 \pm 0.3\%$ of V_{OC} within the 200 cycles and the ternary devices lose $7.8 \pm 0.5\%$.

In the case of the J_{SC} , the loss is the smallest, but longer cyclizations must be carried out in order to be able to make more accurate statements about the development. After 200 cycles, the J_{SC} of the binary devices drops by 6.7 ± 1.6 in relative terms and by only $1.3 \pm 0.6\%$ for the ternary devices.

As can be seen in the Table 12 below, the absolute data of the temperature cycling experiment, the PCE of the binary devices decreases from 15.1 ± 0.2 to $8.6 \pm 0.1\%$ more than that of the ternary devices, where only a decrease from 15.1 ± 0.1 to $10.6 \pm 0.1\%$ is observed after the 200 cycles.

The fill factor decreases in absolute terms from 74.6 ± 0.5 to $51.3 \pm 0.5\%$ for the binary devices and from 74.0 ± 0.7 to $57.2 \pm 0.5\%$ for the ternary devices.

The binary devices lose 100 mV over the 200 cycles, dropping from 802 ± 1 to 702 ± 2 mV. The ternary devices drop by 63 mV from 804 ± 2 to 741 ± 2 mV.

The J_{SC} drops by 1.7 mA/cm^2 in absolute terms for binary devices, from 25.6 ± 0.3 to $23.9 \pm 0.1 \text{ mA/cm}^2$, in comparison, the J_{SC} barely drops for ternary devices, from 25.4 ± 0.1 to $25.1 \pm 0.2 \text{ mA/cm}^2$.

The standard deviations are generally very small for all experiments, making the data easily comparable.

Table 12: Results of the thermal cycling experiment; average of 3 devices.

Binary System								
Cycles	AV _{VOC} [mV]	SD _{VOC}	AV _{ISC} [mA/cm ²]	SD _{ISC}	AV _{FF} [%]	SD _{FF}	AV _{PCE} [%]	SD _{PCE}
0	802	1	25.6	0.3	74.6	0.5	15.1	0.2
10	795	2	24.7	0.1	70.0	0.4	13.7	0.1
20	798	1	25.2	0.8	67.0	0.6	13.3	0.3
30	785	2	25.3	0.5	65.5	0.6	13.1	0.3
40	774	1	24.5	0.6	62.7	0.5	11.8	0.2
50	782	3	24.9	0.4	58.4	0.3	11.4	0.2
100	746	6	25.0	0.2	55.3	0.5	10.2	0.3
150	712	1	24.4	0.9	53.5	0.5	9.3	0.3
200	702	2	23.9	0.1	51.3	0.5	8.6	0.1
Ternary System								
Cycles	AV _{VOC} [mV]	SD _{VOC}	AV _{ISC} [mA/cm ²]	SD _{ISC}	AV _{FF} [%]	SD _{FF}	AV _{PCE} [%]	SD _{PCE}
0	804	2	25.4	0.1	74.0	0.7	15.1	0.1
10	807	2	25.6	0.4	71.6	0.5	15.0	0.3
20	806	3	25.9	0.3	69.7	0.5	14.6	0.2
30	797	2	25.5	0.4	70.2	0.7	14.0	0.3
40	787	2	25.3	0.2	67.4	0.6	13.5	0.2
50	798	4	24.9	0.7	64.4	1.1	12.8	0.6
100	770	5	24.6	0.9	60.3	1.1	11.4	0.6
150	742	3	25.0	0.2	59.5	0.5	11.0	0.2
200	741	2	25.1	0.2	57.2	0.5	10.6	0.1

Figure 45 shows the current density voltage curves of all measurements performed after 0, 10, 20, 30, 40, 50, 100 and 200 cycles. Figures 45A and B show the complete curves of a binary and ternary device and Figure 45C and D show the same curves with zoom to better see the evolution of the shape or the curves.

As in the previous experiments, it is easy to see that the series resistance of the binary devices increases more than that of the ternary devices. In picture C it can be seen well that the V_{OC} changes more with the binary devices than in picture D with the ternary devices. Also related to the fill factor, the zoomed images show that the curves shift more to the left and flatten out more with the binary devices compared to the ternary devices. The parallel resistance does not change or hardly changes, which can be well seen in the slope of the curves around 0 V, which does not change noticeably.

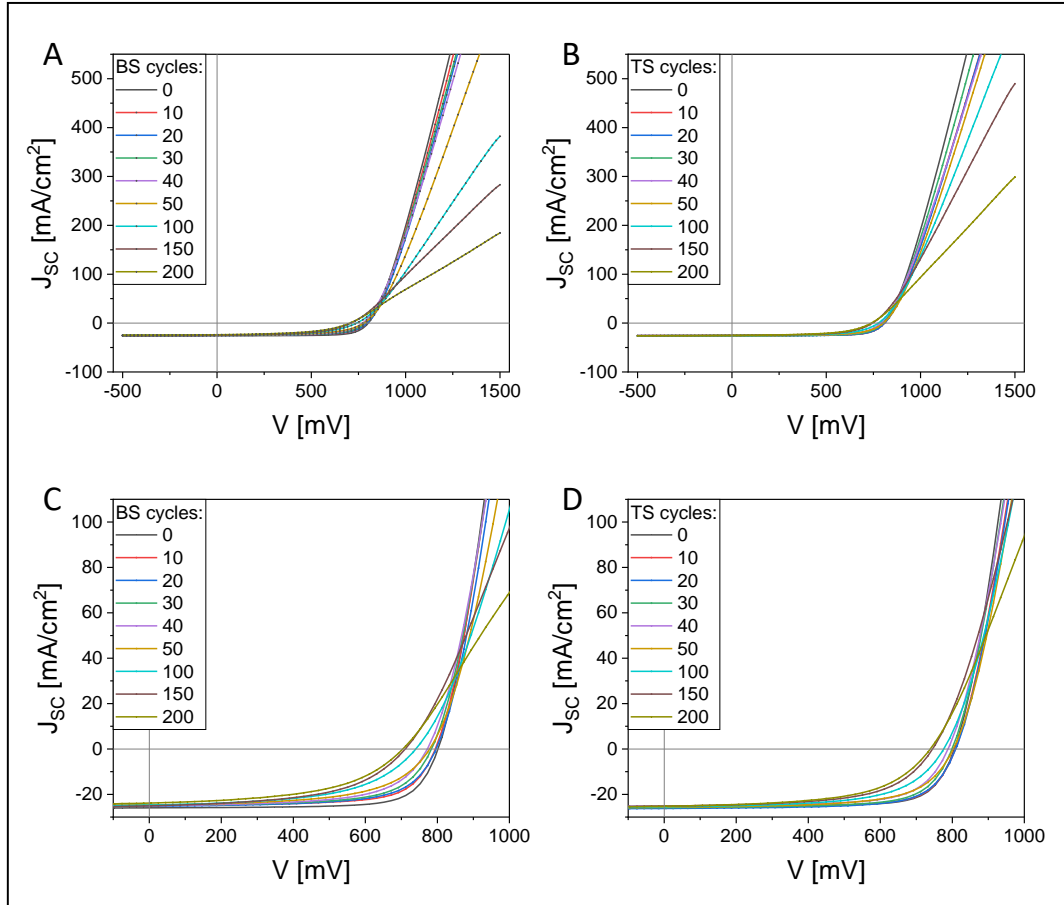


Figure 45: Current density voltage characteristics of the temperature cycling experiment, binary and ternary devices (A, B) and the same devices with zoom (C, D) over time.

4 Conclusions

In this work, state-of-the-art OSCs with a PCE of more than 15% could be produced with a high reproducibility. The champion device attained a PCE value of 17.0%, showing an open circuit voltage of 817 mV, a short circuit current density of 27.2 mA/cm² and a fill factor of 76%.

Long-term stability is currently one of the major hurdles of OSCs towards further adoption in many applications. Therefore, this work was devoted to the investigation of the temperature stability of OSCs. To investigate the temperature stability, three types of experiments were conducted. Short-term was the heating run of the active layer, for the medium-term, the devices were subjected to temperature treatment at 50 and 100°C for 1020 minutes, and in the long-term experiment, the devices were stored at room temperature and at 65°C in the glovebox and, in addition, devices were subjected to temperature cycling from room temperature to 65°C.

The short-term heat exposure of the active layer was done with a heating rate of 10°C/min from room temperature up to 200°C and then holding the 200°C for 20 minutes. It was observed that the solar cells show quite similar J_{SC} values when the absorber layer was treated up to 200°C. Generally, the J_{SC} values were around 25 ± 1 mA/cm² throughout the experiment, with a maximum of 26.2 mA/cm². The solar cells showed a very similar constant behavior in the PCE and FF values with absorber layers treated up to a temperature of 100°C, with a subsequent quite sharp drop of these values by treatments from 100 to 200°C, and with only a slight further degradation after the holding phase at 200°C. The initial value of the PCE for the non-annealed devices was 15.7 ± 0.3% and deteriorated to 10.3% ± 0.1 for the devices at the maximum temperature treatment. Similar, the FF values were reduced from 77 ± 0.3% to 64 ± 0.6%. The V_{OC} had its highest value in the non-annealed devices (836 ± 1 mV) and deteriorated fairly consistently to 657 ± 2 mV for the devices prepared at the end of the heating run. In this experiment, it was observed that the blend could withstand higher temperatures for a short time, but the optimum was at 100°C, yielding solar cells with a PCE of 16.1 ± 0.1%.

The devices prepared at room temperature and the ones prepared from blends having a temperature treatment until 100°C, 160°C, 200°C, and additionally 20 minutes at 200°C, were examined in greater detail by external quantum efficiency spectra, the investigation of the charge recombination properties, the exciton dissociation probability, and charge collection efficiency in the devices in order to better understand the results of this experiment. A trend is seen in the EQE data that solar cells with blends exposed to higher temperatures exhibit a shift to higher wavelengths between approx. 820 to 950 nm due to a red shift of the Y6 absorption.

In case of the light intensity-dependent measurements it can be concluded that, probably in the area of the J_{SC} , no bimolecular recombination is present and the charge transport and charge collection work well, even in devices annealed at higher temperatures. In the V_{OC} area it is a mixture of bimolecular and trap-assisted recombination, but the trap-assisted recombination rises in devices prepared from blends with increasing temperature and then drops again in those prepared with prolonged exposure to 200°C. The exciton dissociation probability slightly decreases during this experiment from 98 ± 1 to $93 \pm 1\%$. A more pronounced effect is observed regarding the charge collection efficiency, which drops from $91 \pm 1\%$ for the sample without annealing and for the sample exposed to 100°C to $79 \pm 1\%$ for that which was on the hot plate for the full heating run. This indicates that the annealing at higher temperatures has more impact on the charge transport than on the exciton dissociation.

Interestingly, the annealing at temperatures up to 100°C has only a very minor effect on the properties of the solar cells. The photovoltage slightly decreases, while the short circuit current density slightly increases. The FF remains unchanged, which leads only to a minor change in the PCE. Also, recombination properties, exciton dissociation probability and charge collection efficiency do not change upon a short annealing within this temperature range.

To explore the temperature stability over an extended timeframe, solar cells were placed on a heating plate either at 50 or 100°C for 1020 minutes in both cases. Therefore, 20 binary PM6/Y6 and 20 ternary PM6/Y6/PC₇₁BM solar cells with a PCE above 15% were fabricated and characterized before and after the exposure to 50 or 100°C for 1020 minutes, respectively.

The binary and ternary devices show excellent temperature stabilities at 50°C for 1020 minutes, indicating that even over a longer period of time, these systems seem to be quite stable and real differences between the binary and ternary systems at 1020 minutes at 50°C are not given.

In contrast, at a temperature of 100°C for 1020 minutes, differences between the binary and ternary systems become visible. The ternary system seems to cope better with the effect of 100°C, because the PCE loses only 8.3% in relative terms, while the binary system deteriorates by 13.8%. The J_{SC} shows a slight increase in the ternary system and a slight decrease in the binary system while the V_{OC} behaves quite similar in both systems. The main difference, other than the PCE, is the FF, which relatively deteriorates by 9.9% for the binary system and by only 6.2% for the ternary solar cells.

The UV-Vis data of the pristine Y6 samples show a small red shift of the samples after temperature treatment with 100°C for 1020 minutes, but the spectra of the samples annealed at

50°C looked like the ones of the untreated samples. In the UV-Vis spectra of PM6, no shift is visible, but at the peak at 580, the intensity is highest for the layers without thermal aging and drops a little due to the temperature treatment at 50 and 100°C for 1020 minutes. The data for the binary and ternary system for the untreated samples and the ones aged at 50°C for 1020 minutes look very similar, but for the samples which were held at 100°C for 1020 minutes, the absorption decreases between 680 and 818 nm, but increases from 818 nm to higher wavelengths due to the red shift of the Y6 peak. Because of this red shift, the charge carrier generation in the EQE spectra also shifts for the devices aged at 100°C.

The hole and electron mobility ratio for both systems are very similar, for the untreated devices a value of 0.7 was obtained and for the aged devices at 50°C for 1020 minutes a value of 0.6. A very significant change is observed with the devices aged at 100°C. In the case of binary devices, the ratio μ_h to μ_e increases from 0.7 to 7.9 and for the ternary devices, an increase by a factor of 17, from 0.7 to 12.1, due to significantly worsening electron mobility with almost unchanged hole mobility, is observed.

By studying the dependence of the short-circuit current density on the light intensity, no differences in the α value are observed. The recombination in the V_{OC} region is based on a mixture of bimolecular and trap-assisted recombination and there are no distinct differences between both systems for the untreated and temperature-aged devices, except for the not aged ternary device, which has a lower n value. This could be because the additional PC₇₁BM facilitates electron transport in the absorber layer, thereby reducing trap-assisted recombination, which disappears upon thermal aging.

No significant changes of the exciton dissociation probability due to thermal aging can be observed for both systems, but the charge collection efficiency is different. In case of the binary system, the untreated devices and those aged at 50°C for 1020 minutes are very similar, with a value of 92 ± 1 and $91 \pm 1\%$, but the charge collection efficiency deteriorates to a value of $82 \pm 1\%$ when thermally aged at 100°C for 1020 minutes. Thus, these layers show poorer charge transport and increased recombination. The ternary devices aged at 100°C drop only to $87 \pm 1\%$. The difference between binary and ternary devices is also evident in the performance, where the binary devices deteriorate by 13.8% after thermal aging, while the ternary devices lose only 8.3% (relative) in efficiency.

The AFM topography images of the binary and ternary devices show no prominent changes in the surface morphology but the phase images of both systems show the trend of a more defined phase separation after the temperature treatment at 100°C.

TEM measurements were used to examine the binary system for domain size through the nitrogen and sulfur distribution. This approach is very helpful since sulfur occurs in donor PM6 and acceptor Y6, but nitrogen only in Y6. The Y6 domains in the absorber layers appear to be approximately 15-20 nm in size, while the PM6 domains are slightly larger, typically around 30 nm, but also larger domains are observed. With the temperature treatments at 50 and 100°C for 1020 minutes, no significant changes in the sizes of the Y6 and the PM6 phase are observed. With respect to phase purity, these studies do not allow any clear conclusions to be drawn, since the thickness of the samples ranged between 70 and 100 nm and the contrasts in the TEM characterization may therefore also be due to different PM6 or Y6 domains at different depths of the sample.

To gain further insight into the changes in crystallinity of the PM6/Y6 films as a function of temperature treatment, GIWAXS and GISAXS measurements were performed. The GIWAXS data prove an increased crystallinity in the absorber layer after the temperature treatment. Furthermore, the GISAXS data show no significant change in domain sizes, which is also confirmed by the TEM elemental distribution images, but indicate a more defined phase separation between PM6 and the Y6 phase after aging at 100°C for 1020 minutes, as already observed in the AFM phase images.

In order to investigate the long-term temperature stability, three experiments were carried out. First, the ISOS-D-1 Shelf Life, where the devices were stored under nitrogen atmosphere in the glovebox and under dark conditions, was tested. The binary devices were measured regularly for about 5500 hours and the ternary devices for about 6000 hours. The two systems follow the same trend and no significant difference was found between the binary and ternary systems. The PCE lost a little over 20% relative and the FF a little over 10% by the end of the experiment. For current density and voltage, the change is not that high. The clear change in the shape of the JV characteristics is an indication of an increase in the series resistance. The parallel resistance probably changes only very slightly, since the slope in the reverse direction remains quite stable. T_{80} values of about 5000 hours were obtained in the shelf life experiment with the ternary and about 3600 hours with the binary system.

The second experiment for long-term temperature stability was the ISOS-D-2 High Storage Temperature, in which the devices were stored at constant 65°C, in the dark and under nitrogen atmosphere in the glovebox. The devices were exposed to 65°C for 1080 hours and measured regularly. The observed trend is the same for both systems, but the ternary system performed a little better. The T_{80} values of the 65°C storage experiment have remained below 200 hours.

The third long-term temperature stability experiment was the ISOS-LT-1 thermal cycling, using temperature cycling between 25 and 65°C, with one cycle time about 3 hours, done in the dark and under nitrogen atmosphere in the glovebox. The devices were measured regularly up to 200 cycles. The T_{80} values were significantly below 100 cycles for both systems, with a clear advantage of the ternary system.

If the T_{80} values of the different long-term temperature stability experiments are compared, it can be seen that without temperature influence, significantly longer lifetimes (a few thousand hours, up to a drop of 20% in PCE) are found, whereas with a constant temperature exposure of 65°C, this is achieved very quickly after less than 200 hours. Also in the temperature cycling test, the drop down to 80% of the initial efficiency occurs very quickly.

5 Experimental part

5.1 Solar cell and sample preparation

Glass substrates with a size of $1.5 \times 1.5 \text{ cm}^2$ coated with conductive indium tin oxide layer (15 ohm/cm) were used to manufacture the solar cells. The substrates were cleaned in isopropanol using an ultrasonic bath and followed by an oxygen plasma treatment (femto, Diener electronic).

After this cleaning procedure, an approximately 30 nm thick hole transport layer was spin coated (using a Laurell WS-650MZ-23NPPB spincoater) in air, at a speed of 3500 rpm and a ramp of 1500 rpm s^{-1} , for 30 seconds and with 50 μl of the PEDOT:PSS solution. After coating, the substrates were baked at 150°C , under nitrogen atmosphere in the glovebox for 10 minutes.

The active layer was spin-coated in the nitrogen-filled glovebox. The speed was 5000 rpm (ramp of 2500 rpm s^{-1}), the time of the spin coating step was 40 seconds and 100 μl of the solution were applied on the substrate. An annealing step of 10 minutes at 100°C was then carried out. The concentration of the binary system solution was 6 mg/ml PM6 with a weight ratio of PM6/Y6 of 1/1.2. The same PM6 concentration was used for the ternary system, but with a PM6/Y6/PC₇₁BM weight ratio of 1/1/0.2. Chloroform containing 0.5% chloronaphthalene was used as the solvent.

After the deposition of the absorber layer, an electron transport layer (ETL) was spin-coated also in the glovebox. PNDIT-F3N-Br was used with a concentration of 0.5 mg/ml in methanol. The spin-coating speed was 2000 rpm with a ramp of 1500 rpm s^{-1} , the time of the process was 30 seconds and 50 μl of solution were applied.

The last step was to deposit the silver electrodes via thermal evaporation in a vacuum chamber in the glove box. The electrodes were deposited at a rate of about 0.1 nm/s to a final layer thickness of 100 nm at a vacuum below 1.10^{-5} mbar .

5.2 Solar cell characterization – JV characteristics

The measurements of the JV curves and the storage of the devices took place in a nitrogen-filled glovebox with a Keithley 2400 source meter and a Dedolight DLH400D lamp (1000 W m^{-2} , comparable to AM1.5G). The Dedolight DLH400D lamp was calibrated using a reference silicon solar cell (Fraunhofer ISE). The exposed electrode area was 0.07 cm^2 , defined by a

shadow mask. The slope of the corresponding linear fit of the JV curve measured under illumination at open circuit or short circuit conditions, respectively, was used to determine the values of R_S and R_P .

5.3 Temperature stability tests

The devices of the investigation of the annealing step, the treatment for 1020 minutes, the shelf life tests, the stability investigations at elevated storage temperatures and the thermal cycling experiments were prepared according to the described standard procedure. Only in case of the devices of the investigation of the annealing step, the heating process of the active layer was different. For the storage experiments at elevated temperature and thermal cycling experiment, two heating/cooling chambers were developed and constructed at ICTM in collaboration with Lukas Troi, BSc.

5.3.1 Investigation of the annealing step

Except for the heating of the active layer, all production steps were identical to the standard procedure. A set of similarly prepared absorber layers were subjected to an annealing program, in which the samples were heated with a rate of $10^{\circ}\text{C}/\text{min}$, from room temperature to 200°C and then maintaining 200°C for 20 minutes. For this purpose, 20 devices, each with six solar cells, were placed on a hot plate and after every 10°C temperature increase, a substrate was removed from the hot plate during the heating run. After reaching 200°C , the last two set of solar cells were taken of the heating plate after 10 and 20 minutes.

5.3.2 Temperature treatment for 1020 minutes at 50 and 100°C

To investigate the temperature stability of the 1020 minutes treatment, 20 standard devices of each system, the binary PM6/Y6 and the ternary PM6/Y6/PC₇₁BM, with a PCE greater than 15% were built. Subsequently, 10 devices were characterized via recording of JV curves without temperature treatment and after expose to 50°C for over 1020 minutes and the other 10 devices also were measured without and with a temperature treatment at 100°C for 1020 minutes, for both systems.

5.3.3 ISOS-D-1 shelf life

Between the measurements, the devices were stored in the dark under nitrogen atmosphere in the glovebox. For characterization, JV curves were recorded at appropriate intervals and the corresponding parameters were determined.

5.3.4 ISOS-D-2 high storage temperature

During this experiment, the devices were stored in a closed heating chamber constructed at ICTM to protect the devices from any external influences, at a constant temperature of 65°C with an accuracy of $\pm 0.5^\circ\text{C}$, under nitrogen atmosphere in the glovebox. JV curves were recorded at certain intervals to determine the respective parameters. The temperature was controlled by a Eurotherm 2208e microcontroller.

5.3.5 ISOS-LT-1 solar thermal cycling (cycle RT – 65°C)

For the cycling experiments, JV curves, until reaching 50 cycles, were recorded after every 10 cycles and then after every 50 cycles. The temperature applied profile is shown in Figure 46. At a rate of $0.5^\circ\text{C}/\text{min}$, the devices were heated from 25 to 65°C, then the temperature of 65°C was held for 15 minutes before the solar cells were cooled back to 25°C at a rate of $-0.5^\circ\text{C}/\text{min}$, and then the temperature was held at 25°C again for 15 minutes. The temperature, with an accuracy of $\pm 0.5^\circ\text{C}$, was set using a Eurotherm 2408 microcontroller. The devices were placed for the temperature cycling in a closed heating/cooling chamber, under nitrogen atmosphere in the glovebox. To achieve a defined cooling rate and the final temperature of 25°C, which is normally below the temperature of the glovebox, a Peltier-element was additionally installed in the chamber.

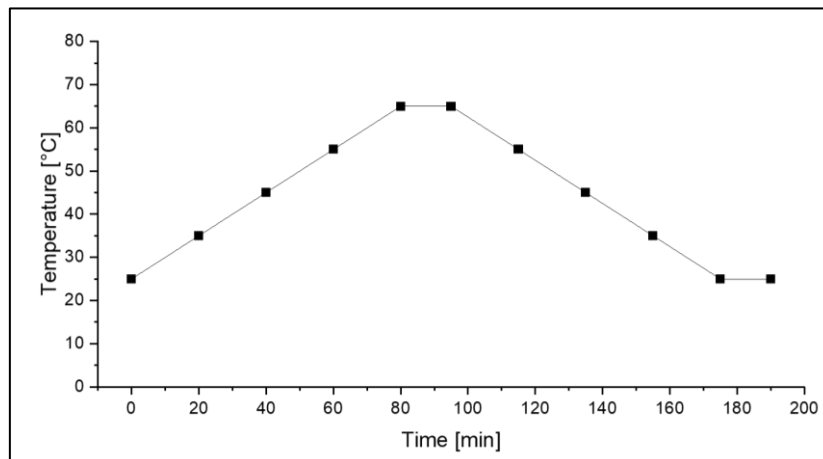


Figure 46: Temperature profile of one cycle.

5.4 Layer thickness measurements

To evaluate the layer thickness of the thin film samples, surface profilometry measurements were made using a Bruker DektakXT stylus surface profiling system with a 12.5 μm -radius stylus tip. A stylus force of 3 mg and a resolution of 0.33 $\mu\text{m pt}^{-1}$ were used to capture line

scans across a length of 500 μm . The Vision 64 program (Bruker) was used to reveal layer thickness values from two-dimensional surface profiles.

5.5 UV/Vis spectroscopy

Absorption spectra were recorded using a Shimadzu UV-1800 spectrometer in the range of 350 - 1100 nm. The pure layers of PM6 and Y6, the binary PM6/Y6 system and the ternary PM6/Y6/PC₇₁BM system were measured. In addition, all layers were aged for 1020 minutes at 50 and 100°C on a hot plate under nitrogen atmosphere in the glovebox and also measured. Chloroform with 0.5% chloronaphthalene was used as solvent. For the pure PM6 and Y6 layers, a weight of 10 mg/ml was used. For the binary system, a PM6/Y6 ratio of 1/1.2 and a weight of 6 mg/ml PM6 were used. For the ternary system, a weight ratio of PM6/Y6/PC₇₁BM of 1/1/0.2 was used, as well as a weight of 6 mg/ml PM6. For the measurements, the layers were deposited on glass substrates by spincoating.

5.6 EQE spectra

EQE spectra were recorded with a Keithley 2400 source meter connected to a LabView-based software. The monochromatic light was generated via a Multimode 4-AT monochromator (Amko) and a 75 W xenon lamp as light source. The incident light beam was chopped at a frequency of 30 Hz and the amplitude of the signal was measured. The calibration was done using a silicon photodiode (818-UV/DB, Newport Corporation). The EQE-spectra were recorded from 380 to 1000 nm with a step width of 10 nm.

5.7 Determination of hole and electron mobility

A good and practicable architecture for hole only devices was applied in 2020 by Firdaus *et al.*⁸⁰ These device architectures were also used the hole only devices prepared in this work. First, PEDOT:PSS (HTL) was deposited on a glass ITO substrate, followed by the respective active layer (PM6/Y6 and PM6/Y6/PC₇₁BM). On top of the active layer again a HTL in the form of MoO₃ and on top of that an Ag electrode were applied.

In the case of the electron-only devices, a glass ITO substrate was coated with a ZnO ETL. The active layer (PM6/Y6 and PM6/Y6/PC₇₁BM) was coated on top of this, followed by another ETL (PNDIT-F3N-Br), and an Ag electrode. This workable architecture was reported in 2021 by Lua *et al.*⁸¹

By fitting the dark current to the Mott-Gurney equation (Eq. 1), which describes a single-carrier space charge limited current (SCLC), the hole and electron mobilities were determined.

$$J = \frac{9\varepsilon_0\varepsilon_r\mu V^2}{8L^3} \quad (\text{Eq. 1}) \quad \mu = \frac{8L^3 \text{slope}^2}{9\varepsilon_0\varepsilon_r} \quad (\text{Eq. 2})$$

J is the current density, measured for the hole- and electron-only devices under dark conditions, μ is the mobility, the effective internal voltage is given with V , ε_0 represents the vacuum permittivity ($8.85 \text{ CV}^{-1}\text{s}^{-1}$), the relative permittivity is ε_r , adopted with 3.0 and L is the thickness of the respective active layer. Mobilities can then be calculated from the slope of the plotted $J^{1/2}V$ -curves using Equation 2.⁸¹ In the interval of 1 to 2 volts, the slope was determined. The measured active layer thicknesses are $67 \pm 2 \text{ nm}$ and $78 \pm 3 \text{ nm}$ for the hole and electron mobility of the binary system and $65 \pm 2 \text{ nm}$ and $76 \pm 2 \text{ nm}$ for the ternary system, respectively. In addition, reference cells with normal structure in the form of glass/ITO/HTL/active layer/ETL/Ag and with inverse structure, glass/ITO/ETL/active layer/HTL/Ag were built to verify the results of the mobilities.

5.8 Light intensity dependent measurements of J_{SC} and V_{OC}

Light intensity dependent measurements were performed using neutral density filters to reduce the intensity of the light of a Dedolight DLH400D lamp from 100.0 mW/cm^2 to 6.0 mW/cm^2 ($100.0, 80.6, 51.8, 34.1, 29.6, 12.1$ and 6.0 mW/cm^2 , determined with a silicon photodiode). After an equilibration time of 2 s the J_{SC} and V_{OC} values under irradiation were recorded using a Keithley 2400 source meter. The alpha value is the slope in the double logarithmic plot of J_{SC} and the light intensity and can thus be determined graphically. The ideality factor n ($1 < n < 2$) can be obtained from the slope of the semi-logarithmic plot of the V_{OC} vs. the light intensity. The slope corresponds to nkT/q , with k the Boltzmann's constant, q as the elementary charge, n as the ideality factor and T is the temperature in Kelvin.⁷³

5.9 Exciton dissociation probability and charge collection efficiency

The JV curves for the exciton dissociation probability and charge collection efficiency were measured from 1.5 to -3.0 V. The photo-current density (J_{PH}) is equal to the current density of the exposed device minus the current density of the unexposed device. The J_{PH} was plotted as a function of the effective voltage (V_{eff}). V_{eff} is calculated by subtracting the given bias voltage from the voltage at which J_{PH} is zero. The exciton dissociation probability (n_{diss}) is represented by J_{PH}/J_{SAT} calculated under short-circuit conditions and the charge collection efficiency (n_{coll})

is represented by the current density at the maximum power point (J_{MPP}) divided with the saturated current density (J_{SAT}).⁸² The saturated current density (J_{SAT}) was determined at $V_{eff} = 2$ V.

5.10 Atomic force microscopy

AFM images were acquired on a ToscaTM 400 atomic force microscope from Anton Paar, using silicon cantilevers (AP-ARROW-NCR from NanoWorld AG) in tapping mode (resonance frequency 285 kHz, force constant 42 N m⁻¹).

5.11 TEM investigations

Scanning transmission electron microscopy (STEM) - electron energy loss spectroscopy (EELS) elemental mapping was performed similar to the procedure reported by Hoefler et al.⁷⁹ The samples for the TEM characterization were spin coated onto sodium chloride crystal substrates (Korth Kristalle GmbH) and (after the respective heat treatments) transferred to the TEM grid by dissolving the sodium chloride crystals in deionized water. STEM data and EELS spectrum images were recorded on a probe-corrected FEI Titan3 60–300 microscope equipped with a Gatan Imaging Filter (GIF) Quantum and a Gatan K2 direct electron detection camera.

5.12 GIWAXS and GISAXS measurements

The GIWAXS and GISAXS investigations were performed at the Austrian SAXS Beamline 5.2L of the electron storage ring ELETTRA (Italy) at a photon energy of 8 keV. The GIWAXS signal was monitored using a Dectris Pilatus 100k detector and the GISAXS signal with a Dectris Pilatus3 1M detector. The calibration of the detectors was carried out using p-bromo benzoic acid (GIWAXS) and silver behenate powder (d-spacing of 58.38 Å, GISAXS). The GIWAXS measurements were performed with an incidence angle of 1.1° and the GISAXS measurements with an angle of 0.32°. The in-plane and out-of-plane integrations were done with the data evaluation software SAXS DOG.⁸³

5.13 Used materials, chemicals and solvents

All chemicals used were not specially purified and used as purchased.

- Indium tin oxide coated glass substrates 15 Ω/sq; Luminescence Technology Corp.
- PEDOT:PSS; Clevios P VP.AI 4083, Heraeus
- 2-Propanol for HPLC, 99.9%, Sigma-Aldrich

- Chloroform, anhydrous, $\geq 99\%$, Sigma-Aldrich
- Methanol NORMAPUR, VWR
- PC₇₁BM, 99.9% Solenne b.v.
- Chloronaphthalene, Merck
- Y6, 1-Material
- PM6, approx. MW 30 kD, 1-Material
- PNDIT-F3N-Br, 1-Material
- Ag-pellets, 99.99%, Kurt J. Lesker
- NaCl-crystals, 13 x 2 mm, Korth Kristalle GmbH
- Si-Wafer, thickness: $625 \pm 20 \mu\text{m}$, Siegert Wafer

6 References

- 1 D. Meng, R. Zheng, Y. Zhao, E. Zhang, L. Dou and Y. Yang, Near-Infrared Materials: The Turning Point of Organic Photovoltaics, *Adv. Mater.*, 2022, **34**, 2107330.
- 2 Y. Su, L. Zhang, Z. Ding, Y. Zhang, Y. Wu, Y. Duan, Q. Zhang, J. Zhang, Y. Han, Z. Xu, R. Zhang, K. Zhao and S. Liu, Carrier Generation Engineering toward 18% Efficiency Organic Solar Cells by Controlling Film Microstructure, *Adv. Energy Mater.*, 2022, **12**, 2103940.
- 3 C. Li, J. Zhou, J. Song, J. Xu, H. Zhang, X. Zhang, J. Guo, L. Zhu, D. Wei, G. Han, J. Min, Y. Zhang, Z. Xie, Y. Yi, H. Yan, F. Gao, F. Liu and Y. Sun, Non-fullerene acceptors with branched side chains and improved molecular packing to exceed 18% efficiency in organic solar cells, *Nat. Energy*, 2021, **6**, 605–613.
- 4 L. Hong, H. Yao, Y. Cui, P. Bi, T. Zhang, Y. Cheng, Y. Zu, J. Qin, R. Yu, Z. Ge and J. Hou, 18.5% Efficiency Organic Solar Cells with a Hybrid Planar/Bulk Heterojunction, *Adv. Mater.*, 2021, **33**, e2103091.
- 5 X. Yan, J. Wu, J. Lv, L. Zhang, R. Zhang, X. Guo and M. Zhang, Highly efficient ternary solar cells with reduced non-radiative energy loss and enhanced stability via two compatible non-fullerene acceptors, *J. Mater. Chem. A*, 2022, **10**, 15605–15613.
- 6 Y. Pan, X. Zheng, J. Guo, Z. Chen, S. Li, C. He, S. Ye, X. Xia, S. Wang, X. Lu, H. Zhu, J. Min, L. Zuo, M. Shi and H. Chen, A New End Group on Nonfullerene Acceptors Endows Efficient Organic Solar Cells with Low Energy Losses, *Adv. Funct. Mater.*, 2022, **32**, 2108614.
- 7 R. Sun, Y. Wu, X. Yang, Y. Gao, Z. Chen, K. Li, J. Qiao, T. Wang, J. Guo, C. Liu, X. Hao, H. Zhu and J. Min, Single-Junction Organic Solar Cells with 19.17% Efficiency Enabled by Introducing One Asymmetric Guest Acceptor, *Adv. Mater.*, 2022, **34**, e2110147.
- 8 S. Li, Q. Fu, L. Meng, X. Wan, L. Ding, G. Lu, G. Lu, Z. Yao, C. Li and Y. Chen, Achieving over 18 % Efficiency Organic Solar Cell Enabled by a ZnO-Based Hybrid Electron Transport Layer with an Operational Lifetime up to 5 Years, *Angew. Chem.*, 2022, **134**, e202207397.
- 9 K. Yu, W. Song, J. Ge, K. Zheng, L. Xie, Z. Chen, Y. Qiu, L. Hong, C. Liu and Z. Ge, 18.01% Efficiency organic solar cell and 2.53% light utilization efficiency semitransparent organic solar cell enabled by optimizing PM6:Y6 active layer morphology, *Sci. China Chem.*, 2022, **65**, 1615–1622.
- 10 D. Li, F. Geng, T. Hao, Z. Chen, H. Wu, Z. Ma, Q. Xue, L. Lin, R. Huang, S. Leng, B. Hu, X. Liu, J. Wang, H. Zhu, M. Lv, L. Ding, M. Fahlman, Q. Bao and Y. Li, n-Doping of

- photoactive layer in binary organic solar cells realizes over 18.3% efficiency, *Nano Energy*, 2022, **96**, 107133.
- 11 J. Zhang, R. Peng, K. Yu, J. Ge, Y. Guo, D. Li, Y. Qiu and Z. Ge, Isogenous Acceptor Strategy Enables Highly Efficient Ternary Organic Solar Cells via Synergistic Morphology Regulation and Charge Recombination Reduction, *Sol. RRL*, 2022, **6**, 2200508.
 - 12 Y. Cai, Y. Li, R. Wang, H. Wu, Z. Chen, J. Zhang, Z. Ma, X. Hao, Y. Zhao, C. Zhang, F. Huang and Y. Sun, A Well-Mixed Phase Formed by Two Compatible Non-Fullerene Acceptors Enables Ternary Organic Solar Cells with Efficiency over 18.6, *Adv. Mater.*, 2021, **33**, e2101733.
 - 13 X. Xiong, X. Xue, M. Zhang, T. Hao, Z. Han, Y. Sun, Y. Zhang, F. Liu, S. Pei and L. Zhu, Melamine-Doped Cathode Interlayer Enables High-Efficiency Organic Solar Cells, *ACS Energy Lett.*, 2021, **6**, 3582–3589.
 - 14 X. Xu, W. Jing, H. Meng, Y. Guo, L. Yu, R. Li and Q. Peng, Sequential Deposition of Multicomponent Bulk Heterojunctions Increases Efficiency of Organic Solar Cells, *Adv. Mater.*, 2023, **35**, e2208997.
 - 15 Z. Zheng, J. Wang, P. Bi, J. Ren, Y. Wang, Y. Yang, X. Liu, S. Zhang and J. Hou, Tandem Organic Solar Cell with 20.2% Efficiency, *Joule*, 2022, **6**, 171–184.
 - 16 B. Schweda, M. Reinfelds, P. Hofstadler, G. Trimmel and T. Rath, Recent Progress in the Design of Fused-Ring Non-Fullerene Acceptors-Relations between Molecular Structure and Optical, Electronic, and Photovoltaic Properties, *ACS Appl. Energy Mater.*, 2021, **4**, 11899–11981.
 - 17 W. Yu, L. Huang, D. Yang, P. Fu, L. Zhou, J. Zhang and C. Li, Efficiency exceeding 10% for inverted polymer solar cells with a ZnO/ionic liquid combined cathode interfacial layer, *J. Mater. Chem. A*, 2015, **3**, 10660–10665.
 - 18 H. Gaspar, F. Figueira, L. Pereira, A. Mendes, J. C. Viana and G. Bernardo, Recent Developments in the Optimization of the Bulk Heterojunction Morphology of Polymer: Fullerene Solar Cells, *Materials*, 2018, **11**, 2560.
 - 19 D. Deng, Y. Zhang, J. Zhang, Z. Wang, L. Zhu, J. Fang, B. Xia, Z. Wang, K. Lu, W. Ma and Z. Wei, Fluorination-enabled optimal morphology leads to over 11% efficiency for inverted small-molecule organic solar cells, *Nat. Commun.*, 2016, **7**, 13740.
 - 20 W. Li, J. Cai, F. Cai, Y. Yan, H. Yi, R. S. Gurney, D. Liu, A. Iraqi and T. Wang, Achieving over 11% power conversion efficiency in PffBT4T-2OD-based ternary polymer solar cells with enhanced open-circuit-voltage and suppressed charge recombination, *Nano Energy*, 2018, **44**, 155–163.

- 21 J. Zhao, Y. Li, G. Yang, K. Jiang, H. Lin, H. Ade, W. Ma and H. Yan, Efficient organic solar cells processed from hydrocarbon solvents, *Nat. Energy*, 2016, **1**, 15027.
- 22 S. Xiao, Q. Zhang and W. You, Molecular Engineering of Conjugated Polymers for Solar Cells: An Updated Report, *Adv. Mater.*, 2017, **29**, 1601391.
- 23 Y. Huang, L. Meng, H. Liang, M. Li, H. Chen, C. Jiang, K. Zhang, F. Huang, Z. Yao, C. Li, X. Wan and Y. Chen, Tandem organic solar cells with 18.67% efficiency via careful subcell design and selection, *J. Mater. Chem. A*, 2022, **10**, 11238–11245.
- 24 A. Lan, Y. Lv, J. Zhu, H. Lu, H. Do, Z.-K. Chen, J. Zhou, H. Wang, F. Chen and E. Zhou, High-Performance Ternary Organic Solar Cells through Incorporation of a Series of A 2 - A 1 -D-A 1 -A 2 Type Nonfullerene Acceptors with Different Terminal Groups, *ACS Energy Lett.*, 2022, **7**, 2845–2855.
- 25 D. Luo, W. Jang, D. D. Babu, M. S. Kim, D. H. Wang and A. K. K. Kyaw, Recent progress in organic solar cells based on non-fullerene acceptors: materials to devices, *J. Mater. Chem. A*, 2022, **10**, 3255–3295.
- 26 X. Zhang, Z. Lu, L. Ye, C. Zhan, J. Hou, S. Zhang, B. Jiang, Y. Zhao, J. Huang, S. Zhang, Y. Liu, Q. Shi, Y. Liu and J. Yao, A potential perylene diimide dimer-based acceptor material for highly efficient solution-processed non-fullerene organic solar cells with 4.03% efficiency, *Adv. Mater.*, 2013, **25**, 5791–5797.
- 27 J. Liu, S. Chen, D. Qian, B. Gautam, G. Yang, J. Zhao, J. Bergqvist, F. Zhang, W. Ma, H. Ade, O. Inganäs, K. Gundogdu, F. Gao and H. Yan, Fast charge separation in a non-fullerene organic solar cell with a small driving force, *Nat. Energy*, 2016, **1**, 1–7.
- 28 M. Li, Y. Liu, W. Ni, F. Liu, H. Feng, Y. Zhang, T. Liu, H. Zhang, X. Wan, B. Kan, Q. Zhang, T. P. Russell and Y. Chen, A simple small molecule as an acceptor for fullerene-free organic solar cells with efficiency near 8%, *J. Mater. Chem. A*, 2016, **4**, 10409–10413.
- 29 J. Lee, S.-J. Ko, M. Seifrid, H. Lee, B. R. Luginbuhl, A. Karki, M. Ford, K. Rosenthal, K. Cho, T.-Q. Nguyen and G. C. Bazan, Bandgap Narrowing in Non-Fullerene Acceptors: Single Atom Substitution Leads to High Optoelectronic Response Beyond 1000 nm, *Adv. Energy Mater.*, 2018, **8**, 1801212.
- 30 S. Li, L. Zhan, W. Zhao, S. Zhang, B. Ali, Z. Fu, T.-K. Lau, X. Lu, M. Shi, C.-Z. Li, J. Hou and H. Chen, Revealing the effects of molecular packing on the performances of polymer solar cells based on A–D–C–D–A type non-fullerene acceptors, *J. Mater. Chem. A*, 2018, **6**, 12132–12141.

- 31 L. Feng, J. Yuan, Z. Zhang, H. Peng, Z.-G. Zhang, S. Xu, Y. Liu, Y. Li and Y. Zou, Thieno3,2-bpyrrolo-Fused Pentacyclic Benzotriazole-Based Acceptor for Efficient Organic Photovoltaics, *ACS Appl. Mater. Interfaces*, 2017, **9**, 31985–31992.
- 32 J. Yuan, Y. Zhang, L. Zhou, G. Zhang, H.-L. Yip, T.-K. Lau, X. Lu, C. Zhu, H. Peng, P. A. Johnson, M. Leclerc, Y. Cao, J. Ulanski, Y. Li and Y. Zou, Single-Junction Organic Solar Cell with over 15% Efficiency Using Fused-Ring Acceptor with Electron-Deficient Core, *Joule*, 2019, **3**, 1140–1151.
- 33 W. Tress, *Organic Solar Cells*, Springer International Publishing, Cham, 2014.
- 34 M. Mainville and M. Leclerc, Recent Progress on Indoor Organic Photovoltaics: From Molecular Design to Production Scale, *ACS Energy Lett.*, 2020, **5**, 1186–1197.
- 35 Y. Cui, L. Hong and J. Hou, Organic Photovoltaic Cells for Indoor Applications: Opportunities and Challenges, *ACS Appl. Mater. Interfaces*, 2020, **12**, 38815–38828.
- 36 S. A. Hashemi, S. Ramakrishna and A. G. Aberle, Recent progress in flexible–wearable solar cells for self-powered electronic devices, *Energy Environ. Sci.*, 2020, **13**, 685–743.
- 37 L. La Notte, L. Giordano, E. Calabrò, R. Bedini, G. Colla, G. Puglisi and A. Reale, Hybrid and organic photovoltaics for greenhouse applications, *Appl. Energy*, 2020, **278**, 115582.
- 38 K. Yu, S. Rich, S. Lee, K. Fukuda, T. Yokota and T. Someya, Organic Photovoltaics: Toward Self-Powered Wearable Electronics, *Proc. IEEE*, 2019, **107**, 2137–2154.
- 39 A. Armin, W. Li, O. J. Sandberg, Z. Xiao, L. Ding, J. Nelson, D. Neher, K. Vandewal, S. Shoaee, T. Wang, H. Ade, T. Heumüller, C. Brabec and P. Meredith, A History and Perspective of Non-Fullerene Electron Acceptors for Organic Solar Cells, *Adv. Energy Mater.*, 2021, **11**, 2003570.
- 40 J.-S. Wu, S.-W. Cheng, Y.-J. Cheng and C.-S. Hsu, Donor-acceptor conjugated polymers based on multifused ladder-type arenes for organic solar cells, *Chem. Soc. Rev.*, 2015, **44**, 1113–1154.
- 41 H. Hu, K. Jiang, G. Yang, J. Liu, Z. Li, H. Lin, Y. Liu, J. Zhao, J. Zhang, F. Huang, Y. Qu, W. Ma and H. Yan, Terthiophene-based D-A polymer with an asymmetric arrangement of alkyl chains that enables efficient polymer solar cells, *J. Am. Chem. Soc.*, 2015, **137**, 14149–14157.
- 42 S. H. Park, A. Roy, S. Beaupré, S. Cho, N. Coates, J. S. Moon, D. Moses, M. Leclerc, K. Lee and A. J. Heeger, Bulk heterojunction solar cells with internal quantum efficiency approaching 100%, *Nat. Photonics*, 2009, **3**, 297–302.

- 43 Z. Chen, P. Cai, J. Chen, X. Liu, L. Zhang, L. Lan, J. Peng, Y. Ma and Y. Cao, Low band-gap conjugated polymers with strong interchain aggregation and very high hole mobility towards highly efficient thick-film polymer solar cells, *Adv. Mater.*, 2014, **26**, 2586–2591.
- 44 M. Zhang, X. Guo, W. Ma, H. Ade and J. Hou, A Large-Bandgap Conjugated Polymer for Versatile Photovoltaic Applications with High Performance, *Adv. Mater.*, 2015, **27**, 4655–4660.
- 45 M. Kaltenbrunner, M. S. White, E. D. Głowacki, T. Sekitani, T. Someya, N. S. Sariciftci and S. Bauer, Ultrathin and lightweight organic solar cells with high flexibility, *Nat. Commun.*, 2012, **3**, 770.
- 46 X. Xu, D. Li, J. Yuan, Y. Zhou and Y. Zou, Recent advances in stability of organic solar cells, *EnergyChem*, 2021, **3**, 100046.
- 47 Y. Zhao, Z. Wu, X. Liu, Z. Zhong, R. Zhu and J. Yu, Revealing the photo-degradation mechanism of PM6:Y6 based high-efficiency organic solar cells, *J. Mater. Chem. C*, 2021, **9**, 13972–13980.
- 48 Y. Han, H. Dong, W. Pan, B. Liu, X. Chen, R. Huang, Z. Li, F. Li, Q. Luo, J. Zhang, Z. Wei and C.-Q. Ma, An Efficiency of 16.46% and a T80 Lifetime of Over 4000 h for the PM6:Y6 Inverted Organic Solar Cells Enabled by Surface Acid Treatment of the Zinc Oxide Electron Transporting Layer, *ACS Appl. Mater. Interfaces*, 2021, **13**, 17869–17881.
- 49 Y. Zeng, D. Li, H. Wu, Z. Chen, S. Leng, T. Hao, S. Xiong, Q. Xue, Z. Ma, H. Zhu and Q. Bao, Enhanced Charge Transport and Broad Absorption Enabling Record 18.13% Efficiency of PM6:Y6 Based Ternary Organic Photovoltaics with a High Fill Factor Over 80%, *Adv. Funct. Mater.*, 2022, **32**, 2110743.
- 50 X. Li, L. Zhou, X. Lu, L. Cao, X. Du, H. Lin, C. Zheng and S. Tao, Hydrogen bond induced high-performance quaternary organic solar cells with efficiency up to 17.48% and superior thermal stability, *Mater. Chem. Front.*, 2021, **5**, 3850–3858.
- 51 M. Fahlman, S. Fabiano, V. Gueskine, D. Simon, M. Berggren and X. Crispin, Interfaces in organic electronics, *Nat. Rev. Mater.*, 2019, **4**, 627–650.
- 52 P. Li and Z.-H. Lu, Interface Engineering in Organic Electronics: Energy-Level Alignment and Charge Transport, *Small Sci.*, 2021, **1**, 2000015.
- 53 R. Li, G. Liu, M. Xiao, X. Yang, X. Liu, Z. Wang, L. Ying, F. Huang and Y. Cao, Non-fullerene acceptors based on fused-ring oligomers for efficient polymer solar cells via complementary light-absorption, *J. Mater. Chem. A*, 2017, **5**, 23926–23936.
- 54 A. Karki, J. Vollbrecht, A. J. Gillett, S. S. Xiao, Y. Yang, Z. Peng, N. Schopp, A. L. Dixon, S. Yoon, M. Schrock, H. Ade, G. N. M. Reddy, R. H. Friend and T.-Q. Nguyen, The role of

- bulk and interfacial morphology in charge generation, recombination, and extraction in non-fullerene acceptor organic solar cells, *Energy Environ. Sci.*, 2020, **13**, 3679–3692.
- 55 J. Roncali and I. Grosu, The Dawn of Single Material Organic Solar Cells, *Adv. Sci.*, 2019, **6**, 1801026.
 - 56 Y. Wu, J. Guo, W. Wang, Z. Chen, Z. Chen, R. Sun, Q. Wu, T. Wang, X. Hao, H. Zhu and J. Min, A conjugated donor-acceptor block copolymer enables over 11% efficiency for single-component polymer solar cells, *Joule*, 2021, **5**, 1800–1815.
 - 57 X. Jiang, J. Yang, S. Karuthedath, J. Li, W. Lai, C. Li, C. Xiao, L. Ye, Z. Ma, Z. Tang, F. Laquai and W. Li, Miscibility-Controlled Phase Separation in Double-Cable Conjugated Polymers for Single-Component Organic Solar Cells with Efficiencies over 8%, *Angew. Chem.*, 2020, **59**, 21683–21692.
 - 58 P. Bi and X. Hao, Versatile Ternary Approach for Novel Organic Solar Cells: A Review, *Sol. RRL*, 2019, **3**, 1800263.
 - 59 X. Xu, Y. Li and Q. Peng, Recent advances in morphology optimizations towards highly efficient ternary organic solar cells, *Nano Select*, 2020, **1**, 30–58.
 - 60 P. Cheng, J. Wang, X. Zhan and Y. Yang, Constructing High-Performance Organic Photovoltaics via Emerging Non-Fullerene Acceptors and Tandem-Junction Structure, *Adv. Energy Mater.*, 2020, **10**, 2000746.
 - 61 K. Zhang, L. Ying, H.-L. Yip, F. Huang and Y. Cao, Toward Efficient Tandem Organic Solar Cells: From Materials to Device Engineering, *ACS Appl. Mater. Interfaces*, 2020, **12**, 39937–39947.
 - 62 X. Xu, Y. Li and Q. Peng, Recent Advances Toward Highly Efficient Tandem Organic Solar Cells, *Small Struct.*, 2020, **1**, 2000016.
 - 63 D. Di Carlo Rasi and R. A. J. Janssen, Advances in Solution-Processed Multijunction Organic Solar Cells, *Adv. Mater.*, 2019, **31**, e1806499.
 - 64 F. Zhao, H. Zhang, R. Zhang, J. Yuan, D. He, Y. Zou and F. Gao, Emerging Approaches in Enhancing the Efficiency and Stability in Non-Fullerene Organic Solar Cells, *Adv. Energy Mater.*, 2020, **10**, 2002746.
 - 65 *Principles of Fluorescence Spectroscopy*, Springer, Boston, MA, 2006.
 - 66 P. C. Y. Chow, S. Albert-Seifried, S. Gélinas and R. H. Friend, Nanosecond intersystem crossing times in fullerene acceptors: implications for organic photovoltaic diodes, *Adv. Mater.*, 2014, **26**, 4851–4854.

- 67 D. C. Coffey, A. J. Ferguson, N. Kopidakis and G. Rumbles, Photovoltaic charge generation in organic semiconductors based on long-range energy transfer, *ACS Nano*, 2010, **4**, 5437–5445.
- 68 J. D. A. Lin, O. V. Mikhnenko, J. Chen, Z. Masri, A. Ruseckas, A. Mikhailovsky, R. P. Raab, J. Liu, P. W. M. Blom, M. A. Loi, C. J. García-Cervera, I. D. W. Samuel and T.-Q. Nguyen, Systematic study of exciton diffusion length in organic semiconductors by six experimental methods, *Mater. Horiz.*, 2014, **1**, 280–285.
- 69 O. V. Mikhnenko, P. W. M. Blom and T.-Q. Nguyen, Exciton diffusion in organic semiconductors, *Energy Environ. Sci.*, 2015, **8**, 1867–1888.
- 70 IEC 61215–2:2016 *Terrestrial Photovoltaic (PV) Modules - Design Qualification and Type Approval - Part 2: Test Procedures* (IEC Webstore, 2016).
- 71 IEC 61215–1:2016 *Terrestrial Photovoltaic (PV) Modules - Design Qualification and Type Approval - Part 1: Test Requirements* (IEC Webstore, 2016).
- 72 M. O. Reese, S. A. Gevorgyan, M. Jørgensen, E. Bundgaard, S. R. Kurtz, D. S. Ginley, D. C. Olson, M. T. Lloyd, P. Morvillo, E. A. Katz, A. Elschner, O. Haillant, T. R. Currier, V. Shrotriya, M. Hermenau, M. Riede, K. R. Kirov, G. Trimmel, T. Rath, O. Inganäs, F. Zhang, M. Andersson, K. Tvingstedt, M. Lira-Cantu, D. Laird, C. McGuinness, S. Gowrisanker, M. Pannone, M. Xiao, J. Hauch, R. Steim, D. M. DeLongchamp, R. Rösch, H. Hoppe, N. Espinosa, A. Urbina, G. Yaman-Uzunoglu, J.-B. Bonekamp, A. J. van Breemen, C. Girotto, E. Voroshazi and F. C. Krebs, Consensus stability testing protocols for organic photovoltaic materials and devices, *Sol. Energy Mater. Sol. Cells*, 2011, **95**, 1253–1267.
- 73 Y. Qin, Y. Xu, Z. Peng, J. Hou and H. Ade, Low Temperature Aggregation Transitions in N3 and Y6 Acceptors Enable Double-Annealing Method That Yields Hierarchical Morphology and Superior Efficiency in Nonfullerene Organic Solar Cells, *Adv. Funct. Mater.*, 2020, **30**, 2005011.
- 74 J. Lv, H. Tang, J. Huang, C. Yan, K. Liu, Q. Yang, D. Hu, R. Singh, J. Lee, S. Lu, G. Li and Z. Kan, Additive-induced miscibility regulation and hierarchical morphology enable 17.5% binary organic solar cells, *Energy Environ. Sci.*, 2021, **14**, 3044–3052.
- 75 Y. Fu, J. Qu, Y. Geng, B. Wang, Y. Han and Z. Xie, Insight into correlation between molecular length and exciton dissociation, charge transport and recombination in Polymer: Oligomer based solar cells, *Org. Electron.*, 2018, **58**, 75–81.
- 76 Z. Li, K. Jiang, G. Yang, J. Y. L. Lai, T. Ma, J. Zhao, W. Ma and H. Yan, Donor polymer design enables efficient non-fullerene organic solar cells, *Nat. Commun.*, 2016, **7**, 13094.

- 77 G. Schlichthörl, N. G. Park and A. J. Frank, Evaluation of the Charge-Collection Efficiency of Dye-Sensitized Nanocrystalline TiO₂ Solar Cells, *J. Phys. Chem. B*, 1999, **103**, 782–791.
- 78 G. Haberfehlner, S. F. Hoefler, T. Rath, G. Trimmel, G. Kothleitner and F. Hofer, Benefits of direct electron detection and PCA for EELS investigation of organic photovoltaics materials, *Micron*, 2021, **140**, 102981.
- 79 S. F. Hoefler, G. Haberfehlner, T. Rath, A. Keilbach, M. A. Hobisch, A. Dixon, E. Pavlica, G. Bratina, G. Kothleitner, F. Hofer and G. Trimmel, Elucidation of Donor:Acceptor Phase Separation in Nonfullerene Organic Solar Cells and Its Implications on Device Performance and Charge Carrier Mobility, *ACS Appl. Energy Mater.*, 2019, **2**, 7535–7545.
- 80 Y. Lin, Y. Firdaus, F. H. Isikgor, M. I. Nugraha, E. Yengel, G. T. Harrison, R. Hallani, A. El-Labban, H. Faber, C. Ma, X. Zheng, A. Subbiah, C. T. Howells, O. M. Bakr, I. McCulloch, S. de Wolf, L. Tsetseris and T. D. Anthopoulos, Self-Assembled Monolayer Enables Hole Transport Layer-Free Organic Solar Cells with 18% Efficiency and Improved Operational Stability, *ACS Energy Lett.*, 2020, **5**, 2935–2944.
- 81 Y. Luo, Y. Luo, X. Huang, S. Liu, Z. Cao, L. Guo, Q. Li, Y.-P. Cai and Y. Wang, A New Ester-Substituted Quinoxaline-Based Narrow Bandgap Polymer Donor for Organic Solar Cells, *Macromol. Rapid Commun.*, 2021, **42**, e2000683.
- 82 C. Guo, D. Li, L. Wang, B. Du, Z.-X. Liu, Z. Shen, P. Wang, X. Zhang, J. Cai, S. Cheng, C. Yu, H. Wang, D. Liu, C.-Z. Li and T. Wang, Cold-Aging and Solvent Vapor Mediated Aggregation Control toward 18% Efficiency Binary Organic Solar Cells, *Adv. Energy Mater.*, 2021, **11**, 2102000.
- 83 M. Burian, C. Meisenbichler, D. Naumenko and H. Amenitsch, SAXSDOG: open software for real-time azimuthal integration of 2D scattering images, *J. Appl. Crystallogr.*, 2022, **55**, 677–685.

7 Appendix

Table 13: Parameters of the single solar cells of the binary PM6/Y6 system before and after temperature treatment at 50°C for 1020 minutes.

BS RT	V_{OC} [mV]	J_{SC} [mA/cm²]	FF [%]	PCE [%]	R_S [Ω]	R_P [kΩ]
Cell 1	811	25.2	77.4	15.7	2.1	1.6
Cell 2	815	25.8	77.0	16.1	2.1	1.9
Cell 3	812	25.7	76.9	16.0	2.0	1.7
Cell 4	809	25.3	77.0	15.7	2.0	1.2
Cell 5	808	24.7	77.3	15.4	1.9	1.4
Cell 6	820	26.5	77.4	16.8	2.3	1.3
Cell 7	818	25.9	77.2	16.4	2.3	1.7
Cell 8	817	25.5	77.3	16.1	2.2	1.6
Cell 9	814	25.1	76.4	15.6	2.2	1.5
Cell 10	814	25.4	76.8	15.9	2.1	1.3
AV	814	25.5	77.1	16.0	2.1	1.5
SD	4	0.5	0.3	0.4	0.1	0.2
1020' 50°C	V_{OC} [mV]	J_{SC} [mA/cm²]	FF [%]	PCE [%]	R_S [Ω]	R_P [kΩ]
Cell 1	814	25.6	75.3	15.6	2.3	1.4
Cell 2	816	26.3	75.9	16.2	2.2	1.1
Cell 3	814	26.2	76.0	16.1	2.2	1.2
Cell 4	812	25.5	75.3	15.5	2.2	1.4
Cell 5	810	24.7	76.2	15.2	2.1	1.2
Cell 6	814	25.7	75.6	15.7	2.2	1.3
Cell 7	811	26.4	76.3	16.2	2.2	1.5
Cell 8	810	26.0	76.3	15.9	2.0	1.2
Cell 9	806	25.4	75.7	15.3	2.1	1.2
Cell 10	805	24.7	76.0	15.0	1.9	1.1
AV	811	25.7	75.8	15.7	2.1	1.3
SD	3	0.6	0.4	0.4	0.1	0.1
Change [%]	-0.3	1.8	-1.7	-1.9	0.0	-13.3

Table 14: Parameters of the single solar cells of the binary PM6/Y6 system before and after temperature treatment at 100°C for 1020 minutes.

BS RT	V_{oc} [mV]	J_{sc} [mA/cm²]	FF [%]	PCE [%]	R_s [Ω]	R_p [kΩ]
Cell 1	819	25.3	76.4	15.8	2.4	1.0
Cell 2	819	26.4	76.0	16.4	2.2	1.5
Cell 3	818	25.9	75.9	16.1	2.0	1.0
Cell 4	818	25.1	76.3	15.6	2.0	1.6
Cell 5	817	25.9	75.8	16.1	2.1	1.6
Cell 6	815	24.3	76.3	15.1	2.0	1.1
Cell 7	825	25.5	74.8	15.8	2.2	1.5
Cell 8	823	25.8	76.4	16.3	2.1	1.6
Cell 9	821	25.9	75.3	16.0	2.2	1.4
Cell 10	820	24.4	76.2	15.3	2.1	1.3
AV	820	25.5	75.9	15.9	2.1	1.4
SD	3	0.6	0.5	0.4	0.1	0.2
1020' 100°C	V_{oc} [mV]	J_{sc} [mA/cm²]	FF [%]	PCE [%]	R_s [Ω]	R_p [kΩ]
Cell 1	791	25.1	67.6	13.4	2.6	0.6
Cell 2	793	25.1	67.5	13.4	2.8	0.5
Cell 3	793	26.1	67.8	14.0	2.6	0.5
Cell 4	792	24.9	67.7	13.3	2.7	0.6
Cell 5	794	25.4	68.5	13.8	2.7	0.6
Cell 6	789	24.4	68.0	13.1	2.6	0.7
Cell 7	801	25.9	68.8	14.4	2.9	0.6
Cell 8	798	26.0	67.7	14.1	2.8	0.5
Cell 9	797	25.9	67.5	14.0	2.9	0.5
Cell 10	797	24.8	68.3	13.6	2.9	0.7
AV	795	25.4	68.0	13.7	2.7	0.6
SD	3	0.5	0.4	0.4	0.1	0.1
Change [%]	-3.1	-0.4	-9.9	-13.8	28.6	-57.1

Table 15: Parameters of the single solar cells of the ternary PM6/Y6/PC₇₁BM system before and after temperature treatment at 50°C for 1020 minutes.

TS RT	V_{oc} [mV]	J_{sc} [mA/cm²]	FF [%]	PCE [%]	R_s [Ω]	R_p [kΩ]
Cell 1	820	23.9	76.6	15.2	2.4	1.4
Cell 2	820	24.1	77.6	15.5	2.3	1.9
Cell 3	820	25.0	77.4	16.1	2.2	1.8
Cell 4	817	23.7	76.5	15.0	2.3	1.3
Cell 5	818	25.1	76.9	16.0	2.1	1.3
Cell 6	825	24.9	76.2	15.7	2.5	1.4
Cell 7	822	24.4	75.1	15.1	2.5	0.9
Cell 8	820	25.1	75.7	15.9	2.2	1.4
Cell 9	819	25.0	76.7	15.8	2.3	1.3
Cell 10	819	25.8	76.9	16.3	2.2	1.4
AV	820	24.7	76.6	15.7	2.3	1.4
SD	2	0.6	0.7	0.4	0.1	0.3
1020' 50°C	V_{oc} [mV]	J_{sc} [mA/cm²]	FF [%]	PCE [%]	R_s [Ω]	R_p [kΩ]
Cell 1	810	25.1	76.1	15.3	2.3	1.2
Cell 2	813	25.3	76.8	15.7	2.3	1.5
Cell 3	812	25.6	76.9	15.9	2.2	1.2
Cell 4	812	25.6	76.5	15.8	2.3	1.1
Cell 5	812	26.0	76.3	16.0	2.2	1.3
Cell 6	818	23.9	75.8	14.8	2.7	1.2
Cell 7	815	24.5	73.5	14.7	3.0	0.9
Cell 8	810	23.8	75.2	14.7	2.3	1.3
Cell 9	813	25.3	76.5	15.7	2.4	1.2
Cell 10	813	25.9	76.8	16.1	2.2	1.4
AV	813	25.1	76.0	15.5	2.4	1.2
SD	2	0.8	1.0	0.5	0.2	0.2
Change [%]	-0.9	1.6	-0.8	-1.3	4.3	-14.3

Table 16: Parameters of the single solar cells of the ternary PM6/Y6/PC71BM system before and after temperature treatment at 100°C for 1020 minutes.

TS RT	V_{oc} [mV]	J_{sc} [mA/cm²]	FF [%]	PCE [%]	R_s [Ω]	R_p [kΩ]
Cell 1	835	23.5	77.0	15.1	2.3	1.8
Cell 2	835	24.1	77.1	15.5	2.2	1.3
Cell 3	830	24.4	76.6	15.8	2.0	1.7
Cell 4	832	24.9	77.3	16.3	2.0	1.8
Cell 5	833	24.6	77.1	16.1	2.1	2.3
Cell 6	828	24.2	76.5	15.6	2.0	1.8
Cell 7	827	23.2	76.8	15.0	2.2	1.3
Cell 8	834	23.9	77.4	15.4	2.1	1.4
Cell 9	833	24.7	76.7	15.8	2.2	1.4
Cell 10	832	24.8	77.3	15.9	2.1	1.0
AV	832	24.2	77.0	15.7	2.1	1.6
SD	3	0.5	0.3	0.4	0.1	0.4
1020' 100°C	V_{oc} [mV]	J_{sc} [mA/cm²]	FF [%]	PCE [%]	R_s [Ω]	R_p [kΩ]
Cell 1	789	23.7	72.4	13.5	2.5	1.0
Cell 2	791	25.1	72.2	14.3	2.4	0.9
Cell 3	794	25.1	71.7	14.3	2.7	1.0
Cell 4	797	25.5	72.7	14.8	2.6	1.2
Cell 5	796	25.2	72.8	14.7	2.6	1.1
Cell 6	793	25.2	71.8	14.4	2.6	1.0
Cell 7	791	24.1	73.1	14.0	2.4	1.1
Cell 8	792	24.5	71.7	14.0	2.5	1.1
Cell 9	793	25.8	71.6	14.8	2.5	0.9
Cell 10	792	25.7	72.2	14.8	2.3	1.1
AV	793	25.0	72.2	14.4	2.5	1.0
SD	2	0.6	0.5	0.4	0.1	0.1
Change [%]	-4.7	3.3	-6.2	-8.3	19.0	-37.5